

VUS9/34

VU000007

TUE / 1991/13  
Box TUE/00005

VICTORIA UNIVERSITY OF TECHNOLOGY



3 0001 00084 0068

A COMPUTER CONTROLLED  
RANDOM WAVE GENERATOR



A THESIS SUBMITTED IN FULFILMENT OF  
THE REQUIREMENT FOR THE DEGREE OF  
MASTER OF ENGINEERING IN MECHANICAL ENGINEERING

BY

VINCENT ROUILLARD

DEPARTMENT OF MECHANICAL ENGINEERING  
FOOTSCRAY INSTITUTE OF TECHNOLOGY  
VICTORIA UNIVERSITY OF TECHNOLOGY  
VICTORIA, AUSTRALIA.

APRIL 1991

## ABSTRACT

*Simulation of ocean wave processes and model studies related to marine technology are areas of increasing economic and environmental importance. Sophisticated laboratory facilities are needed to model ocean wave phenomena under controlled conditions. This thesis describes the techniques and principles employed in the design, commissioning and evaluation of a computer controlled random wave generation facility devised to accurately simulate spectral wave models.*

*A discussion on the classification of ocean waves is presented together with a review of classical wave theories and their range of application. The treatment of water waves as a random process is presented along with an outline of current spectral analysis techniques. Statistical properties of random waves are considered and a description of various mathematical spectral models used to represent ocean waves is given.*

*Various designs and random wave generation techniques employed in existing laboratory wave generators are critically reviewed. A detailed description of the design of the wave generator, wave absorbers and wave probe is presented. Computer software developed for managing the wave generator was principally designed to control the wave maker motion and carry out spectral and statistical analyses of recorded wave data.*

*Experiments aimed at evaluating the characteristics of the wave generator and ancillary equipment are outlined. Both the static and dynamic properties of the wave probe were investigated as well as the reflection characteristics of the wave absorbers. The system frequency response characteristics under various operating conditions were measured and are discussed. Random waves produced from a spectral model were used to compare the performance of open and closed-loop control techniques. A series of experiments devised to investigate the capability of the system to generate spectral models of ocean waves were conducted and the results are discussed.*

## TABLE OF CONTENTS

	PAGE
<i>Acknowledgements</i>	iv
<i>List of figures</i>	v
<i>List of tables</i>	vii
<i>1. Introduction</i>	1
<i>1.1 Background</i>	1
<i>1.2 Aim and Significance</i>	2
<i>2. Review of Classical Wave Theories</i>	3
<i>2.1 Classification of Ocean Waves</i>	3
<i>2.2 Development of Classical Wave Theories</i>	4
<i>2.3 Small Amplitude Wave Theory</i>	11
<i>2.4 Finite Amplitude Wave Theory</i>	18
<i>2.5 Stoke's Wave Theory</i>	22
<i>2.6 Cnoidal Wave Theory</i>	24
<i>2.7 Solitary Wave Theory</i>	24
<i>2.8 Stream Function Wave Theory</i>	24
<i>2.9 Wave Superposition</i>	25
<i>3. Statistical Analysis of Ocean Waves</i>	33
<i>3.1 Spectral Analysis of Random Processes</i>	33
<i>3.2 Spectral Models of Ocean Waves</i>	39
<i>3.3 Distribution of Water Surface Elevation</i>	44
<i>3.4 Distribution of Surface Elevation Maxima</i>	46
<i>3.5 Distribution of Wave Heights</i>	51
<i>3.6 Significant Wave Height</i>	53

TABLE OF CONTENTS (cont'd)

4. <i>Wave Generation Equipment and Software</i>	56
4.1 <i>Review of Wave Generators</i>	56
4.2 <i>Design of Wave Generator</i>	62
4.3 <i>Wave Probe</i>	73
4.4 <i>Wave Absorbers</i>	75
4.5 <i>Control System</i>	77
4.6 <i>Software Development</i>	78
4.6.1 <i>Wave Probe Calibration</i>	78
4.6.2 <i>Reflection Evaluation and Regular Wave Generation</i>	79
4.6.3 <i>Random Wave Generation</i>	80
4.6.4 <i>System Frequency Response Measurement</i>	88
4.6.5 <i>Statistical Analysis</i>	89
5. <i>Results and Discussion</i>	93
5.1 <i>Experiments</i>	93
5.2 <i>Wave Probe Characteristics</i>	93
5.3 <i>Wave Energy Absorber Characteristics</i>	96
5.4 <i>System Frequency Response Evaluation</i>	97
5.5 <i>Comparison of Open and Closed-loop Performance</i>	106
5.6 <i>Generation of Single Peak Spectral Models</i>	114
5.7 <i>Generation of Double Peak Spectral Models</i>	123
6. <i>Conclusions</i>	129
<i>Bibliography</i>	130
<i>Appendix A. Further Theoretical Relationships for the Wallops         Spectrum</i>	136
<i>Appendix B. Formulation of the Wave Maker Generating Surface</i>	137

## ACKNOWLEDGMENTS

*I wish to express my deep appreciation to Dr. G.T. Lleonart, who initiated and supervised this study, for his valuable guidance and helpful suggestions. My gratitude extends to Mr. R. Juniper, Dr. M.A. Sek and Mr. J. McLeod for their constructive advice. My thanks also go to the technical staff of the Department of Mechanical Engineering and the Fluid Dynamics Laboratory who contributed in the construction of the wave generation facility.*

*I would finally like to thank the secretarial staff of the Department of Mechanical Engineering who assisted in the typing of this report.*

## LIST OF FIGURES

- 2.1 *Estimation of the distribution of wave energy.*
- 2.2 *Conservation of mass.*
- 2.3 *Rotation of a fluid particle.*
- 2.4 *External forces acting on a fluid element.*
- 2.5 *Schematic diagram of a small amplitude wave.*
- 2.6 *Effects of water depth on fluid particle paths.*
- 2.7 *Classification of wave theories.*
- 2.8 *Stationary finite amplitude wave.*
- 2.9 *Second order Stoke's wave.*
- 2.10 *Illustration of various wave profiles.*
- 2.11 *Polar representation of common harmonics of arbitrary phase.*
- 2.12 *Nodes and antinodes of wave envelope.*
  
- 3.1 *Linear system input-output relationships.*
- 3.2 *Variation of the water surface elevation maxima with spectral width parameter.*
- 3.3 *Narrow band random process.*
- 3.4 *Definition of wave heights.*
- 3.5 *Variation of  $H_1/n/ 2M_0$ .*
  
- 4.1 *Some types of wave makers.*
- 4.2 *Schematic of wave generation facility.*
- 4.3 *Wave maker support arrangement.*
- 4.4 *Wave maker dimensions.*
- 4.5 *Wave maker plunger.*
- 4.6 *Wave maker arrangement.*
- 4.7 *Wave generator arrangement.*
- 4.8 *Force excitation of A frame model for FEA.*
- 4.9 *Deflection response of A frame.*
- 4.10 *Displacement excitation of pivot beam for FEA.*
- 4.11 *Displacement response of pivot beam.*
- 4.12 *Electro-hydraulic wave generator system.*
- 4.13 *Wave probe.*
- 4.14 *Wave energy absorbers.*
- 4.15 *Parabolic wave absorber pattern.*

## LIST OF FIGURES (cont'd)

- 4.16 *Illustration of control method for random wave generation.*
- 4.17 *Random wave generation control flow chart.*
- 4.18 *On-line menu for random wave generation.*
- 4.19 *Signal generation and acquisition method for random wave generation.*
- 4.20 *Spectral moments computation method.*
  
- 5.1 *Wave probe static calibration curves.*
- 5.2 *Time response characteristics of wave probe.*
- 5.3 *Stoke's breaking wave profile.*
- 5.4 *Breaking wave measurement.*
- 5.5 *Amplitude reflection characteristics of wave tank.*
- 5.6 *Definition of single and dual stage systems.*
- 5.7 *Single and dual stage system frequency response estimates.*
- 5.8 *Variation of system frequency response with wave probe location.*
- 5.9 *Variation of system frequency response with input signal level.*
- 5.10 *Open-loop spectral estimates.*
- 5.11 *Closed-loop spectral estimates.*
- 5.12 *History of measured spectral estimates.*
- 5.13 *Control system recovery.*
- 5.14 *Single peak target spectra.*
- 5.15 *Command signal distribution.*
- 5.16 *Single peak spectrum - experiment 1.*
- 5.17 *Single peak spectrum - experiment 2.*
- 5.18 *Single peak spectrum - experiment 3.*
- 5.19 *Single peak spectrum - experiment 4.*
- 5.20 *Double peak spectrum - experiment 5.*
- 5.21 *Double peak target spectra.*
- 5.22 *Double peak spectrum - experiment 1.*
- 5.23 *Double peak spectrum - experiment 2.*
- 5.24 *Double peak spectrum - experiment 3.*
  
- 1B. *Development of the plunger generating surface.*
- 2B. *Expected maximum horizontal displacement error.*

## LIST OF TABLES

- 5.1 *Experimental conditions - single peak spectrum.*
- 5.2 *Statistical results - single peak spectrum.*
- 5.3 *Experimental conditions - double peak spectrum.*
- 5.4 *Statistical results - double peak spectrum.*

## 1. INTRODUCTION

### 1.1. Background.

Oceans are a major source of minerals, energy and food and constitute an essential means of communication, distribution and transport. The motions in the upper ocean provide the means for the exchange of matter, momentum and energy between the atmosphere and the underlying ocean. These exchanges produce the general circulation pattern in the oceans and at the same time form one of the most important factors in the worldwide distribution of climate.

Successful ventures in the marine environment, such as the design and construction of ships, structures, diving, dredging, drilling and towing equipment as well as communication equipment require a wide range of information and professional advice on the behaviour of the oceans.

Even to the casual observer, the random nature and continually changing condition of the ocean surface is evident. Waves of different lengths travelling at different speeds combine and recombine to form constantly changing patterns. For a long time it was thought that this apparently chaotic process was beyond adequate mathematical description. In comparatively recent times, the development of an approach based on the combination of statistics, Fourier analysis and hydrodynamics promises a better understanding of real sea conditions. Statistical theories have been used to determine stable parameters for describing random sea states, Fourier analysis was then employed to separate the random process into harmonic components which can be analysed using classical theories of wave motion.

The evaluation of sea surface conditions is a problem of long-standing interest to ocean engineers and the effects of wave motions on natural and artificial structures demand detailed and sophisticated analysis. Important considerations in the study of ocean waves are firstly, the observation, description and measurement of the phenomenon under natural, uncontrolled conditions, and secondly, the physical modelling of one or more attributes of ocean waves under controlled conditions in the

laboratory where the analysis of these motions and the development of a coherent theory can be undertaken. It is only by drawing these considerations together in a consistent manner that the nature of ocean wave motion may be better understood.

## 1.2. Aims and Significance.

There is a need for wave generators which can be readily and accurately programmed to undertake experimental studies on wave phenomena and scale modelling of offshore structures, mooring systems, breakwaters, beaches and other marine engineering systems. Such a laboratory facility would provide a tool for deepening our understanding of the basic design and physical processes involved.

With the advent of digital computers and electronically controlled servo-mechanisms, wave generators can be controlled more accurately and reliably. Furthermore, with digital computers, optimal control techniques such as feedback compensation in the frequency domain, are more easily implemented.

The principal aim of this work is to design and commission a computer controlled random wave generator capable of simulating ocean wave phenomena and analysing data in a practical engineering manner.

## 2. REVIEW OF CLASSICAL WAVE THEORIES

### 2.1. Classification of Ocean Waves.

In this chapter the classical theories for unsteady free surface flow subjected to gravitational forces are reviewed. Such motions are called water waves. They are also called gravity waves. From a physical standpoint there are a great multiplicity of water waves which range from tsunami waves generated by earthquakes to seiches in harbours; from tidal bores in estuaries to waves generated by wind in the oceans.

Water wave motions are of such diversity and complexity that classification is far from simple. One method of classifying ocean waves is by estimating the relative energy content at various wave periods. Figure 2.1, after Kinsman (1965), shows that a large amount of energy is associated with gravity waves. These waves, with periods ranging from 1 to 30 seconds, are of primary concern.

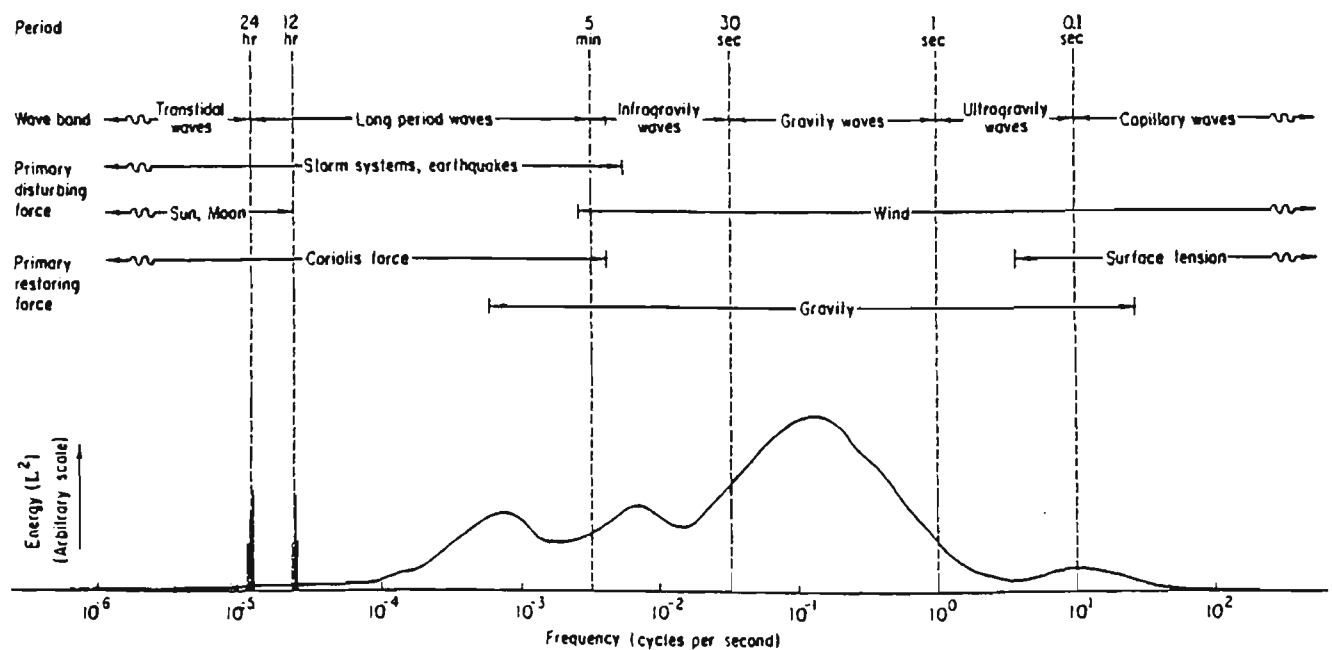


Figure 2.1. Estimation of the distribution of ocean wave energy.

- After Kinsman (1965) -

Gravity waves in the ocean are further distinguished according to the following criteria:

(i) Sea - waves created by direct action of the wind on the ocean surface.

(ii) Swell - waves caused by distant meteorological disturbances which have spread from the generating area and are no longer subjected to significant wind action.

Seas generally consist of steeper, higher frequency waves of shorter wavelengths and are more chaotic than swells. Swells persist after the source of disturbance has disappeared and maintain a constant direction so long as deep water conditions prevail. Sea waves, caused by local wind, are often superimposed on swells and interactions between the two can cause unpredictably high waves.

## 2.2. Development of Classical Wave Theories.

Water wave theories may generally be classified in two main groups. These are the small amplitude wave theories and the long wave theories. The small amplitude wave theories cover the linearised solutions for infinitesimal amplitude waves as well as power series in terms of the wave height to wavelength ratio for finite amplitude waves. Long waves theories include the numerical methods of solutions generally used for solving nonlinear long wave equations. The two groups encompass cases exhibiting features of both groups. For instance, cnoidal and solitary waves are considered as special cases of the long wave theories since they are nonlinear shallow water waves.

Water waves have traditionally been treated as the combination of many different waves of various amplitudes, wavelengths and shapes. In order to omit most of the complicating factors, classical wave theories assume the waves to be periodic and uniform. Classical wave theories are developed by approximating solutions to the differential equations describing the kinematic and dynamic conditions under certain specific boundary conditions.

In the development of water wave theories the conservation of mass, hence continuity of flow, is assumed. The equation of continuity may be derived by considering fluid flowing through an elemental volume  $\Delta V$  fixed in a rectangular Cartesian coordinate system as shown in figure 2.2.

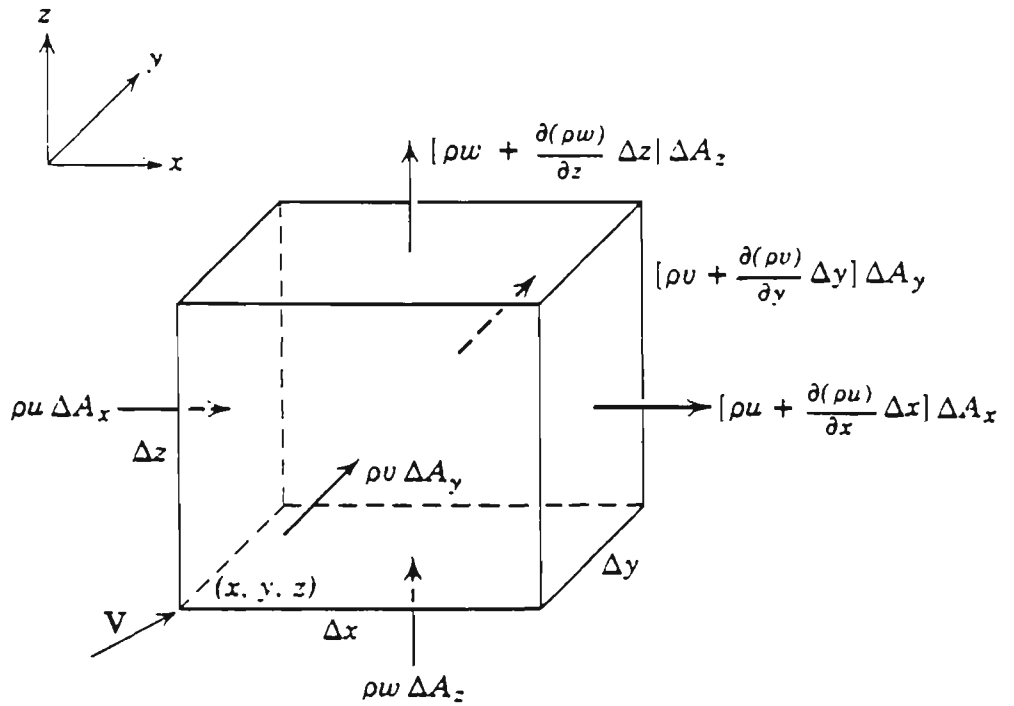


Figure 2.2. Conservation of mass.

The law of conservation of mass is expressed by

$$\frac{\delta(\rho\Delta V)}{\delta t} = -\frac{\delta(\rho u)\Delta x\Delta A_x}{\delta x} + \frac{\delta(\rho v)\Delta y\Delta A_y}{\delta y} + \frac{\delta(\rho w)\Delta z\Delta A_z}{\delta z} \quad (2.1)$$

where  $\rho$  is the fluid density and  $u$ ,  $v$  and  $w$  are the velocities in the  $x$ ,  $y$  and  $z$  directions respectively.

Since  $\Delta V = \Delta A_x = \Delta A_y = \Delta A_z$ , equation (2.1) reduces to

$$\frac{\delta\rho}{\delta t} = -\frac{\delta(\rho u)}{\delta x} + \frac{\delta(\rho v)}{\delta y} + \frac{\delta(\rho w)}{\delta z} \quad (2.2)$$

If it is assumed that the fluid is incompressible, the continuity equation may be written as

$$\frac{\delta u}{\delta x} + \frac{\delta v}{\delta y} + \frac{\delta w}{\delta z} = 0 \quad (2.3)$$

In hydrodynamics, the concept of irrotational motion is important since many real flows are nearly irrotational. The properties of irrotational motion lead to a number of simple and powerful analytical methods which can

be used to solve problems. Most of these methods result from the existence of a special function known as the velocity potential. In general, the motion of the fluid particles may be considered irrotational when the velocity gradient is small, such as in periodic gravity waves. Mathematical simplification is achieved in the treatment of fluid flow problems if the fluid is considered to be irrotational.

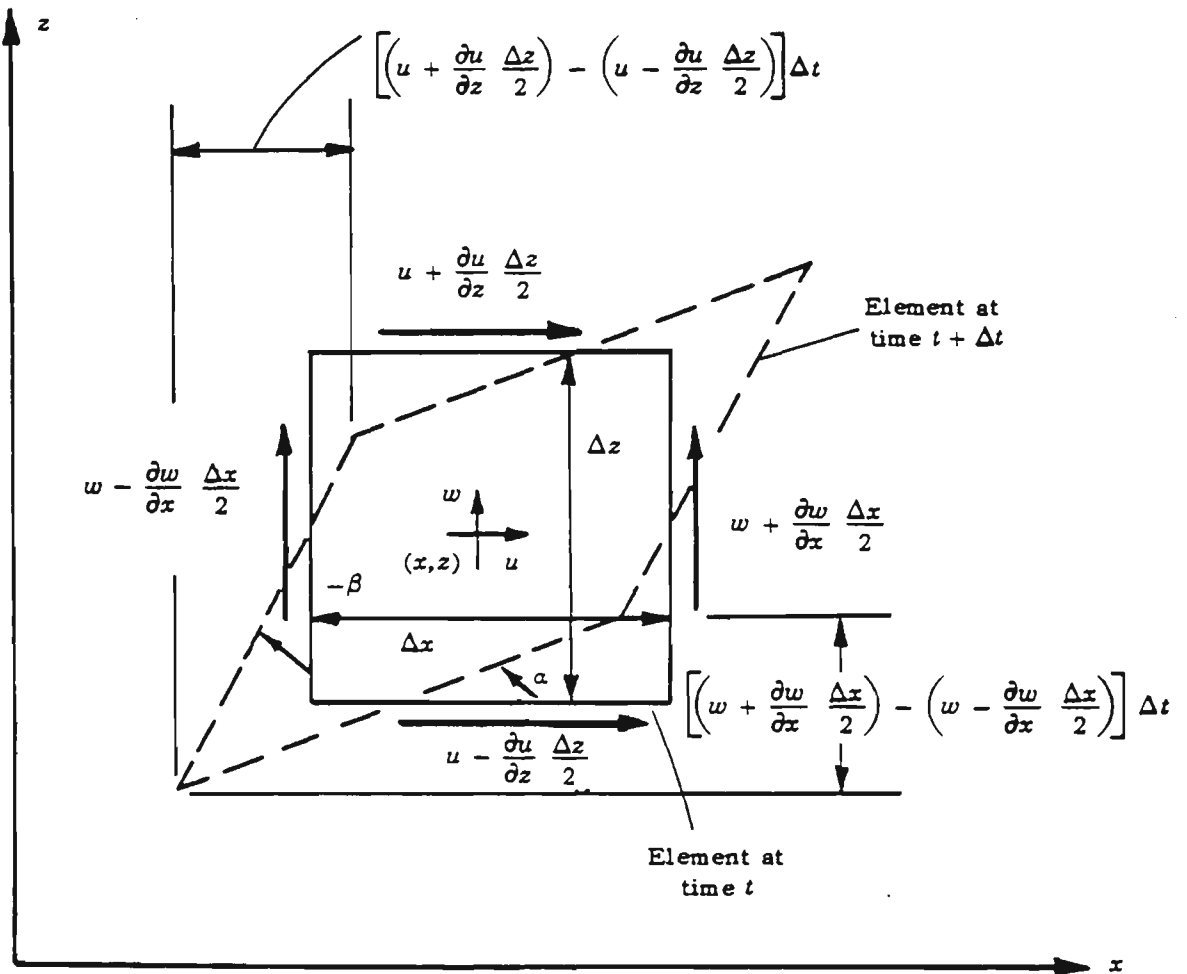


Figure 2.3. Rotation of a fluid particle.

For simplicity, the motion of a two-dimensional rectangular fluid particle with its centre of mass at  $(x, z)$  is considered as shown in figure 2.3. After a short time interval  $\Delta t$ , the element is subjected to a small deformation. From the geometrical configuration of figure 2.3, the mean velocities of the fluid particle faces, for planes parallel to the  $x$  axis, are

$$u - \frac{\delta u}{\delta z} \frac{\Delta z}{2} \quad \text{and} \quad u + \frac{\delta u}{\delta z} \frac{\Delta z}{2} \quad (2.4)$$

and for planes parallel to the  $z$  axis,

$$w - \frac{\delta w}{\delta x} \frac{\Delta x}{2} \quad \text{and} \quad w + \frac{\delta w}{\delta x} \frac{\Delta x}{2} \quad (2.5)$$

In a time interval  $\Delta t$ , the difference in the velocities of opposing planes will result in the deformation of the fluid particle as shown by the dotted line in figure 2.3. The mean rate of change of the angles  $\alpha$  and  $\beta$  may then be written as

$$\frac{\Delta \alpha}{\Delta t} = \left[ \left( w + \frac{\delta w}{\delta x} \frac{\Delta x}{2} \right) - \left( w - \frac{\delta w}{\delta x} \frac{\Delta x}{2} \right) \right] \cdot \Delta t / (\Delta x \Delta t) = \frac{\delta w}{\delta x} \quad (2.6)$$

and

$$\frac{\Delta \beta}{\Delta t} = \left[ \left( u + \frac{\delta u}{\delta z} \frac{\Delta z}{2} \right) - \left( u - \frac{\delta u}{\delta z} \frac{\Delta z}{2} \right) \right] \Delta t / (\Delta z \Delta t) = - \frac{\delta u}{\delta z} \quad (2.7)$$

where anticlockwise rotations are considered positive.

The mean angular velocity,  $\Omega_1$ , of the fluid particle in the  $x$ - $z$  plane is therefore

$$\Omega_1 = \frac{1}{2} \left[ \frac{\delta w}{\delta x} - \frac{\delta u}{\delta z} \right] \quad (2.8)$$

If three dimensional flow is considered, the remaining two components of the rotational vector are given by

$$\Omega_2 = \frac{1}{2} \left[ \frac{\delta u}{\delta y} - \frac{\delta v}{\delta x} \right] \quad \text{in the } x - y \text{ plane} \quad (2.9)$$

and

$$\Omega_3 = \frac{1}{2} \left[ \frac{\delta v}{\delta z} - \frac{\delta w}{\delta y} \right] \quad \text{in the } z - y \text{ plane} \quad (2.10)$$

The flow is rotational if  $\Omega_1 = \Omega_2 = \Omega_3$  or

$$\frac{\delta w}{\delta x} = \frac{\delta u}{\delta z}, \quad \frac{\delta w}{\delta x} = \frac{\delta u}{\delta z} \quad \text{and} \quad \frac{\delta w}{\delta x} = \frac{\delta u}{\delta z} \quad (2.11)$$

It can be stipulated that there exists a velocity potential represented by the scalar function  $\Phi(x,y,z,t)$  which, by definition, satisfies

$$u = \frac{\delta\Phi}{\delta x} \quad , \quad v = \frac{\delta\Phi}{\delta y} \quad \text{and} \quad w = \frac{\delta\Phi}{\delta z} \quad (2.12)$$

If it is assumed that the velocity potential has continuous derivatives, then

$$\frac{\delta}{\delta z} \left( \frac{\delta\Phi}{\delta x} \right) = \frac{\delta}{\delta x} \left( \frac{\delta\Phi}{\delta z} \right) \quad \text{or} \quad \frac{\delta u}{\delta z} = \frac{\delta w}{\delta x} \quad (2.13)$$

$$\frac{\delta}{\delta x} \left( \frac{\delta\Phi}{\delta y} \right) = \frac{\delta}{\delta y} \left( \frac{\delta\Phi}{\delta x} \right) \quad \text{or} \quad \frac{\delta v}{\delta x} = \frac{\delta u}{\delta y} \quad (2.14)$$

$$\frac{\delta}{\delta y} \left( \frac{\delta\Phi}{\delta z} \right) = \frac{\delta}{\delta z} \left( \frac{\delta\Phi}{\delta y} \right) \quad \text{or} \quad \frac{\delta w}{\delta y} = \frac{\delta v}{\delta z} \quad (2.15)$$

which are the conditions for irrotational flow. Consequently, for irrotational flow of an incompressible fluid, the continuity equation reduces to

$$\frac{\delta^2\Phi}{\delta x^2} + \frac{\delta^2\Phi}{\delta y^2} + \frac{\delta^2\Phi}{\delta z^2} = 0 \quad (2.16)$$

which is known as the Laplace equation.

The dynamical equations of motion are derived by considering the forces acting on an elemental mass of fluid. By Newton's second law of motion, the net sum of the external forces acting on a mass must be equal to the rate of change of the linear momentum.

By considering an elemental mass of frictionless fluid in rectangular Cartesian coordinates, as shown in figure 2.4, the sum of the forces in the x direction is

$$p\Delta y\Delta z - \left( p + \frac{\delta p}{\delta x} \Delta x \right) \Delta y\Delta z + X\rho\Delta x\Delta y\Delta z = \rho\Delta z\Delta y\Delta z \cdot \frac{du}{dt} \quad (2.17)$$

where  $X$  is the body force per unit mass acting in the x direction and  $p$  is the pressure acting on the element.

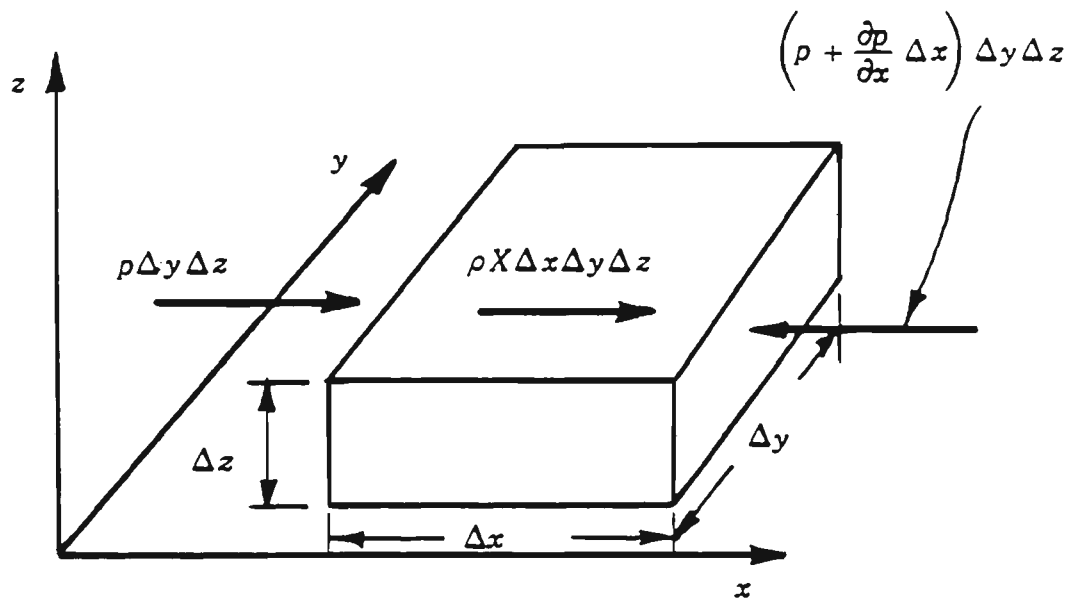


Figure 2.4. External forces acting on a fluid element.

Equation (2.17) reduces to the equation of motion for a frictionless fluid in the x direction :

$$\frac{du}{dt} = X - \frac{1}{\rho} \frac{\delta p}{\delta x} \quad (2.18)$$

Similarly

$$\frac{dv}{dt} = Y - \frac{1}{\rho} \frac{\delta p}{\delta y} \quad \text{- equation of motion in the y direction} \quad (2.19)$$

$$\frac{dw}{dt} = Z - \frac{1}{\rho} \frac{\delta p}{\delta z} \quad \text{- equation of motion in the z direction} \quad (2.20)$$

Alternatively, the equations of motion in the x, y and z directions may be written as

$$X - \frac{1}{\rho} \frac{\delta p}{\delta x} = \frac{du}{dt} = \frac{\delta u}{\delta t} + u \frac{\delta u}{\delta x} + v \frac{\delta u}{\delta y} + w \frac{\delta u}{\delta z} \quad (2.21)$$

$$Y - \frac{1}{\rho} \frac{\delta p}{\delta y} = \frac{dv}{dt} = \frac{\delta v}{\delta t} + u \frac{\delta v}{\delta x} + v \frac{\delta v}{\delta y} + w \frac{\delta v}{\delta z} \quad (2.22)$$

$$Z - \frac{1}{\rho} \frac{\delta p}{\delta z} = \frac{dw}{dt} = \frac{\delta w}{\delta t} + u \frac{\delta w}{\delta x} + v \frac{\delta w}{\delta y} + w \frac{\delta w}{\delta z} \quad (2.23)$$

Since the body forces only include gravity, then

$$X \equiv 0 \quad , \quad Y \equiv 0 \quad \text{and} \quad Z = -g = -\frac{\delta(gz)}{\delta z} \quad (2.24)$$

Under the assumption that the motion is irrotational and from the definition of the velocity potential, the continuity equations become

$$-\frac{1}{\rho} \frac{\delta p}{\delta x} = -\frac{\delta^2 \Phi}{\delta x \delta t} + u \frac{\delta u}{\delta x} + v \frac{\delta v}{\delta x} + w \frac{\delta w}{\delta x} \quad (2.25)$$

$$-\frac{1}{\rho} \frac{\delta p}{\delta y} = -\frac{\delta^2 \Phi}{\delta y \delta t} + u \frac{\delta u}{\delta y} + v \frac{\delta v}{\delta y} + w \frac{\delta w}{\delta y} \quad (2.26)$$

$$-\frac{\delta(gz)}{\delta z} - \frac{1}{\rho} \frac{\delta p}{\delta z} = -\frac{\delta^2 \Phi}{\delta z \delta t} + u \frac{\delta u}{\delta z} + v \frac{\delta v}{\delta z} + w \frac{\delta w}{\delta z} \quad (2.27)$$

If the fluid density is assumed to be uniform, equations (2.25), (2.26) and (2.27) may be written as

$$\frac{\delta}{\delta x} \left( -\frac{\delta \Phi}{\delta t} + \frac{1}{2} (u^2 + v^2 + z^2) + \frac{p}{\rho} \right) = 0 \quad (2.28)$$

$$\frac{\delta}{\delta y} \left( -\frac{\delta \Phi}{\delta t} + \frac{1}{2} (u^2 + v^2 + z^2) + \frac{p}{\rho} \right) = 0 \quad (2.29)$$

$$\frac{\delta}{\delta x} \left( -\frac{\delta \Phi}{\delta t} + \frac{1}{2} (u^2 + v^2 + z^2) + \frac{p}{\rho} + gz \right) = 0 \quad (2.30)$$

Integrating and combining equations (2.28), (2.29) and (2.30) results in the single equation describing Bernoulli's law

$$-\frac{\delta \Phi}{\delta x} + \frac{1}{2} (u^2 + v^2 + z^2) + \frac{p}{\rho} + gz = F(t) \quad (2.31)$$

where  $F(t)$  is an arbitrary function of time.

If the flow is considered steady,  $\delta \Phi / \delta t = 0$  and  $F(t) = \text{constant}$ , equation (2.31) is reduced to the steady-state Bernoulli equation

$$\frac{1}{2} (u^2 + v^2 + z^2) + \frac{p}{\rho} + gz = \text{constant} \quad (2.32)$$

In the general case, equation (2.31) is solved by obtaining  $\Phi$  through the solution of Laplace's equation.

### 2.3. Small Amplitude Wave Theory.

The small amplitude wave theory, also known as Airy's wave theory or the first order wave theory, is generally considered as the most important of all classical wave theories. It is also the basis for the spectral description of ocean waves. As its name suggests, the small amplitude wave theory is based on the assumption that the wave amplitudes are so small that the contributions of the higher order terms to the solution are negligible. By neglecting the squares of the velocity components, equation (2.31) reduces to

$$-\frac{\delta\Phi}{\delta t} + \frac{p}{\rho} + gz = 0 \quad (2.33)$$

In establishing the linearized boundary conditions necessary to solve Laplace's equation, the physical characteristics of a two-dimensional travelling surface wave are defined in figure 2.5.

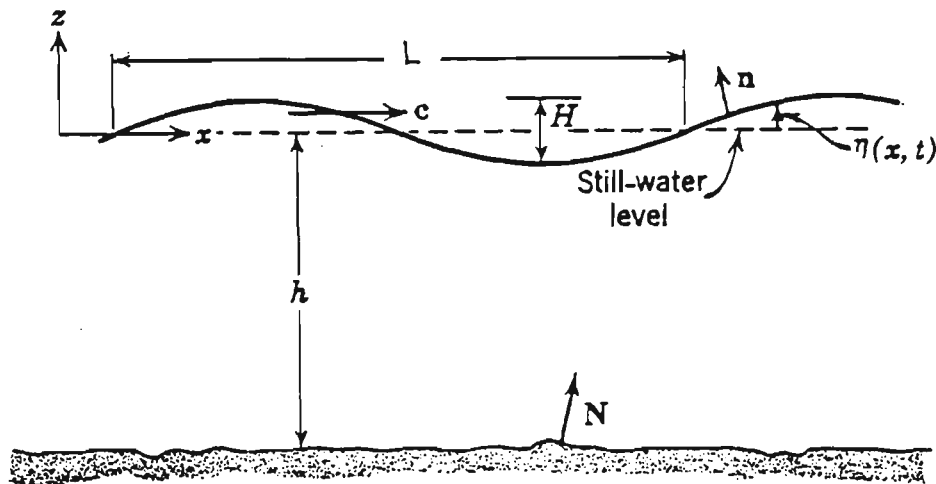


Figure 2.5. Schematic representation of a small amplitude wave.

The Cartesian coordinate system has its origin located on the still water level (SWL) and the depth,  $h$ , of the water is measured from the sea bed to the SWL. The wave is of height,  $H$ , has a wavelength,  $L$ , and a phase velocity or celerity,  $C$ .  $\eta$  denotes the elevation of the free surface from the SWL at any position  $x$  and time  $t$ .

If the seabed is regarded as fixed, horizontal and impermeable, the

velocity normal to sea bed must be zero. The bottom boundary condition may therefore be written as

$$w = - \frac{\delta\Phi}{\delta z} = 0 \quad \text{at } z = -h \quad (2.34)$$

If it is assumed that the pressure on the free surface is zero (gauge) at any position  $x$  or time  $t$  and that the flow is irrotational, the free surface boundary condition is obtained by applying Bernoulli's equation at the free surface ( $z = \eta$ ). Furthermore, by neglecting the second order terms to satisfy the small amplitude assumptions, the linearized dynamic boundary condition is

$$\eta = - \frac{1}{g} \frac{\delta\Phi}{\delta t} \quad \text{at } z = \eta = 0 \quad (2.35)$$

In physical terms the linearization assumes that the flow is sufficiently small to render the kinetic energy of the fluid particles negligible compared with the total mechanical energy in the system.

Since no particle can cross the free surface, the particle velocity at the free surface must be equal to the normal velocity at the free surface. If it is assumed that the water surface elevations are small relative to the wavelength, the rate of change of elevation of the water surface at any point may be said to be approximately equal to the vertical velocity component,  $w$ , at the same point

$$w = \frac{d\eta}{dt} = \frac{\delta\eta}{\delta t} + \frac{\delta\eta}{\delta x} \frac{\delta x}{\delta t} = 0 \quad (2.36)$$

therefore

$$\frac{\delta\eta}{\delta t} = w \quad \text{at } z = 0 \quad (2.37)$$

Since

$$w = - \frac{\delta\Phi}{\delta z} \quad (2.38)$$

The linearized free-surface boundary conditions of equations (2.35) and (2.37) may be combined by eliminating  $\eta$  to obtain

$$\frac{1}{g} \frac{\delta^2 \Phi}{\delta t^2} + \frac{\delta \Phi}{\delta z} = 0 \quad \text{for } z = \eta = 0 \quad (2.39)$$

Since a continuous fluid within the wave is being considered and irrotational flow is assumed, the differential equation to be satisfied within the region  $-h < z < +\eta$  and  $-\infty < x < +\infty$  is the two-dimensional form of Laplace's equation which is written as

$$\frac{\delta^2 \Phi}{\delta x^2} + \frac{\delta^2 \Phi}{\delta z^2} = 0 \quad (2.40)$$

Using the method of separation of variables, in which the solution of the partial differential equation is assumed in product form, the general solution of equation (2.40) may be written as

$$\Phi(x, z, t) = X(x) Z(z) T(t) \quad (2.41)$$

where  $X$  is a function of  $x$  alone,  
 $Z$  is a function of  $z$  alone,  
and  $T$  is a function of  $t$  alone.

Substituting equation (2.41) into equation (2.40), dividing by  $X(x)Z(z)T(t)$  then separating the variables yields

$$\frac{1}{X} \frac{d^2 X}{dx^2} = - \frac{1}{Z} \frac{d^2 Z}{dz^2} = - k^2 \quad (2.42)$$

where the constant  $k$  is the wave number. The general solutions for  $X(x)$  and  $Z(z)$  respectively are

$$X(x) = C_1 \sin(kx + \beta) \quad (2.43)$$

and

$$Z(z) = C_2 \cosh(kz + \alpha) \quad (2.43)$$

where  $C_1$  ,  $C_2$  ,  $\alpha$  and  $\beta$  are arbitrary constants. The particular solution of  $Z(z)$  is obtained by applying the boundary condition at the sea bed so that equation (2.43) is satisfied at  $z = -h$ . Hence

$$\frac{dZ}{dz} = C_2 k \sinh(-kh + \alpha) = 0 \quad (2.44)$$

from which  $\alpha = kh$ . Equation (2.43) therefore becomes

$$Z(z) = C_2 \cosh(kz + kh) \quad (2.45)$$

By substituting equations (2.41) and (2.45) into the linearized free-surface boundary condition (eqn. 2.39) the solution of the time function,  $T(t)$ , is

$$\left[ \frac{1}{g} \cosh(kz + kh) \frac{d^2 T}{dt^2} + \sinh(kz + kh) \right] \Big|_{z=0} = 0 \quad (2.46)$$

When the separation of variables is applied, equation (2.46) becomes

$$\frac{1}{T} \frac{d^2 T}{dt^2} + \omega^2 = 0 \quad (2.47)$$

where  $\omega$  is the wave circular frequency and is expressed as

$$\omega = [kg \tanh(kh)]^{0.5} \quad (2.48)$$

The general solution of equation (2.47) is

$$T(t) = C_3 \sin(\omega t + \gamma) \quad (2.49)$$

By equating the phase angles  $\beta$  and  $\gamma$  to zero and combining equations (2.43), (2.45) and (2.49), the solution to the differential equation according to equation (2.41) can now be expressed as

$$\Phi(x, z, t) = A \cosh(kz + kh) \sin(kx) \sin(\omega t) \quad (2.50)$$

where the arbitrary constants  $C_1$  ,  $C_2$  and  $C_3$  are now represented by the amplitude coefficient  $A$ .

Substituting for the velocity potential in the dynamic free-surface condition yields the expression for the displacement of the free surface of a standing wave:

$$\begin{aligned}\eta &= - \frac{1}{g} \frac{\delta\Phi}{\delta t} \Big|_{z=0} = - \frac{\omega A}{g} \cosh(kh) \cdot \sin(kx) \cdot \cos(\omega t) \\ &= a \sin(kx) \cdot \cos(\omega t)\end{aligned}\tag{2.51}$$

where  $a$  is the wave amplitude. By replacing the amplitude coefficient  $A$  in equation (2.50) by  $-ag/\omega \cosh(kh)$ , one obtains

$$\Phi(x, z, t) = - \frac{a g \cosh(kz + kh)}{\omega \cosh(kh)} \cdot \sin(kx) \sin(t)\tag{2.52}$$

From the combinations of the sine and cosine functions of  $x$  and  $t$ , there exist three additional standing wave solutions. The four standing waves are

$$\eta_1 = a \sin(kx) \cdot \cos(\omega t)\tag{2.53}$$

$$\eta_2 = a \cos(kx) \cdot \cos(\omega t)\tag{2.54}$$

$$\eta_3 = a \sin(kx) \cdot \sin(\omega t)\tag{2.55}$$

$$\eta_4 = a \cos(kx) \cdot \sin(\omega t)\tag{2.56}$$

Since the above expressions result from the solution of a linear equation, any pair can be superimposed to obtain solutions describing travelling waves:

$$\eta^- = \eta_1 + \eta_4 = a \sin(kx + \omega t)\tag{2.57}$$

for left-running waves, and

$$\eta^+ = \eta_2 + \eta_3 = a \cos(kx - \omega t)\tag{2.58}$$

for right-running waves. The velocity potential functions corresponding to equations (2.57) and (2.58) are respectively

$$\Phi^- = - \frac{a g \cosh(kz + kh)}{\omega \cosh(kh)} \cdot \cos(kx + \omega t)\tag{2.59}$$

and

$$\phi^+ = \frac{a g \cosh(kz + kh)}{\omega \cosh(kh)} \cdot \sin(kx + \omega t) \quad (2.60)$$

If the origin of the coordinate system is allowed to travel with the wave, then the argument of the cosine term in equation (2.58) is constant, or

$$kx - \omega t = \text{constant} \quad (2.61)$$

and the differential of the argument is

$$k dx - \omega dt = 0 \quad (2.62)$$

The wave velocity or celerity is therefore defined as

$$C = \frac{dx}{dt} = \frac{\omega}{k} = \frac{L}{T} = fL \quad (2.63)$$

where  $f$  is the wave frequency,  $L$  the wavelength, and  $T$  the wave period. The combination of equations (2.48) and (2.63) yields an expression for the wave celerity

$$C = \frac{g}{k} \tanh(kh) \quad (2.64)$$

and a transcendental equation for the wavelength

$$L = C T = \frac{g T^2}{2\pi} \tanh(2\pi h/L) \quad (2.65)$$

For deep water waves, customarily defined when the water depth is greater than twice the wavelength, or  $h/L > 2$ , Kinsman (1965), equation (2.65) reduces to

$$L = gT^2/2\pi \quad (2.66)$$

Similarly, for shallow water waves, commonly defined when the water depth to wavelength ratio is less than 1/25, or  $h/L < 1/25$ , Kinsman (1965),

equation (2.65) is written as

$$L = gT^2 h/L \quad (2.67)$$

In considering the fluid particle motion, equations (2.12) and (2.60) are combined to give the velocity components of the fluid in a right-running wave as

$$u = \frac{\delta\Phi}{\delta x} = \frac{a g k}{\omega} \frac{\cosh(kz + kh)}{\cosh(kh)} \cos(kx - \omega t) \quad (2.68)$$

and

$$w = \frac{\delta\Phi}{\delta z} = \frac{a g k}{\omega} \frac{\sinh(kz + kh)}{\cosh(kh)} \sin(kx - \omega t) \quad (2.69)$$

It is evident from equations (2.68) and (2.69) that the fluid particle velocities  $u$  and  $w$  vary sinusoidally in time with a mean position at a fixed point  $(x_0, z_0)$ . The fluid particle displacement equations are obtained by integration of the particle velocity equations with respect to time yielding

$$\xi = - \frac{a g k}{\omega^2} \frac{\cosh(kz_0 + kh)}{\cosh(kh)} \sin(kx_0 - \omega t) \quad (2.70)$$

for horizontal particle displacements and

$$\zeta = \frac{a g k}{\omega^2} \frac{\sinh(kz_0 + kh)}{\cosh(kh)} \cos(kx_0 - \omega t) \quad (2.71)$$

for vertical particle displacements.

It can be seen from equations (2.70) and (2.71) that the paths of the fluid particles about a mean position  $(x_0, z_0)$  are determined by the ratio of the water depth to the wavelength,  $h/L = kh/2\pi$ . For deep water waves ( $0.5 < h/L$ ) the fluid particles move in a circular path which radius decreases exponentially with depth. The fluid particles motion of intermediate depth waves ( $1/25 < h/L < 0.5$ ) follow an elliptic path with its

major and minor axes decreasing exponentially with depth. For waves in shallow water ( $0 < h/L < 1/20$ ), the fluid particles motion is approximated by an elliptic path with the major axis independent of depth as illustrated in figure 2.6.

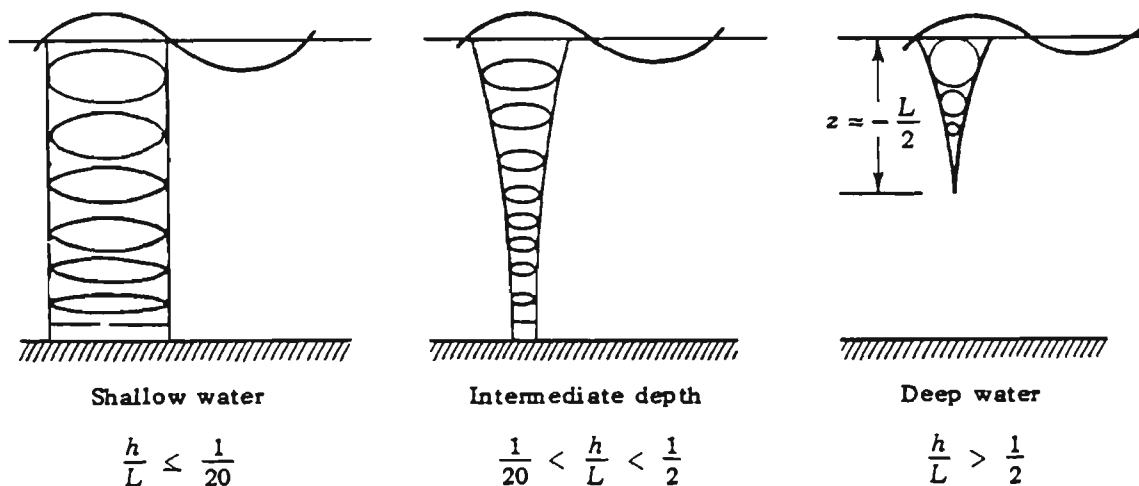


Figure 2.6. Effects of water depth on fluid particle paths.

#### 2.4. Finite Amplitude Waves.

The small amplitude wave theory, presented above, is founded on the premise that the fluid motions are sufficiently small to permit the linearization of the free surface boundary conditions. Alternatively the validity of the small amplitude wave theory may be defined by

$$\frac{H}{h} \ll 1 \quad \text{and} \quad \frac{H}{L} \ll 1 \quad (2.72)$$

or by the Ursell parameter

$$U_R = \frac{HL^2}{h^3} < 15 \quad (2.73)$$

Since these assumptions are no longer valid if the wave amplitudes are finite, it is necessary to retain the higher-order terms to achieve an accurate representation of the nonlinear wave motion to allow for cases where  $H/h$  and  $H/L$  approach 1. In order to eliminate the difficulties in developing a theory in which both  $H/h$  and  $H/L$  are defined over a certain range, it is assumed that either one of these parameters is small ( $H/h$  and

$H/L \ll 1$ ). The validity of various classical wave theories according to ranges of these important parameters are shown graphically in figure 2.7.

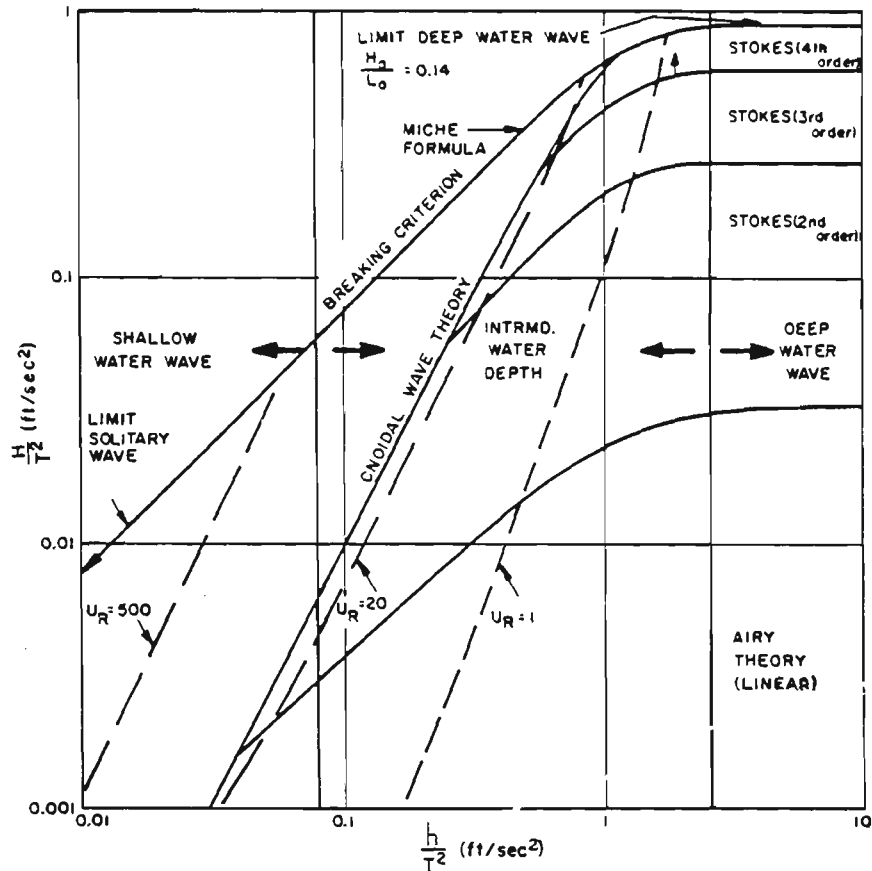


Figure 2.7. Classification of wave theories.  
- After Le Mehaute (1976) -

The formulation of the finite amplitude wave boundary value problem is basically the same as that presented for the small amplitude wave theory with the exception that the nonlinear higher order terms are retained. For convenience, it is generally assumed that a wave travels at a constant celerity  $c$  and with retention of its shape. A right-running wave of finite amplitude within a rectangular coordinate system, whose origin travels with the wave crest at a velocity  $c$ , as shown in figure 2.8, is considered. Since, as in the analysis of linear small amplitude waves, the fluid is assumed to be incompressible and irrotational, Laplace's equation is applied

$$\frac{\delta^2 \Phi}{\delta x^2} + \frac{\delta^2 \Phi}{\delta y^2} + \frac{\delta^2 \Phi}{\delta z^2} = 0 \quad (2.74)$$

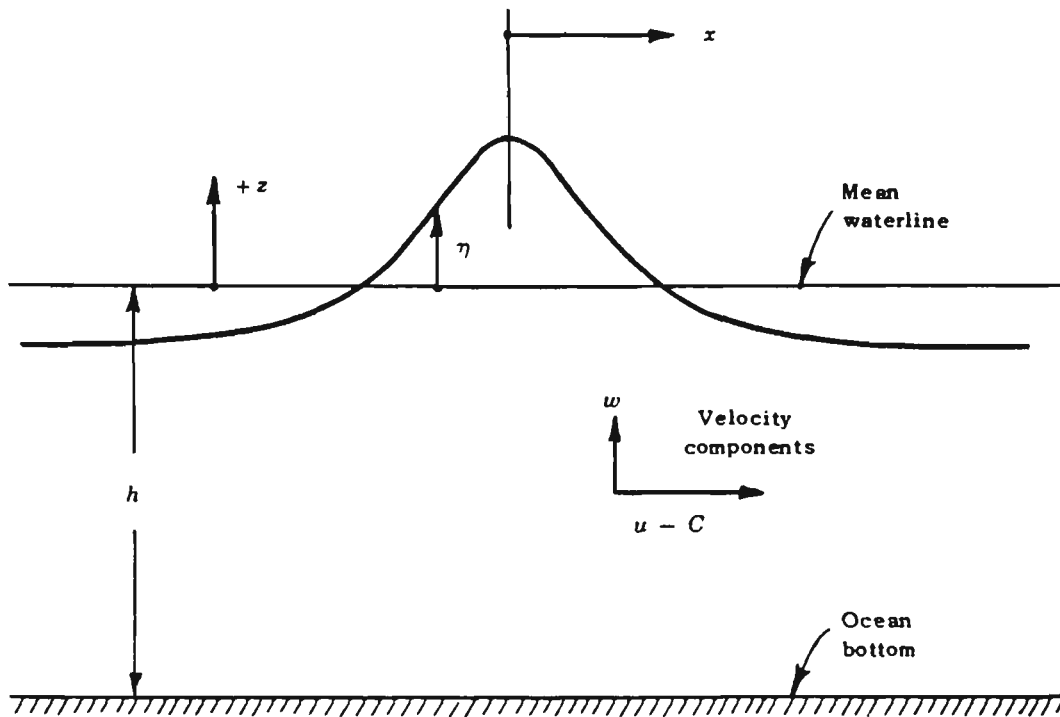


Figure 2.8. A stationary finite amplitude wave.

The boundary condition at the bottom is such that there is no flow across the boundary and is written as

$$w = - \frac{\delta\Phi}{\delta z} = 0 \quad \text{at } z = -h \quad (2.75)$$

There are two boundary conditions at the (stationary) free surface that must be satisfied. The dynamic boundary condition is the requirement that the total energy along the free surface remains constant. This is expressed as Bernoulli's equation applied to the quasi-steady flow at the surface

$$\eta + \frac{1}{2g} (u - C)^2 + w^2 = Q \quad \text{at } z = \eta \quad (2.76)$$

Where  $Q$  is the fluid flow at the surface. It must be noted that the nonlinear terms  $u^2$  and  $w^2$  are now retained, unlike in the development of the small amplitude wave theory.

The kinematic free surface boundary condition requires that no fluid be transported across the free surface. This can be formulated by specifying that the resultant vector of the fluid velocity at the free surface be tangent to the free surface.

$$\frac{\delta\eta}{\delta x} = \frac{w}{(u - C)} \quad \text{at } z = \eta \quad (2.77)$$

Equation (2.77) may be expanded by the Maclaurin series in which

$$\frac{1}{(1 - k)} = \sum_{n=0}^{\infty} k^n = 1 + k + k^2 + k^3 + \dots \quad (2.78)$$

Since

$$\frac{\delta\eta}{\delta x} = \frac{w}{(u - C)} = - \frac{w}{C} \frac{1}{(1 - u/C)} \quad (2.79)$$

then equation (2.77) becomes

$$\begin{aligned} \frac{\delta\eta}{\delta x} &= \sum_{n=0}^{\infty} - \frac{w}{C} \left(\frac{u}{C}\right)^n \\ &= - \frac{w}{C} - \frac{wu}{C^2} - \frac{wu^2}{C^3} - \frac{wu^3}{C^4} - \dots \\ &= - \frac{w}{C} \left[ 1 + \frac{u}{C} + \left(\frac{u}{C}\right)^2 + \left(\frac{u}{C}\right)^3 + \dots \right] \end{aligned} \quad (2.80)$$

In summary, the derivation of an accurate finite amplitude wave theory was achieved by finding a solution to Laplace's equation which satisfies the boundary conditions as expressed in equations (2.75), (2.76) and (2.77).

## 2.5. Stokes Wave Theory.

The nonlinear Stokes wave theory was developed by assuming that the solutions to the properties of wave motion, such as the velocity potential, the free surface displacement and the wave celerity can be represented by a series of small perturbations expressed as

$$\Phi = \sum_{n=1}^{\infty} \epsilon^n \Phi_n \quad (2.81)$$

$$\eta = \sum_{n=1}^{\infty} \epsilon^n \eta_n \quad (2.82)$$

and

$$\Phi = C_* + \sum_{n=1}^{\infty} \epsilon^n C_n \quad (2.83)$$

Where  $C_*$  is the lowest order celerity term and is equivalent to equation (2.64). In the solutions above, the sum of the terms up to index  $n$  represent the  $n^{\text{th}}$  order theory. Accordingly, as the number of terms increases, so does the accuracy of approximation to the actual wave properties. The solutions to equations (2.81), (2.82) and (2.83) are obtained by successive approximations and require numerous and detailed calculations of the coefficients and parameters in which small errors often occur. Consequently, there often exist differences in the final results of various investigators. As the development of Stokes theory is rather involved, the reader is referred to Kinsman (1965) for a thorough review of Stokes perturbation method.

The results of Stokes first order analysis are identical to those of the linear, small amplitude wave theory.

When extended to the second order, the solutions to the finite amplitude Stokes analysis are, for the velocity potential:

$$\begin{aligned} \Phi = \frac{H}{2} C \frac{\cos(kh + kz)}{\sinh(kh)} \cdot \sin(kx - \omega t) + \\ \frac{H^2}{4} \frac{3\pi C}{4L} \frac{\cosh(2kh + 2kz)}{\sinh^4(kh)} \cdot \sin(2kx - 2\omega t) \end{aligned} \quad (2.84)$$

for the free surface displacement:

$$\eta = \frac{H}{2} \cos(kx - \omega t) + \frac{H^2}{4} \frac{\pi \cosh(kh)}{2L \sinh^3(kh)} \cdot [2 + \cosh(2kh)] \cos(2kx - 2\omega t) \quad (2.85)$$

and for the wave celerity:

$$C = \frac{g}{k} \tanh(kh) = C_* \quad (2.86)$$

The wavelength is given by

$$L = \frac{gT^2}{2\pi} \tanh(2\pi h/L) \quad (2.87)$$

The first term of the free surface profile (eqn. 2.85) is the same as the solution to free surface profile of the linear small amplitude theory while the remaining term is the second order correction for nonlinearity. However, the expressions for the celerity and the wavelength are identical to those described for the first order small amplitude theory.

Unlike the linear theory, Stokes' second order theory describes a wave form that is asymmetrical about the mean water level as shown in Figure 2.9.

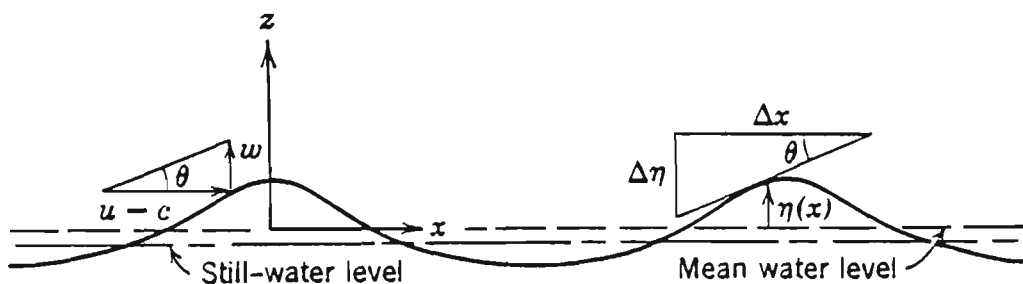


Figure 2.9. Second order Stokes wave.

Solutions for the third and higher order Stokes waves that take into account more terms to improve the approximation have been derived and are given in the Shore Protection Manual (1984).

Stokes higher order theories are only valid when the Ursell parameter is very small, namely, for steep waves in deep water.

## 2.6. Cnoidal Wave Theory.

Long waves of finite amplitude in shallow water are presently best described by the cnoidal wave theory. It is based on the assumption that the square of the slope of the water surface is small relative to unity. The cnoidal wave is periodic and has sharp crests separated by wide troughs as shown in Figure 2.10. The surface profile of the cnoidal wave is given by the Jacobian elliptical cosine function, hence the term cnoidal. Solutions for the cnoidal water surface profile, wave celerity and wavelength may be found in the Shore Protection Manual (1984).

The cnoidal wave theory is considered only valid for  $h/L < 1/8$  and  $U_R > 26$ . As the wave height becomes small relative to the water depth, the wave profile approaches a sinusoidal profile as predicted in the linear small amplitude theory. However, when the wavelength increases and approaches infinity, the cnoidal wave theory reduces to the solitary wave theory.

## 2.7. Solitary Wave Theory.

The solitary wave theory describes a wave of permanent form and of infinite wavelength. A solitary wave is neither oscillatory nor does it have a trough as it lies entirely above the still water level. The profile of a solitary wave is illustrated in figure 2.10. Equations defining the solitary wave profile and the wave celerity are outlined in the Shore Protection Manual (1984).

## 2.8. Stream Function Wave Theory.

A numerical approximation to solutions of the hydrodynamic equations describing wave motion have been proposed by Dean (1965). The stream function wave theory (more accurately described as a procedure), is a nonlinear theory based on a stream function representation of the flow. The theory is similar to that of Stokes in that it is constructed in terms of sine or cosine functions that satisfy the original differential equation (Laplace's equation). However, the coefficient of each higher order term is determined numerically such that errors in the solution to the dynamic free surface boundary conditions are minimized.

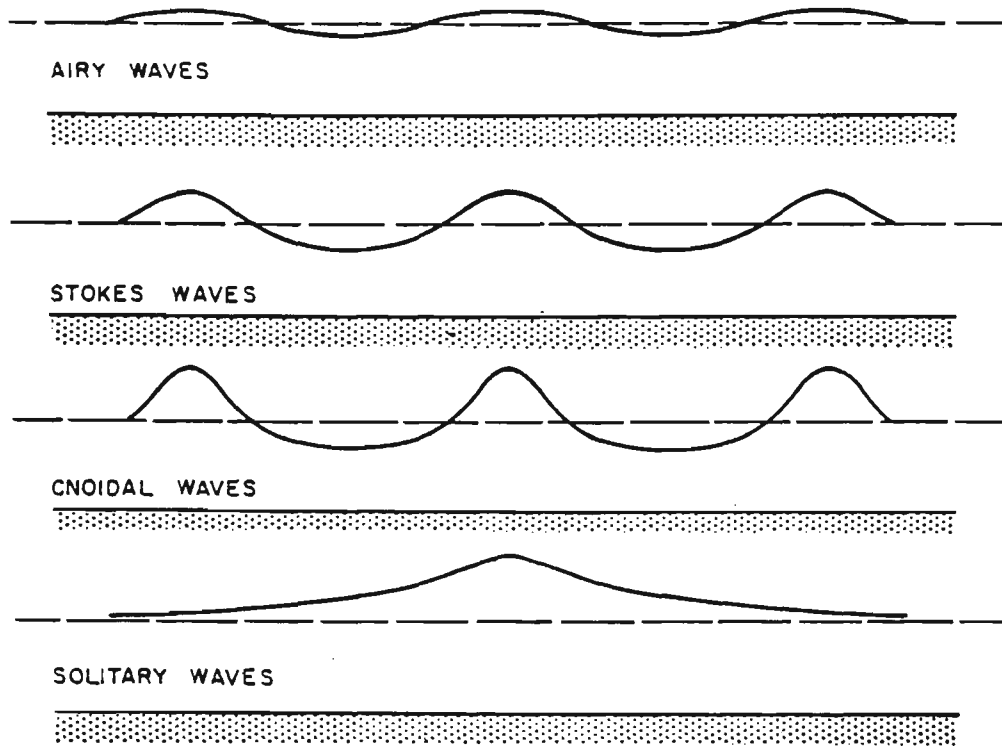


Figure 2.10. Illustration of various wave profiles.

### 2.9. Wave Superposition - Small Amplitude Waves.

Due to the linearity of Laplace's equation for small amplitude waves, the total velocity potential of the wave field,  $\Phi_T$ , is equal to the sum of the velocity potential of each individual wave:

$$\Phi_T = \sum_{n=1}^N \Phi_n \quad (2.88)$$

where  $N$  is the total number of individual waves and

$$\Phi_n = \frac{a_n g}{\omega_n} \frac{\cosh(k_n z + k_n h)}{\cosh(k_n h)} \cdot \cos(k_n x + \omega_n t + \delta_n) \quad (2.89)$$

in which  $\delta_n$  is an arbitrary phase relationship between various individual waves.

By applying the linear boundary conditions for small amplitude waves, as in section 2.3, the resulting water surface displacement is given by

$$\eta_T = \sum_{n=1}^N \eta_n \quad (2.90)$$

When a number of small amplitude waves travelling in the same direction in water of constant depth are considered, the water surface displacement may be written as

$$\eta_T = \sum_{n=1}^N a_n \sin(k_n x - \omega_n t + \delta_n) \quad (2.91)$$

If the frequency of each individual wave is the same then

$$\omega_1 = \omega_2 = \omega_3 = \dots \omega_n \quad (2.92)$$

and

$$k_1 = k_2 = k_3 = \dots k_n \quad (2.93)$$

Using the trigonometric identity

$$\sin(A + B) = (\sin A \cdot \cos B) + (\cos A \cdot \sin B) \quad (2.94)$$

equation (2.91) may be written as

$$\eta_T = \sin(kx - \omega t) \sum_{n=1}^N a_n \cos(\delta_n) + \cos(kx - \omega t) \sum_{n=1}^N a_n \sin(\delta_n) \quad (2.95)$$

If the summations in equation (2.95) are substituted such that

$$\sum_{n=1}^N a_n \cos \delta_n = r \cos \lambda \quad (2.96)$$

and

$$\sum_{n=1}^N a_n \sin \delta_n = r \sin \lambda \quad (2.97)$$

then equation (2.95) becomes

$$\eta_T = r \sin(kx - \omega t) \cos(\lambda) + r \cos(kx - \omega t) \sin(\lambda) \quad (2.98)$$

or

$$\eta_T = r \sin(kx - \omega t + \lambda) \quad (2.99)$$

where  $r$  and  $\lambda$  are dependents of the amplitudes and phases of the individual waves and are written as

$$r = \left[ \left( \sum_{n=1}^N a_n \cos \delta_n \right)^2 + \left( \sum_{n=1}^N a_n \sin \delta_n \right)^2 \right]^{0.5} \quad (2.100)$$

and

$$\lambda = \tan^{-1} \left[ \frac{\sum_{n=1}^N a_n \sin \delta_n}{\sum_{n=1}^N a_n \cos \delta_n} \right] \quad (2.101)$$

This resulting harmonic oscillation is best illustrated when presented in polar coordinates as shown in figure 2.11.

When two harmonic progressive waves of the same frequency travelling in opposite directions are combined, the resulting water surface displacement, obtained by addition of each individual wave, is written as

$$\eta_T = a_1 \sin(k_1 x - \omega_1 t + \delta_1) + a_2 \sin(k_2 x + \omega_2 t + \delta_2) \quad (2.102)$$

Again, by using the trigonometric identity of equation (2.94) equation (2.102) becomes

$$\eta_T = a_1 \sin(kx - \omega t) + a_2 \cos \delta_2 \sin(kx + \omega t) + a_2 \sin \delta_2 \sin(kx + \omega t) \quad (2.103)$$

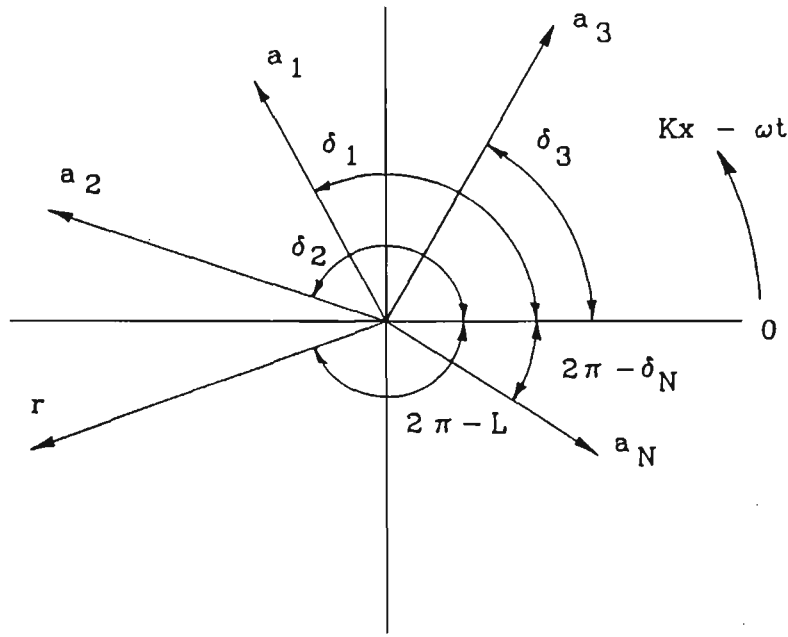


Figure 2.11. Polar representation of common harmonics of arbitrary phase.

When the above wave system is considered such that the outgoing wave is generated by the perfect reflection of the oncoming wave from a vertical wall, the amplitude of the reflected (outgoing) wave will be the same as that of the incident (oncoming) wave. Since the wave frequency  $\omega$ , and hence the wave number  $k$ , are assumed to remain constant, the reflection coefficient,  $K_r$ , defined as the ratio of the amplitude of the incident wave to the amplitude of the reflected wave, or

$$K_r = a_2/a_1 \quad (2.104)$$

must be equal to unity.

The velocity potential of the wave system is obtained by superposition of the velocity potential of each individual wave and is written as

$$\phi_T = \frac{a g}{\omega} \frac{\cosh(kz + kh)}{\cosh(kh)} [\cos(kx - \omega t) - \cos(kx + \omega t + \delta_2)] \quad (2.105)$$

The boundary condition at the impermeable plane vertical wall ( $x = B$ ) is such that the horizontal partical velocity,  $u_T$ , is zero or

$$u_T = - \frac{\delta \Phi_T}{\delta x} = 0 \quad \text{at } x = B \quad \text{for all } t \quad (2.106)$$

By differentiating equation (2.105) and applying the above boundary condition at  $x = B$

$$\sin(kB - \omega t) = \sin(kB + \delta_2) \quad (2.107)$$

Applying the trigonometric identity of equation (2.94),

$$\begin{aligned} \sin(kB) \cos(\omega t) - \cos(kB) \sin(\omega t) &= \sin(kB + \delta_2) \cos(\omega t) \\ &+ \cos(kB + \delta_2) \sin(\omega t) \end{aligned} \quad (2.108)$$

and equating the sinusoidal and cosinusoidal components,

$$\sin(kB) = \sin(kB + \delta_2) \quad (2.109)$$

and

$$\cos(kB) = - \cos(kB + \delta_2) \quad (2.110)$$

It follows that

$$\delta_2 = \pi(2n + 1) - 2kB \quad \text{for } n = 0, 1, 2, \dots \quad (2.111)$$

By substituting for  $\delta_2$  in equation (2.103), and expanding

$$\begin{aligned} \eta_T &= a \sin(2kB) \cos(kx) \cos(\omega t) - a \sin(2kB) \sin(kx) \sin(\omega t) \\ &\quad - a \cos(kx) \sin(\omega t) - a \cos(2kB) \sin(kx) \cos(\omega t) \\ &\quad + a \sin(kx) \cos(\omega t) - a \cos(2kB) \cos(kx) \sin(\omega t) \end{aligned} \quad (2.112)$$

By introducing the following trigonometric identities:

$$\sin(2kB) = 2 \sin(kB) \cos(kB) \quad (2.113)$$

and

$$\cos(2kB) = 2 \cos^2(kB) - 1 = 1 - 2 \sin^2(kB) \quad (2.114)$$

equation (2.112) reduces to

$$\eta_T = 2a \sin(kB - \omega t) \cos(kx - kB) \quad (2.115)$$

which is the equation for a standing wave or clapotis, the nodes of which are located at

$$\cos(kx - kB) = 0 \quad (2.116)$$

or

$$x_{\text{node}} = B - \frac{\pi(2n + 1)}{2k} \quad \text{for } n = 0, 1, 2, \dots \quad (2.117)$$

and the antinodes at

$$\cos(kx - kB) = + 1 \quad (2.118)$$

or

$$x_{\text{antinode}} = B - \pi n/k \quad \text{for } n = 0, 1, 2, \dots \quad (2.119)$$

If the boundary,  $B$ , is made to be at  $x = 0$ , the phase of the reflected wave is reduced to  $\delta_2 = \pi(2n + 1)$ . Consequently, for  $n = 0$ , equation (2.115) reduces to

$$\eta_T = - 2a \sin(\omega t) \cos(kx) \quad (2.120)$$

When energy dissipation and/or transmission occurs, the reflection is not perfect and the reflection coefficient,  $K_r$ , will therefore be less than unity.

Again, by applying the principle of superposition, the resultant water surface displacement, given by the addition of the incident and reflected

waves, is written as

$$\eta_T = a_1 \sin(kx - \omega t) + a_2 \sin(kx + \omega t + \delta_2) \quad (2.121)$$

If it is assumed that the incident wave is partially reflected from a vertical wall located at  $x = 0$  and that the phase of the reflected wave is  $\pi$  as for the perfect reflection case, then equation (2.121) reduces to

$$\eta_T = a_1 \sin(kx - \omega t) - K_r a_1 \sin(kx + \omega t) \quad (2.122)$$

where  $K_r a_1 = a_2$

The addition and subtraction of the term  $K_r a_1 \sin(kx - \omega t)$  yields

$$\eta_T = a_1(1-K_r)\sin(kx - \omega t) - 2K_r a_1 \sin(\omega t) \cos(kx) \quad (2.123)$$

in which a progressive wave and a standing wave are represented by the first and second terms respectively. It can be seen that, as the reflection coefficient increases, the amplitude of the progressive wave component decreases, and, in the limit when  $K_r = 1$ , equation (2.123) reduces to equation (2.120). Alternatively, equation (2.123) may be written as

$$\eta_T = a_1(1-K_r)\sin(kx) \cos(\omega t) - a_1(1+K_r) \cos(kx) \sin(\omega t) \quad (2.124)$$

The time at which extremes of  $\eta_T$  at any location,  $x$ , occur may be obtained by differentiating equation (2.124) with respect to time, thus

$$\left. \frac{\delta \eta_T}{\delta t} \right|_x = 0 \quad (2.125)$$

resulting in

$$[\omega t]_{\eta_{T\max}} = \tan^{-1} \left[ - \frac{a_1(1 + K_r)}{a_1(1 - K_r)} \cot(kx) \right] \quad (2.126)$$

By substituting  $\eta_{T\max}$  and  $\eta_T$  into equation (2.124), the location,  $x$ , at which these extremes occur may be found by setting the derivative of  $\eta_{T\max}$  with respect to  $x$  to zero,

$$\frac{\delta \eta_{Tmax}}{\delta x} = 0 \quad (2.127)$$

resulting in

$$[kx]_{\eta_{Tmax}} = n\pi \quad \text{and} \quad \frac{\pi}{2} (2n + 1) \quad (2.128)$$

where  $n = 0, 1, 2, \dots$

Substituting for  $\omega t$  and  $kx$  into equation (2.124), it can be seen that the resulting function describes a "standing" wave in that the amplitude envelope is stationary with extremes  $a_l$  and  $a_h$  at the nodes and antinodes respectively, where

$$a_l = a_1(1 - K_r) \quad (2.129)$$

$$a_h = a_1(1 + K_r) \quad (2.130)$$

The reflection coefficient may therefore be obtained from the envelope of the wave amplitudes from

$$K_r = \frac{a_h - a_l}{a_h + a_l} \quad (2.131)$$

or, for small amplitude waves where  $H = 2a$ ,

$$K_r = \frac{H_h - H_l}{H_h + H_l} \quad (2.132)$$

where  $H_h$  and  $H_l$  are defined in figure 2.12.

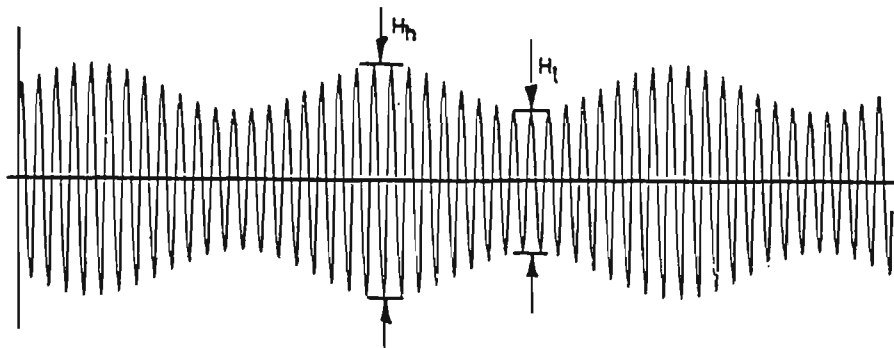


Figure 2.12. Nodes and antinodes of wave envelope.

### 3. STATISTICAL ANALYSIS OF OCEAN WAVES

#### 3.1. Spectral Analysis of Random Processes.

The study of ocean waves has developed as a combination of time series analysis and statistical geometry governed by the laws of hydrodynamics. In this chapter nondeterministic methods of describing the structure of the wave disturbed water surface are presented. The basic ideas of spectral analysis are first considered followed by a review of spectral models of ocean waves. The probability distributions of sea surface parameters, which give concise and useful properties of water waves, are also examined.

Random processes are generally classified into three categories: (1) nonstationary, (2) stationary and (3) stationary and ergodic. A random process is said to be stationary when the governing statistical characteristics are time invariant. A stationary process is ergodic if any finite record is completely representative of the whole, infinite process. Since any record of ocean wave data is of finite duration, ergodicity has to be assumed. Furthermore, since it is never possible to demonstrate ergodicity, one is forced to make the ergodic assumption.

Although no two wave records are ever identical, they will possess certain identifiable statistical properties. Sverdrup and Munk (1947) characterised a random sea by introducing the concept of the significant wave. Where the variety of wave forms is great, such as in a random sea, characterisation by a single wave form is inconsistent with the random nature of the process.

Longuet-Higgins (1957) described ocean waves by treating the random process as a combination of an infinite number of monochromatic waves of different amplitude, frequencies, directions and phases expressed as

$$\eta(x,y,t) = \sum_{n=1}^{\infty} a_n \cos(k_n x \cos\theta_n + k_n y \sin\theta_n - 2\pi f_n t + \delta_n) \quad (3.1)$$

where  $a$  is the wave amplitude,  $k$  is the wave number,  $\theta$  is the wave direction,  $f$  is the wave frequency and  $\delta$  is the phase angle.

Although the correctness of this interpretation of random ocean waves as a linear superposition of free progressive waves cannot be proven, it has been successfully used to characterise most properties of ocean waves. This interpretation of ocean waves rests on four conditions: (1) the frequencies  $f_n$  must be densely distributed between zero and infinity such that an infinitesimal interval  $df$  contains an infinite number of frequencies  $f_n$ . (2) the wave directions  $\theta_n$  must be densely distributed between  $-\pi$  and  $\pi$  such that an infinitesimal interval  $d\theta$  contains an infinite number of directions  $\theta_n$ . (3) the phase angle  $\delta_n$  must be randomly and uniformly distributed between 0 and  $2\pi$ . And (4) although the amplitude of each wave is infinitely small, the summation of  $a_n^2$  should have a finite and unique value  $G(f, \theta)$  expressed as

$$\sum_f^{f+df} \sum_\theta^{\theta+d\theta} 0.5 a_n^2 = G(f, \theta) df d\theta \quad (3.2)$$

The directional wave spectrum  $G(f, \theta)$  defined by equation (3.2) is an expression of the distribution of wave energy with respect to frequency and direction. When waves are observed at a fixed single point in the ocean, the wave profile is expressed as

$$\eta(t) = \sum_{n=1}^{\infty} a_n \cos(2\pi f_n t + \delta_n) \quad (3.3)$$

The sum of the squares of the wave amplitudes over an interval  $f$  to  $f+df$  is given by

$$\sum_f^{f+df} 0.5 a_n^2 = G(f) df \quad (3.4)$$

which represents the wave energy distribution with respect to frequency, irrespective of the wave direction and is called the frequency spectrum. In this study only two-dimensional and unidirectional waves will be

considered. Random waves will therefore be represented in the frequency domain by the frequency spectrum . The use of spectral or frequency analysis to describe ocean waves has now been well established and is discussed by Kinsman (1965).

Linear physical systems are defined as being additive and homogeneous. Specifically, a system is additive when the response to a sum of inputs equals the sum of the responses due to each individual input. If  $y(x)$  is the response to an input  $x_i$  then

$$y(x_1 + x_2) = y(x_1) + y(x_2) \quad (3.5)$$

A system is considered homogeneous if the response to a an input,  $x$  , times a constant,  $c$ , is equal to the constant times the response of the input alone, or

$$y(cx) = c y(x) \quad (3.6)$$

Consequently, when the random input into a linear system is Gaussian, the response will also be Gaussian.

The mathematical basis of spectral analysis is the Fourier Transform which assumes that the signal is composed of a number of sinusoidal or cosinusoidal components of various frequency, amplitude and initial phase. The one-sided discrete Fourier Transform of a sampled time signal  $g(t)$  is given by

$$G(f_k) = \frac{1}{N} \sum_{n=0}^{N-1} g(t_n) \exp(-j2\pi nk/N) \quad (3.7)$$

where  $k$  and  $n$  are positive integers. It can be seen from equation (3.7) that in order to obtain  $N$  frequency components from  $N$  time samples requires  $N^2$  complex multiplications. Since its introduction in the mid 1960's, the algorithm known as the Fast Fourier Transform or FFT which obtains the same results with  $N \log_2(N)$  complex multiplications has been widely used. Stationary random time signals which have a finite and statistically constant power are more commonly represented in the frequency domain by the

Power Spectral Density, or PSD, which has the units of energy per unit frequency or, in the case of water surface elevation,  $m^2/Hz$ .

The frequency response function of a system represents the output to input ratio in the frequency domain and as such characterises stable, linear, stationary systems. The relationships between the input signal  $a(t)$  and the output  $b(t)$  of a stable, linear, stationary system in the absence of noise are shown in figure 3.1.

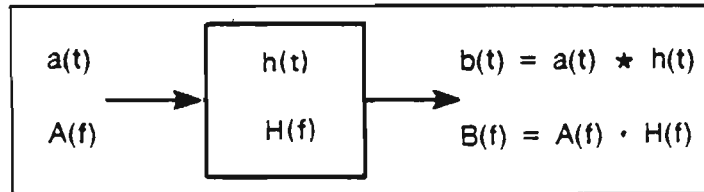


Figure 3.1. Linear system input - output relationships

The system is characterised in the time domain by its impulse response  $h(t)$  and the output signal  $b(t)$  is the convolution of  $a(t)$  with  $h(t)$  or

$$b(t) = a(t) * h(t) \quad (3.8)$$

where  $*$  indicates convolved with. Application of the convolution theorem yields

$$B(f) = A(f) H(f) \quad (3.9)$$

where  $A(f)$  is the Fourier transform of  $a(t)$ ,  $B(f)$  that of  $b(t)$  and  $H(f)$  that of  $h(t)$ . A more thorough discussion of the convolution theorem is presented by Randall (1987).

The frequency response function,  $H(f)$ , of the linear system in the absence of noise is obtained by

$$H(f) = B(f)/A(f) \quad (3.10)$$

If noise is present in the output signal, errors in the result are minimized by multiplying the numerator and denominator of equation (3.10) by the complex conjugate of the Fourier transform of the input thus,

$$H_1(f) = \frac{B(f)}{A(f)} \frac{A^*(f)}{A^*(f)} = \frac{G_{AB}(f)}{G_{AA}(f)} \quad (3.11)$$

which represents the one-sided cross spectrum normalised by the one-sided autospectrum of the input.

It has been shown by Bendat and Piersol (1971 & 1986) that the normalized standard error (random portion of estimation error) in spectral density estimates of a stationary (ergodic) Gaussian random process, obtained by the Fourier Transform, is a function of the bandwidth,  $B_e$  (Hz), of the measurement and the record length  $T$  (sec) written as

$$\epsilon_r = 1/(B_e T)^{0.5} \quad (3.12)$$

For a raw spectral estimate, it turns out that

$$B_e = \Delta f = 1/T \quad (3.13)$$

It follows, from equation (3.12), that the normalized standard error of a raw spectral estimate is unity. This indicates that the standard deviation of the estimate is equal to the value of the estimate, hence poor accuracy is obtained.

The distribution of each frequency component of the estimate may be approximated by a chi-square distribution,  $\chi_n^2$ , with the number of statistical degrees of freedom,  $n$ , being 2.

Furthermore, it can be seen from equations (3.12) and (3.13) that an increase in record length will not yield improvement of the random error of spectral estimates.

The accuracy of spectral estimates may be improved by two methods. The first is by ensemble averaging, in which the average of a number,  $N_d$ , of

raw spectral estimates from independent sample records is computed. This method requires the measurement and analysis of a number of independent records. The second method of improving the accuracy of spectral estimates is by smoothing of the estimate over frequency by averaging a number of adjacent spectral components according to one of several weighting functions. Smoothing by this method is usually performed on the estimate from a single sample record. This technique is only valid under the assumption that the spectral density varies only gradually with respect to frequency.

If  $p$  adjacent frequency components of the raw spectral estimates are averaged, the smoothed spectral estimate will be a  $\chi^2$  variable with approximately  $n = 2p$  degrees of freedom. The resulting effective resolution bandwidth becomes

$$B_e = p/T \quad (3.14)$$

so that the normalized standard error is given by

$$\epsilon_r = 1/(p)^{0.5} \quad (3.15)$$

Similarly for ensemble averaging

$$\epsilon_r = 1/(N_d)^{0.5} \quad (3.16)$$

where  $N_d$  is the number of raw spectral estimates, and for a combination of both frequency smoothing and ensemble averaging, the normalized standard error is given by

$$\epsilon_r = 1/(p N_d)^{0.5} \quad (3.17)$$

It can be seen from the above analysis that smoothing of raw spectral estimates by averaging adjacent estimates always results in loss of resolution in the frequency domain. A compromise must therefore always be arrived at in specifying the number of ensembles (number of spectral estimates) to be averaged and/or the frequency bandwidth of the weighting function.

### 3.2. Spectral Models of Ocean Waves.

There have been numerous attempts at formulating mathematical spectral models of ocean waves and there now exists a number of empirical and semi-empirical frequency spectrum models. These mathematical models, generally based on one or more parameters such as the significant wave height, wave period, shape factor, wind velocity, etc., are usually derived from experimental ocean wave records and hydrodynamic theories.

The Neumann spectral model was developed in 1953 and is expressed in terms of prevalent wind velocity,  $U_w$ , and is written as

$$G(\omega) = B\omega^{-6} \exp[-2g^2/(\omega U_w)^2] \quad (3.19)$$

In which  $B$  is a dimensional constant. As one of the earlier mathematical models, it was derived from limited data. With later developments in measurement techniques, the shortcomings of this model have been demonstrated and it is now regarded as outdated.

The majority of recent spectral models are based on the spectral function proposed by Phillips (1958) who defined the equilibrium range of the frequency spectrum for a fully developed sea as

$$G(\omega) = \alpha g^2 (\omega)^{-5} \quad (3.18)$$

where  $\alpha$  is the Phillips constant,  $g$  the acceleration due to gravity and  $\omega$  the angular wave frequency.

Although seldom employed in practice, the Phillips spectrum has been used as a basis for the formulation of other spectral models.

The Bretshneider spectrum, developed in 1959, may be used to represent fully-developed sea conditions. The model is based on the assumptions that the spectrum is narrow-banded and that the distribution of the wave height and wave period follow the Rayleigh distribution. It is written as

$$G(\omega) = 0.1687(H_s)^2 (\omega_s)^4 (\omega)^{-5} \exp[-0.675(\omega_s/\omega)^4] \quad (3.22)$$

where  $H_s$  is the significant wave height in feet,  $T_s$  the significant wave period in seconds defined as the average period of the significant waves and  $\omega_s = 2\pi T_s$ .

In 1964, a slight modification to the Bretshneider spectrum was suggested at the International Ship Structures Congress. The ISSC spectrum is written as

$$G(\omega) = 0.1107(H_s)^2 (\bar{\omega})^4 (\omega)^{-5} \exp[-0.4427(\omega/\omega)^4] \quad (3.23)$$

where  $\bar{\omega} = 1.296 \omega_0$  in which  $\omega_0$  is the spectral peak frequency.

Pierson and Moskowitz (1964) developed a spectral model also based on wind velocity. This model, commonly referred to as the P-M spectrum, is based on more accurately recorded data and represents a fully developed sea state. It is formulated on the assumptions that the wind has blown at a steady velocity and fixed direction for many hours over a large area.

Despite the fact that the model is derived from steady sea and wind conditions and that ocean waves rarely approach a fully developed sea state, it has been widely used in the design of offshore structures to represent severe storms. The P-M spectrum is

$$G(\omega) = \alpha g^2 \omega^{-5} \exp[-0.74(\omega U_w/g)^{-4}] \quad (3.20)$$

Where  $\alpha = 0.0081$

and  $U_w =$  prevalent wind velocity [ft/s] at 54 ft above the mean sea level.

Alternatively, the P-M spectrum may be expressed in terms of spectral peak frequency,  $\omega_0$ , as

$$G(\omega) = \alpha g^2 \omega^{-5} \exp[-1.25(\omega/\omega_0)^{-4}] \quad (3.21)$$

The International Towing Tank Conference (ITTC) spectrum is a modified version of the P-M spectrum and is defined in terms of the significant wave height and the average zero crossing frequency.

The P-M, Bretshneider, ISSC and ITTC spectral models are of the same class and may all be described by a two parameter spectrum expressed in terms of a statistical wave height and a characteristic wave period as shown by Chakrabarti (1987). Since the P-M based and Bretshneider based spectral models rely on wind speed measurements taken at different heights above the water surface, the difference between the two forms may be considerably reduced by taking into account the gradients of the wind velocity with respect to altitude.

The Scott spectral model, developed in 1965, is independent of wind speed, fetch or duration and was formulated to represent the spectrum of a fully-developed sea. It is expressed in terms of significant wave height and spectral peak frequency as,

$$G(\omega) = 0.214 H_s^2 \exp \left[ - \left( \frac{(\omega - \omega_0)^2}{0.065(\omega - \omega_0 + 0.26)} \right)^{0.5} \right]$$

for  $-0.26 < (\omega - \omega_0) < 1.65$  (3.25)

$$G(\omega) = 0 \quad \text{elsewhere}$$

where  $H_s$  is the significant wave height in feet.

Derived from wave data recorded on Lake Michigan, the Liu spectral model was developed in 1971 and contains a fetch-dependence parameter. The model is similar in form to the P-M spectrum and is written as,

$$G(\omega) = \alpha g^2 (X_0)^{-0.25} (\omega)^{-5} \exp[-\beta(\omega U_*/g)^{-4} X_0^{-4/3}] \quad (3.26)$$

where  $\alpha = 0.4$ ,  $\beta = 5500$ ,  $X_0 = gX/U_*^2$  and  $U_* = U_w(U_w^2/gX)^{1/3}$  in which  $U_w$  is the wind velocity at 10 metres.

Mitsuyasu (1972) proposed another fetch-limited spectral model based on data recorded from waves generated in a laboratory and in a bay. Unlike an earlier model, which did not give consistent results at low frequencies, this revised model of the fetch limited spectrum consists of two parts and is written as,

$$G(\omega) = \alpha g^2 (\omega)^{-5} \exp[\beta(\omega U_*/g)^{-4} (X_0)^{0.312}] \quad 0.3\omega_0 < \omega < \omega_0 \quad (3.27)$$

where  $\alpha = 9.12 \times 10^{-10}$  and  $\beta = 3.55$ , and

$$G(\omega) = \alpha g^2 (\omega)^{-5} (X_0)^{-0.308} \quad \omega > \omega_0 \quad (3.28)$$

where  $\alpha = 0.589$ .

Since both the Liu and Mitsuyasu spectra are fetch dependent and are based on lakes and reservoirs of limited fetch, they may have limited application in ocean conditions.

The JONSWAP spectrum was developed during the Joint North Sea Wave Project by Hasselman et. al. (1973). The model was derived from experimental data based on unsaturated (or not fully developed) sea conditions. Comparison between the experimental JONSWAP spectrum and the P-M spectrum showed discrepancies near the spectral peak. The JONSWAP model is therefore basically the P-M model with an additional peak enhancement function and is expressed in terms of five parameters. Even though three of the five parameters may be reduced to constants via empirical relationships, the model is somewhat inaccurate and inconvenient to use since the agreement between some of these empirical formulae and the data are rather crude as shown by Hasselman et. al. (1976). The JONSWAP spectrum is written as

$$G(\omega) = \alpha g^2 \omega^{-5} \exp[-1.25(\omega/\omega_0)^{-4}] \gamma \exp[-(\omega-\omega_0)^2/(2\tau^2\omega_0^2)] \quad (3.24)$$

Where  $\gamma$  is the peakedness parameter and  $\tau$  the shape parameter. For a prevailing wind of velocity  $U_w$  (in ft/s at 54 ft above the mean sea level) and a fetch  $X$  (ft), the parameters are defined as

$$\begin{aligned} 1 < \gamma < 7 & \quad (\text{average} = 3.3) . \\ \tau = 0.07 & \quad \text{for } \omega < \omega_0 \quad (\text{considered fixed}). \\ \tau = 0.09 & \quad \text{for } \omega > \omega_0 \quad (\text{considered fixed}). \\ \alpha = 0.076 & \quad (X_0)^{-0.22} \quad (\alpha = 0.0081 \text{ when } X \text{ is unknown}). \\ \omega = 2\pi & \quad (g/U_w)(X_0)^{-0.33} \quad (\text{frequency in rad/s}) \\ X_0 = gX/U_w^2 & \end{aligned}$$

Ochi and Hubble (1976) developed a six parameter spectral model which may be used to represent the low frequency (swell) and high frequency (sea)

components of ocean waves. This is written as follows

$$G(\omega) = 0.25 \sum_{j=1}^2 \frac{[0.25(\omega_{0j})^4(4\lambda_j+1)]^{\lambda_j}}{\Gamma(\lambda_j)} \frac{H_{sj}^2}{\omega^{(4\lambda_j+1)}} \cdot \exp[-0.25(4\lambda_j+1)(\omega_{0j}/\omega)^4] \quad (3.29)$$

where  $H_{sj}$ ,  $\omega_{0j}$  and  $\lambda_j$  are the significant wave height, the spectral peak frequency and the spectral shape factor for the lower and higher frequency components when  $j$  equals to 1 and 2 respectively. The model is an algebraic summation of two three-parameter spectra with different spectral peak frequencies and is expressed in terms of significant wave height, spectral peak frequency and spectral shape factor. As shown in equation (3.29), this model may be reduced to the single peaked P-M spectrum by setting the spectral shape parameters to 0 and 1.

Huang et. al. (1981) proposed the Wallops spectral model derived from theoretical analysis and laboratory wave data. Unlike the P-M, Bretshneider and JONSWAP models, the Wallops spectrum is independent of local wind conditions. It is instead related to the significant wave field slope, which is a measure of nonlinearity of the waves in the field, and the spectral peak frequency. The spectral bandwidth of the Wallops spectrum is variable and depends on the nonlinearity of the wave field.

The Wallops spectrum may therefore be used to represent the state of the ocean surface under varying conditions including developing, fully-developed and decaying seas. The Wallops spectrum is written as

$$G(\omega) = \frac{\beta g^2}{\omega^m \omega^{(5-m)}} \exp[-0.25m(\omega/\omega_0)^{-4}] \quad (3.30)$$

Where  $\beta$  and  $m$  are functions of the significant wave field slope,  $\xi$ , and are defined as

$$\xi = (\eta_{rms})^2/L_0 \quad (3.31)$$

where  $L_0$  is the wavelength at the spectral peak,

$$m = \left\lceil \frac{\log(\pi\xi\sqrt{2})^2}{\log(2)} \right\rceil \quad (3.32)$$

and

$$\beta = \frac{(2\pi\xi)^2 m^{0.25(m-1)}}{4^{0.25(m-5)}} \cdot \frac{1}{\Gamma[0.25(m-1)]} \quad (3.33)$$

The similarity between the P-M, JONSWAP and Wallops spectral models is made evident when the significant wave field slope parameter,  $\xi$ , of the Wallops spectrum is set at 0.0398 (hence  $m = 5$ ) and the peakedness parameter of the JONSWAP spectrum is set at 1. Under these conditions they both reduce exactly to the P-M spectrum. The similarity between the P-M, JONSWAP and Wallops spectral models exists only when fully developed sea conditions are represented.

Based on the assumption of weak nonlinear interactions, Huang et. al. (1981) suggested that the superposition of two Wallops spectra of different spectral peak frequency and wave field slopes should prove a useful model for the combined representation of low frequency swell together with higher frequency sea.

Additionally, Hinwood, Blackman and Lleonart (1982) proposed a modified version of the Wallops spectrum to take into account the effects of finite water depths and demonstrated its ability to represent intermediate depth ocean waves.

### 3.3. Distribution of Water Surface Elevations.

By assuming that dynamic interactions between each component of the random wave process are weak, it follows that the wave motions tend to be statistically independent. Therefore, under the central limit theorem, the probability distribution of the water surface elevation may be assumed Gaussian. The Gaussian model, which implies a zero-mean value, is given by

$$p(\eta) = \frac{1}{2\pi\sigma_\eta} \exp\left[\frac{-\eta^2}{2\sigma_\eta^2}\right] \quad (3.34)$$

The variance of the water surface elevation,  $\sigma_\eta^2$ , is defined as

$$\sigma_\eta^2 = M_0 = (\eta_{rms})^2 \quad (3.35)$$

where  $M_0$  is the zeroth moment of the frequency spectrum. A general definition of the spectral moments is given by

$$M_n = \int_0^\infty \omega^n G(\omega) d\omega \quad (3.36)$$

The Gaussian distribution of the water surface elevation is, however, only an approximation. It has been theoretically shown by Phillips (1961) and Longuet-Higgins (1963) that the water surface elevation distribution slightly deviates from the Gaussian distribution due to weakly nonlinear interactions. Kinsman (1965) compared the water surface elevation distribution of experimental wave records with the Gaussian and Gram-Charlier distributions. However, it was concluded that, although the Gram-Charlier distribution exhibited better agreement with the experimental data, the Gaussian distribution usefully represented the distribution of water surface elevations.

Huang et. al. (1980) showed that the deviations from the Gaussian distribution, however slight, are proportional to the significant slope of the wave field. They experimentally demonstrated the relationship between the skewness of the water surface elevation distribution and the significant slope of the wave field,  $\xi$ . Furthermore, the authors also demonstrated that under highly non-Gaussian conditions, such as  $\xi = 0.04$ , the water surface elevation distribution may be approximated by a four-term Gram-Charlier expansion.

### 3.4. Distribution of Surface Elevation Maxima.

By assuming that ocean waves are composed of many sinusoidal wave components of random phase and the frequency spectrum of that process is sufficiently narrow, Longuet-Higgins (1952) showed that the probability distribution of the wave amplitudes corresponds to the Rayleigh distribution, defined as follows

$$p(a) = \frac{2a}{(a_{rms})^2} \exp[-(a/a_{rms})^2] \quad (3.37)$$

where the wave amplitude,  $a$ , is defined as one half of the height of a wave crest above the preceding trough, hence  $a = H^*/2$  where  $H^*$  is the crest-to-trough wave height.

Equation (3.37) can be alternatively expressed as

$$p(a) = \frac{a}{M_0} \exp[-a^2/2M_0] \quad (3.38)$$

Where  $M_0$  is the zeroth moment of the frequency spectrum and is equivalent to the mean-square of the water surface elevation. For linear motions, when the individual wave crests are approximately sinusoidal,  $M_0$  may be expressed as

$$M_0 = 0.5 (a_{rms})^2 \quad (3.39)$$

It is therefore only when equation (3.39) is satisfied that equation (3.38) is equivalent to equation (3.37). The theoretical distribution of the wave amplitude for processes with wider spectral bandwidths is more difficult to establish and is discussed in section 3.5.

Cartwright and Longuet-Higgins (1956) considered the water surface elevation maxima,  $\eta_m$ , to be the difference between the wave crest and the mean water level. They adapted the results of work done by Rice (1944, 1945) on electrical noise signals to ocean waves. The resulting theoretical distribution was found to be dependent on a spectral width

parameter,  $\epsilon$ , and the root mean square of the surface elevation,  $\eta_{rms}$ . The distribution is written as

$$p(\eta_m) = (1/\sqrt{2\pi}) \epsilon \exp[-0.5(\eta_m/\epsilon)^2] + \sqrt{1-\epsilon^2} \eta_m \exp(-0.5\eta_m^2) \int_{-\infty}^{\eta_m \sqrt{1-\epsilon^2} / \epsilon} \exp(-0.5 x^2) dx \quad (3.40)$$

and is illustrated in figure 3.2 as a function of the spectral width parameter  $\epsilon$ .

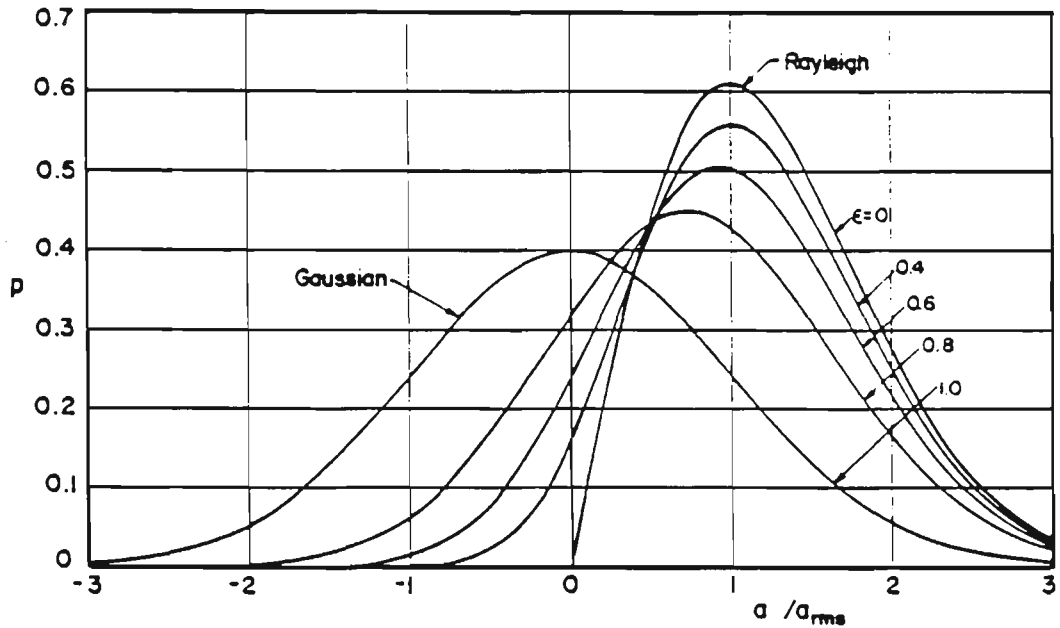


Figure 3.2. Variation of the water surface elevation maxima with the spectral width parameter - After Cartwright and Longuet-Higgins (1956) -

In general,  $\epsilon$  is a measure of the root-mean-square width of the frequency spectrum and may vary between zero and unity. A process is usually considered narrow band when  $\epsilon$  is less than 0.6. The spectral width parameter may be computed from the moments of the spectral density function by

$$\epsilon = \epsilon_s = \sqrt{\frac{M_0 M_4 - M_2^2}{M_0 M_4}} \quad (3.41)$$

For a narrow band process ( $\epsilon = 0$ ), equation (3.32) reduces to the Rayleigh distribution while for a wide band process ( $\epsilon = 1$ ), equation (3.32) reduces to the Gaussian distribution. A narrow band process is one in which all maxima (peaks) are above the mean water level (positive) and all minima (troughs) are below the mean water level (negative). This is illustrated in Figure 3.3.

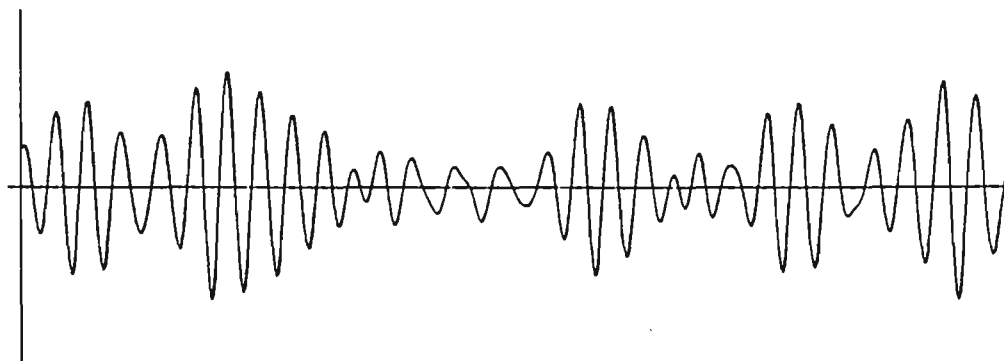


Figure 3.3. Narrow band random process.

In a wide band process, peaks appear below and troughs above the mean water level. For water waves this may be realised when ripples are superimposed on a low frequency swell.

The spectral width parameter may alternatively be obtained by simply counting the number of positive and negative maxima in a record. Here  $\epsilon$  is defined as

$$\epsilon = \epsilon_c = [1 - (N_z/N_c)^2]^{0.5} \quad (3.42)$$

Where  $N_z$  is the number of zero-up-crossings in the record and  $N_c$  is the total number of crests in the record.

Longuet-Higgins (1957) proposed an alternative definition of the spectral bandwidth,  $\nu$ , as follows

$$\nu = (\mu_2/M_2)^{0.5} \quad (3.43)$$

where  $\mu_2$  is the second central moment of the energy spectrum and is defined as

$$\mu_2 = \int_0^{\infty} (\omega - \bar{\omega})^2 G(\omega) d\omega \quad (3.44)$$

with the mean frequency  $\omega$  defined as

$$\omega = M_1/M_0 \quad (3.45)$$

Goda (1974) questioned the usefulness of the spectral width parameter,  $\epsilon$ , and subsequently proposed a spectral peakedness parameter which describes the sharpness of the spectral peak(s). The spectral peakedness parameter,  $Q_p$ , is defined as

$$Q_p = \frac{2}{M_0^2} \int_0^{\infty} \omega G^2(\omega) d\omega \quad (3.46)$$

$Q_p$  becomes unity for white noise and takes larger values for spectra with sharp peaks.

Longuet-Higgins (1952) studied the expected extreme value of the maxima  $E(\eta_{m.\max})$ , and the most probable extreme value of  $\eta_{m.\max}$ , denoted as  $p(\eta_{m.\max})$ , for narrow banded processes. Cartwright and Longuet-Higgins (1956) proposed a solution for the expected extreme value of the maxima for all values of  $\epsilon$  ranging between 0 and 1. This solution was based on the assumption that the number of maxima,  $N$ , in the record is large.

Ochi (1972) proposed a simplified solution for  $E(\eta_{m.\max})$  for values of  $\epsilon$  ranging between 0 and 0.9 which is written as

$$E(\eta_{m.\max}) = \sqrt{2M_0 \ln \left[ \frac{\sqrt{1-\epsilon^2} \cdot 2N}{(1 + \sqrt{1-\epsilon^2})\lambda} \right]} \quad \text{for } \epsilon < 0.9 \quad (3.47)$$

where  $N$  is the number of maxima in the sample and  $\lambda$  is a small probability level such that  $E(\eta_{m.\max})$  will be exceeded. Equation (3.47) is valid for  $\lambda < 0.01$ .

When  $\epsilon = 0$ , equation (3.47) reduces to the original solution proposed by Longuet-Higgins (1952) for a narrow band process:

$$E(\eta_{m.\max}) = \sqrt{2M_0 \ln(N/\lambda)} \quad \text{for } \epsilon = 0 \quad (3.48)$$

Ochi (1972) also compared the expected extreme value for a narrow band process with the corresponding most probable extreme value. It was found that, for large values of the number of maxima,  $N$ , the probability of exceeding  $p(\eta_{m.\max})$  was quite high.

The solution for the most probable extreme value,  $p(\eta_{m.\max})$ , for  $0 < \epsilon < 0.9$  is given by

$$p(\eta_{m.\max}) = \sqrt{2M_0 \ln\left(\frac{\sqrt{1-\epsilon^2} 2N}{(1 + \sqrt{1-\epsilon^2})}\right)} \quad \text{for } \epsilon < 0.9 \quad (3.49)$$

which reduces to the solution given by Longuet-Higgins (1952) for large values of  $N$  when  $\epsilon = 0$  :

$$p(\eta_{m.\max}) = \sqrt{2M_0 \ln(N)} \quad \text{for } \epsilon = 0 \quad (3.50)$$

Ochi (1972) showed that when  $E(\eta_{m.\max})$  and  $p(\eta_{m.\max})$  are expressed in terms of time, the functions are no longer dependent on the spectral width parameter but on the expected rate of zero-up-crossings,  $f_z$ , defined as

$$f_z = (M_2/M_0)^{0.5} \quad (3.51)$$

The expected extreme value of the highest maxima as a function of time is given by

$$E(\eta_{m.\max}) = [2M_0 \ln(T_s f_z / 2\pi\lambda)]^{0.5} \quad \text{for } \lambda < 0.01 \quad (3.52)$$

where  $T_s$  is the length of the record in seconds.

And the most probable extreme value the highest maxima as a function of time is given by

$$p(\eta_{m.\max}) = [2M_0 \ln(T_s f_z / 2\pi)]^{0.5} \quad \text{for } \lambda < 0.01 \quad (3.53)$$

### 3.5. Distribution of Wave Heights.

There are two essential definitions of wave heights. The zero-up-cross wave height,  $H$ , is defined as the difference in level between the maxima and minima located between two adjacent points where the surface elevation crosses the line of mean water level upward. The crest-to-trough wave height  $H^*$  however, is defined as the difference in level between any positive or negative maxima (crest) and the subsequent minima (trough). These are illustrated in Figure 3.4.

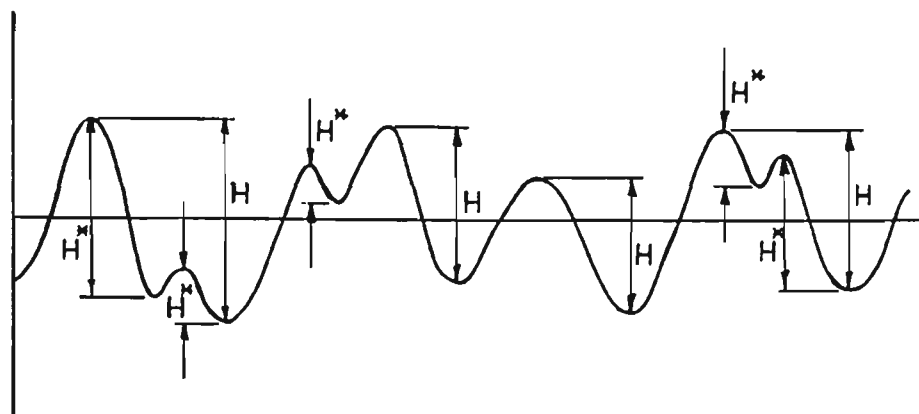


Figure 3.4. Definition of wave heights.

When considering zero-up-cross waves, any existing negative peaks or positive troughs are, by definition, not taken into account. This leads to the process being treated as purely narrow band regardless of the actual width of the spectrum. Consequently, the statistical distribution of zero-up-cross wave heights is independent of the spectral width parameter and, in general, follows the Rayleigh distribution. Since the zero-up-cross wave height of individual waves represent twice the amplitude  $a$ , equation (3.37) can be written in terms of  $H$  as

$$p(H) = \frac{2H}{(H_{rms})^2} \exp[-(H/H_{rms})^2] \quad (3.54)$$

When a random process has a narrow frequency spectrum, negative maxima and positive minima are unlikely to exist. Consequently, for narrow band processes ( $\epsilon \ll 1$ ), the statistical distribution of crest-to-trough wave heights follows the Rayleigh distribution (eqn. 3.54).

Alternatively, the distribution can be expressed in terms of the zeroth spectral moment,  $M_0$ , as

$$p(H^*) = \frac{H^*}{4M_0} \exp \left[ \frac{-H^{*2}}{8M_0} \right] \quad (3.55)$$

where

$$M_0 = (H^*_{rms})^2/8 \quad (3.56)$$

As previously mentioned in section 3.4., equations (3.54) and (3.55) are equivalent only when equation (3.39) is true.

Since by definition,  $H^* = 2a$ , the distribution of crest-to-trough wave heights is equivalent to the distribution of the wave amplitude described by equation (3.37).

Cartwright and Longuet-Higgins (1956) suggested that the general expression for the distribution of crest-to-trough wave heights would depend on other parameters besides the spectral width parameter. Furthermore, they also demonstrated that, in general, observed crest-to-trough wave height distributions departed from the Rayleigh distribution as the width of the energy density spectrum increased. The authors also noted that discrepancies between observed crest-to-trough wave height distribution and the Rayleigh distribution were small for data with a spectral width parameter less than 0.5.

Forristall (1978) observed that the distribution of crest-to-trough wave heights of hurricane generated waves in the Gulf of Mexico was better described by a Weibull distribution rather than the Rayleigh distribution of equation (3.38). Longuet-Higgins (1980) rejected Forristall's conclusions claiming that some confusion had been introduced as to the definition of the Rayleigh distribution. Longuet-Higgins (1980) emphasised that equation (3.38) is one of many possible Rayleigh distributions and was not the form of equation (3.37) as originally proposed by Longuet-Higgins (1952). The author subsequently showed that the distribution of the experimental data used by Forristall could be equally well described by the

Rayleigh distribution of equation (3.37) provided that the root-mean-square amplitude is estimated from the original true record and not from the frequency spectrum. He concluded that Forristall's two-parameter Weibull distribution did not offer any obvious advantages over the originally proposed Rayleigh distribution.

### 3.6. Significant Wave Height.

The concept of the significant wave height was introduced by Sverdrup and Munk (1947) and is defined as the average height of the highest one third of all waves. The significant wave height,  $H_s$  or  $H_{1/3}$ , may be computed from a time record by using the following equation,

$$H_{1/3} = (3/N) \sum_{i=1}^{N/3} H_i^* \quad (3.57)$$

where  $N$  is the number of crest-to-trough waves heights,  $H_i^*$ , in the record ranked from highest to lowest.

Since the above method of computation is time consuming, Tucker (1963) formulated an approximation for determining the significant wave height from a wave record which is given as

$$H_s = \sqrt{2} \cdot C_1 (a_c + a_t) \quad (3.58)$$

where  $a_c$  is the height of the highest crest above the mean water level,  $a_t$  the depth of the lowest trough below the mean water level, and  $C_1$  is defined as

$$C_1 = (\ln N_z)^{-0.5} [1 + 0.289 (\ln N_z)^{-1} - 0.247 (\ln N_z)^{-2}]^{-1} \quad (3.59)$$

where  $N_z$  is the total number of zero-up-crossing cycles.

Alternatively, the significant wave height may be estimated from the frequency spectrum. Since by definition the significant wave height is the average of the highest one-third waves, then

$$P(H_0) = 2/3 = 1 - \exp[-(H_0/H_{rms})^2] \quad (3.60)$$

or

$$H_0 = 1.0481 H_{rms} \quad (3.61)$$

which states that all values of  $H$  which are greater than  $H_0$  are in the highest one-third range. The significant wave height is determined by defining the centroid of the area under the density function for which  $H \geq H_0$  as follows

$$H_{1/3} = \frac{\int_{H_0}^{\infty} H p(H) dH}{\int_{H_0}^{\infty} p(H) dH} \quad (3.62)$$

For spectra with small spectral width parameters, where the wave height distribution follows the Raleigh distribution, the significant wave height is given by

$$H_{1/3} = 1.416 H_{rms} \quad (3.63)$$

or by substituting for  $H_{rms}$  (eqn. 3.39) where  $H_{rms} = 2 a_{rms}$ ,

$$H_{1/3} = 4.005 \sqrt{M_0} \quad (3.64)$$

With the assumption that all crest-to-trough wave heights are twice the wave amplitude from the still water level, Cartwright and Longuet-Higgins (1956) studied the variation of  $H_{1/3}$ ,  $H_{ave}$  and  $H_{1/10}$  relative to the spectral width parameter  $\epsilon$ . The result of their approximation was graphically derived by Silvester (1974) from the paper by Cartwright and Longuet-Higgins (1956) and is shown in figure 3.5 where  $\sqrt{E} = 2M_0$ .

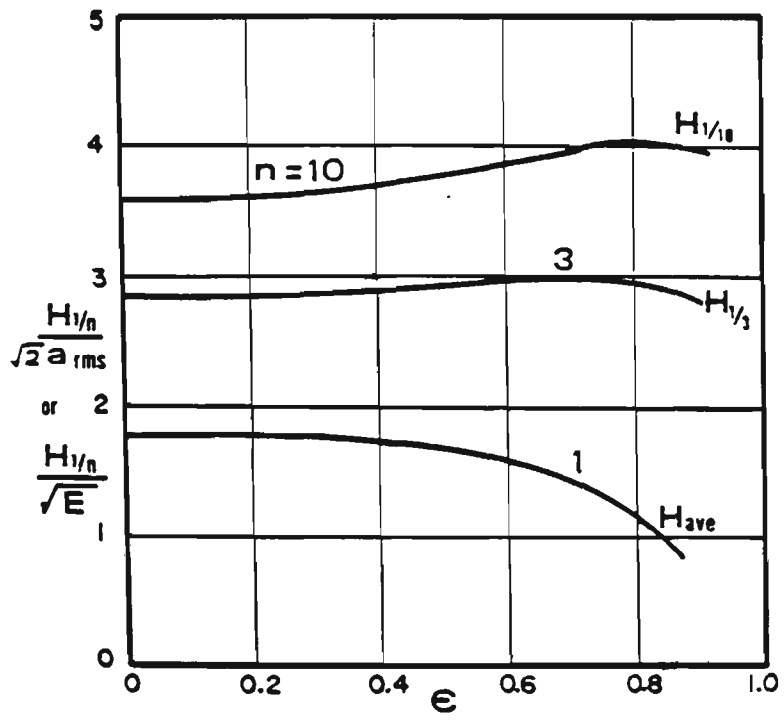


Figure 3.4. Variation of  $H_{1/n} / 2M_0$   
 - After Cartwright and Longuet-Higgins (1956) -

## 4. WAVE GENERATION EQUIPMENT AND SOFTWARE

### 4.1. Review of Wave Generators.

Early laboratory wave generators were restricted to reproducing periodic waves of regular form, usually by means of complicated mechanical linkages driven by electric motors. Later wave generators mostly employed electro-hydraulic servo-mechanisms to generate both regular and random waves. In reviewing the development of wave generators, the most pertinent factors relating to their design and performance will be examined and discussed.

Biesel and Suquet (1951) were among the first to attempt to classify laboratory wave generators. Besides specifying a number of important design criteria, they identified seven main types of wave generating mechanisms which are illustrated in figure 4.1

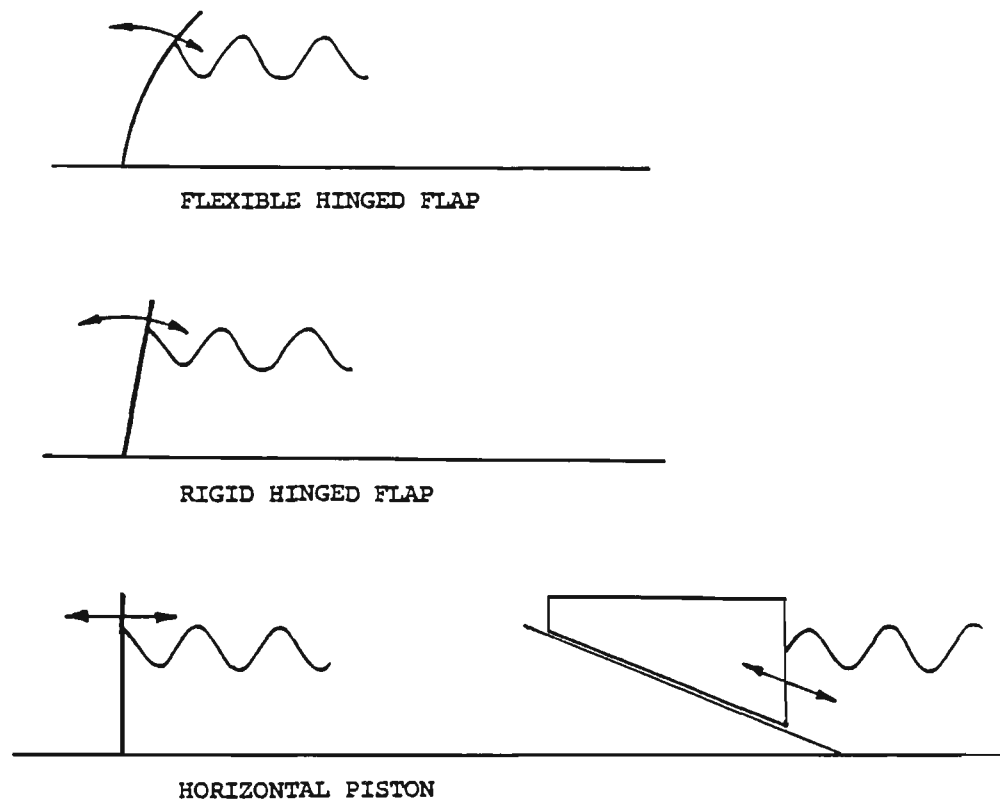


Figure 4.1. Some types of wave makers.

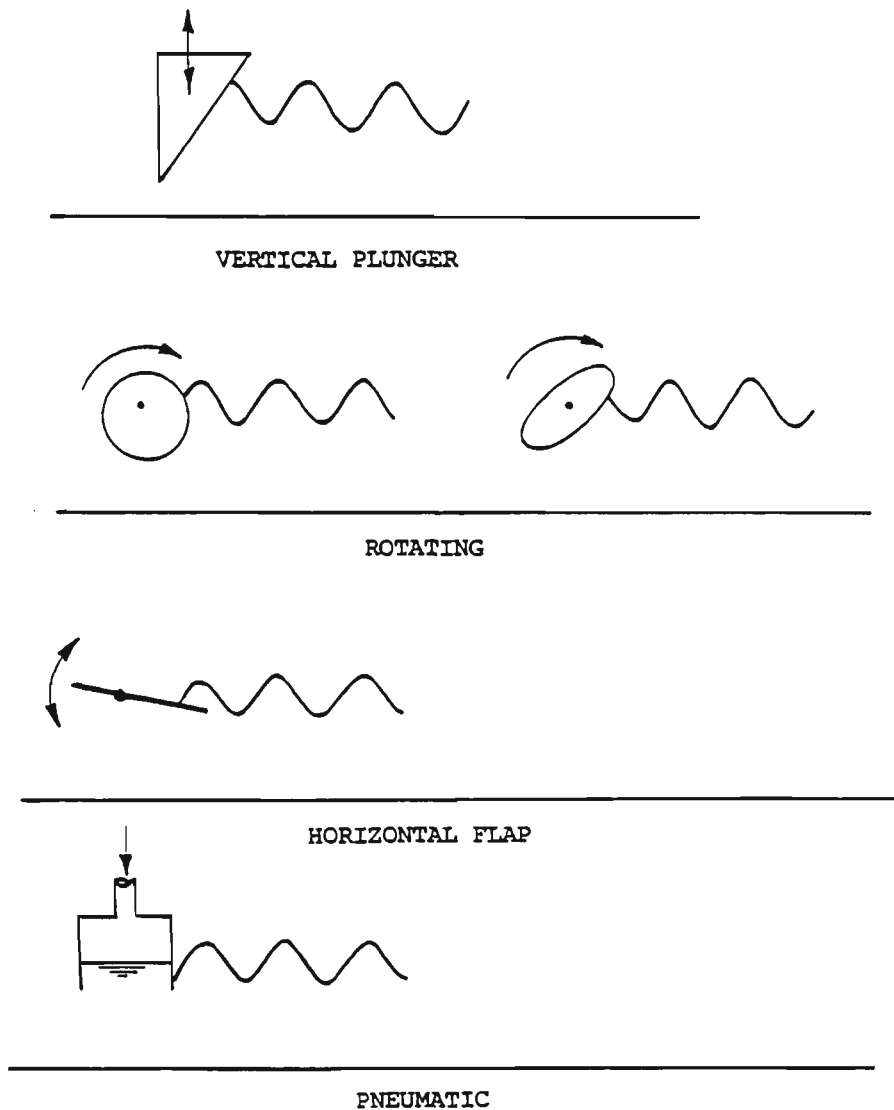


Figure 4.1.(cont'd) Some types of wave makers.

Biesel and Suquet also published calculated frequency response functions relating the wave maker stroke to wave height for some popular types of wave makers. Their calculations were based on the wave maker theory of Havelock (1929) and apply only to the generation of small amplitude waves.

Ursell, Dean and Yu (1960) attempted to experimentally verify the linear wave maker theory for a piston type wave maker. Their experiments were conducted in a 100 ft. long wave channel equipped with an electro-hydraulic wave maker and a plane impermeable wave energy absorber with a gradient of 1:15. The amplitude reflection coefficient was found to usually be less

than 10%. The results obtained from experiments conducted with small wave steepnesses ( $0.002 < H/L < 0.03$ ) showed good agreement with the theoretical wave maker theory based on classical hydrodynamic assumptions. Experiments conducted for larger wave steepnesses ( $0.045 < H/L < 0.048$ ) showed some departure from the theory. This was attributed to finite amplitude effects. Although wave reflection was accounted for in the analysis, the authors indicated that the errors could be reduced and the analysis simplified if wave absorption was more efficient. There have since been many studies of wave generator behaviour, mostly aimed at determining the ratio of wave maker stroke to wave height for regular waves.

A vertical triangular plunger type wave maker was analysed by Huyn (1967). This study was also based on Biesel and Suquet's approach. The wave maker frequency response function was analysed in terms of plunger stroke to wave height and the total hydrodynamic force on the triangular shaped wedge was studied.

Gilbert, Thompson and Brewer (1971) published design curves for both regular and random wave generators. Their analysis was based on the same approach as that of Biesel and Suquet but they presented dimensionless values of wave maker stroke and force over a wide range of a dimensionless parameter directly dependent on the wave period rather than wave length. Hinged flap, piston and wedge type wave makers were analysed.

Wang (1973) also studied plunger type wave makers. Theoretical wave height prediction functions in terms of wave maker stroke and frequency were presented. In addition, the variation of the wave maker stroke to wave height ratio and the wave maker force components with respect to the geometric parameters of the plunger were presented. It was also noted that the wave elevation at far field is not sensitive to the geometrical details of the plunger other than its width, depth of submergence and area.

Keating and Webber (1977) conducted experiments similar to those of Ursell et. al. on a piston type wave maker and evaluated the effects of leakage of water around the sides of the wave maker. They concluded that errors in wave height prediction due to leakage were less than 1%.

Multer and Galvin (1967) observed that when relatively long waves of finite amplitude were generated by a sinusoidally moving wave maker, the resulting waves broke down into a primary and one or more secondary waves. These travel at different velocities and the resulting wave profile exhibited the presence of secondary waves depending on the distance from the wave generating surface. Madsen (1971) studied this phenomenon and showed that the free second harmonic wave may be substantially reduced by giving the wave maker a non-sinusoidal motion that consists of a first and second harmonic. Hansen, Schiolden and Svendsen (1975) studied the concept of a second order Stokes wave and the superimposed second harmonic. They demonstrated that the wave pattern exhibits an apparent variation in mean water level along the tank length as well as the presence of free second harmonics. This meander of the mean water level has an amplitude equal to that of the free second harmonic component. This was experimentally verified and the authors subsequently proposed a non-sinusoidal wave maker motion to generate sinusoidal waves.

More germane to this study is the application of wave makers to the physical modelling of real sea conditions as opposed to the generation of regular waves. This section reviews various methods of simulating random wave trains in the laboratory.

Borgman (1969) identified two basic methods for the numerical simulation of a zero-mean Gaussian random process of specified spectral density for ocean waves: (1) by linear filtration, and (2) by wave superposition. The linear filtration technique employs a pure Gaussian random signal (white noise) modified by a linear filter designed according to specific spectral density characteristics. In the wave superposition technique a finite number of sinusoidal or cosinusoidal functions, governed by a specific spectral density function, are generated with randomly assigned phases. In the latter method, the target spectral density function is used to compute the amplitude of the sinusoids and the random phase angles are required to be uniformly distributed between 0 and  $2\pi$ .

Goda (1970) successfully used the wave superposition method for the numerical simulation of irregular waves with a digital computer. The effects of the number of component waves,  $N$ , on the distribution of the

time signal was studied and a compromise between the computation time and the realisation of the Gaussian distribution was arrived at. Goda subsequently recommended that, although 200 or more component waves would achieve better results, 50 and 60 component waves, for single and double peak spectra respectively, would be sufficient for the time signal to have a Gaussian distribution.

Fryer, Gilbert and Wilkie (1973) described the design of a wave spectrum synthesizer in which white noise was generated digitally in a shift register and passed through a digital filter to obtain the desired shape of the frequency spectrum.

Webber and Christian (1974) employed the digital filtration method for the physical modelling of wave spectra. Their design of a piston type wave maker were based on the design curves formulated by Gilbert, Thompson and Brewer (1971). The wave generator used for the experiment consisted of a closed loop electro-hydraulic positioning servomechanism. The command signal was generated by exciting a specially designed digital filter with computer generated white noise. The filter was not only designed according to the target spectral density function but also to accommodate the frequency response characteristics of the wave generation system. The frequency response function was considered as two separate stages; the command signal-to-wave maker motion and wave maker motion-to-wave motion. The frequency response function of the second stage was obtained directly from the theoretical function published by Biesel and Suquet (1951). Reasonable experimental results were obtained but the authors acknowledged room for improvement in the control system.

Funke (1974), similarly to Fryer, Gilbert and Wilkie (1973), used a binary feedback shift register to generate a pseudo-random signal which was then numerically convolved with a digital filter to produce a synthetic wave record. Experiments, aimed at reproducing the JONSWAP spectrum, were carried out on an electro-hydraulic wave generator which, through two separate linkages, allowed the wave maker to operate in three modes; piston, hinged flap or a combination of both. Reproduction of the target spectrum in the tank was achieved by initially compensating for the system frequency response characteristics and subsequently optimised by means of a difference algorithm based on the target spectrum and the measured

spectral estimates. Their results show good agreement between the target and realised spectra.

Hudspeth and Borgman (1979) used an inverse FFT algorithm together with a digital computer to generate random time sequences from a spectral density function without the use of spectral feedback compensation. Their experiments were conducted in an unusually large wave tank (104 metre long) equipped with a hinged flap type electro-hydraulic wave generator. The experiments, aimed at reproducing the Bretshneider - Pierson - Moskowitz and the Scott spectra, show good agreement between measured spectral estimates and target spectra. Furthermore, the good agreement between the measured and theoretical water surface elevation distribution was attributed to the longer duration of simulation made possible by the stacked FFT algorithm.

There have been many more reports of various experiments aimed at physically simulating spectral models of ocean waves in the laboratory. Most, although using different means of command signal synthesis and wave generation have been achieved with a reasonable degree of accuracy.

Model sea conditions may be reproduced by generating a scaled actual ocean surface elevation record via a wave maker. Although feasible, this method may not be practical since actual wave records are not readily available. Moreover, the record may only apply to a specific location and set of conditions. As demonstrated by many observers, ocean waves may be represented by a zero mean Gaussian stochastic process with a specified spectral density function (or frequency spectrum). Simulation may be achieved by generating a synthesised signal, derived from a target spectral density function, while retaining the original statistical characteristics of the process. This may be achieved by the Inverse Fast Fourier Transform where a large number of frequency components can be used in the simulation by specifying closely spaced frequency components. The resulting time signal,  $y(t)$ , is defined as

$$y(t) = \sum_{n=1}^N A_n \cos(2\pi f_n t + \delta_n) \quad (4.1)$$

in which

$$A_n = 2 \sqrt{G(f_n) \Delta f_n} \quad (4.2)$$

where  $n = 1, 2, \dots, N$ .

$N$  = number of component waves.

$f$  = frequency in Hz.

$\delta$  = uniformly distributed phase between 0 and  $2\pi$ .

$G(f)$  = spectral density function.

Of practical importance in physical wave modelling is the need to consider and accommodate the effects of the system response characteristics on the command signal.

Electro-hydraulic wave generators have proved to be most popular due to their ability to follow command signals with good accuracy and reliability. Despite the significance of higher order effects, linear theory is generally used to determine system response characteristics. Surprisingly, few random wave generation facilities employ spectral feedback compensation techniques to improve the reproduction of spectral models. The effects of duration and the number of component waves on the distribution of the water surface elevation are of major importance on the performance of a random wave generators facility and should be given due consideration.

This study is principally concerned with the steady-state behaviour of ocean waves. The random processes under consideration will therefore be treated as stationary and ergodic.

#### 4.2. Design of Wave Generator.

In this section, the important concepts related to the design of the wave generator are considered. The principal components of the system, as shown in figure 4.2, form the basis for discussion of the design. The wave generator comprises a concrete flume, a wave maker, two wave absorbers and a wave probe. The flume is 21 metre long, 1 metre wide and 1.2 metre deep. In order to allow visual observation of wave motions, one side of the wave flume is fitted with four laminated glass panel each 2 metre long by 1 metre high.

A plunger-type mechanical wave maker, powered by an electro-hydraulic servomechanism, was mounted near one end of the flume and the wave absorbers, used to minimise reflections, were located at each end of the flume. A moveable wave probe for monitoring the water surface elevation was mounted on horizontal rails fixed to the top of the flume. A micro-computer was programmed to control the motion of the wave maker as well as to run software developed for recording and analysing experimental data.

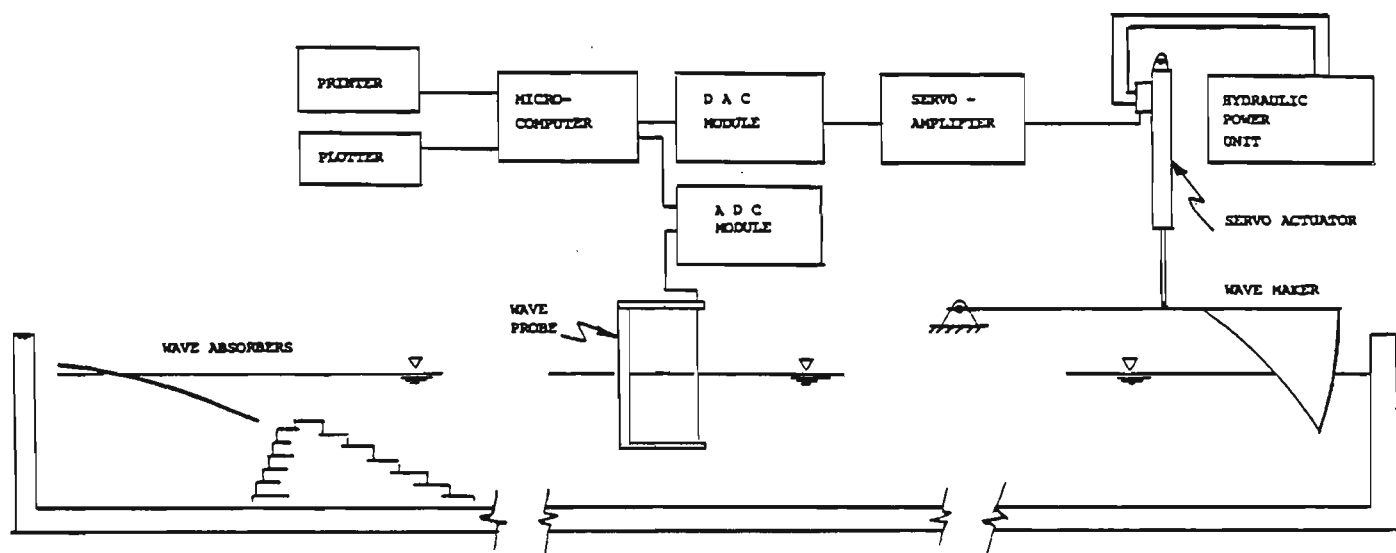


Figure 4.2. Schematic of wave generation facility.

In considering the design of computer controlled wave generators, good engineering practice dictates that a number of important criteria be met. Paramount among these is that the design of the wave maker must be characterised by high rigidity and low inertia in order to effect good system response and reduce errors in controlling motion. It is essential to restrict the number of mechanical linkages to a minimum while the mechanism driving the wave maker should be free of frictional effects, slack, dead bands etc. As noted in the literature, attention needs to be paid to reducing leakage between the wave plunger and the flume walls since it has been shown to be a source of errors when generating waves.

A satisfactory variety of sea conditions may be simulated in the laboratory if the maximum wave height were about 50 cm and the frequency range for random waves between 0 and 3 Hertz. Using this data, the maximum stroke,

velocity and force requirements were calculated from the design curves published by Gilbert et. al. (1971). An electro-hydraulic servo-mechanism coupled directly to a wave plunger appeared an attractive proposition. However, analysis showed that a servo-valve capable of handling high flow rates was needed to drive the wave plunger at the required velocities. A system designed around this concept was rejected since the power requirements were excessive and the cost was prohibitive. The wave generator was instead designed with a servo-valve rated for lower flow rates and a simple mechanical lever system was introduced to drive the wave plunger at the required velocities. This proved to be an effective and economic alternative.

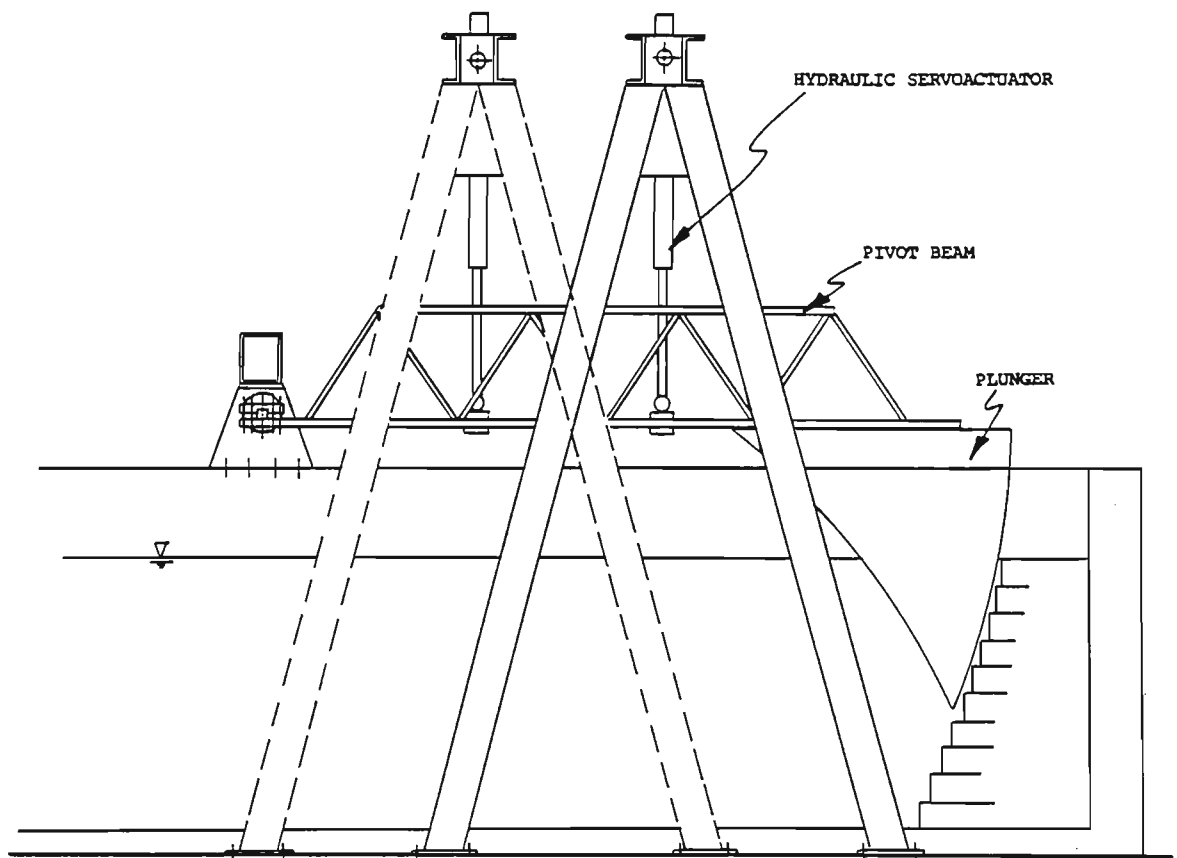


Figure 4.3. Wave maker support arrangement.

The wave maker consists of a wedge shaped plunger connected to a beam hinged about a horizontal axis across the wave tank. The wave maker is activated by means of an electro-hydraulic servo-actuator hinged to a steel frame whose position may be varied so that the mechanical advantage of the plunger may be altered as shown in figure 4.3.

The shape of the plunger was designed to approximate the effect produced by a triangular wedge moving vertically or normal to the still water surface. The rear of the plunger forms an arc of 2.5 metres radius from the pivot beam hinge to minimize the generation of disturbances behind the wave maker. The front or generating surface of the plunger forms an arc of 2.56 metres radius about point 'o' as shown in figure 4.4. This profile was designed to minimize the differences in the horizontal displacement of each horizontal plane when the wave maker is activated, as shown in figure 4.4 where

$$x_i - x_j \approx 0 \quad \begin{array}{l} \text{for } i = 2,3,4 \dots n \\ \text{and } j = 1,2,3 \dots n-1 \end{array} \quad (4.3)$$

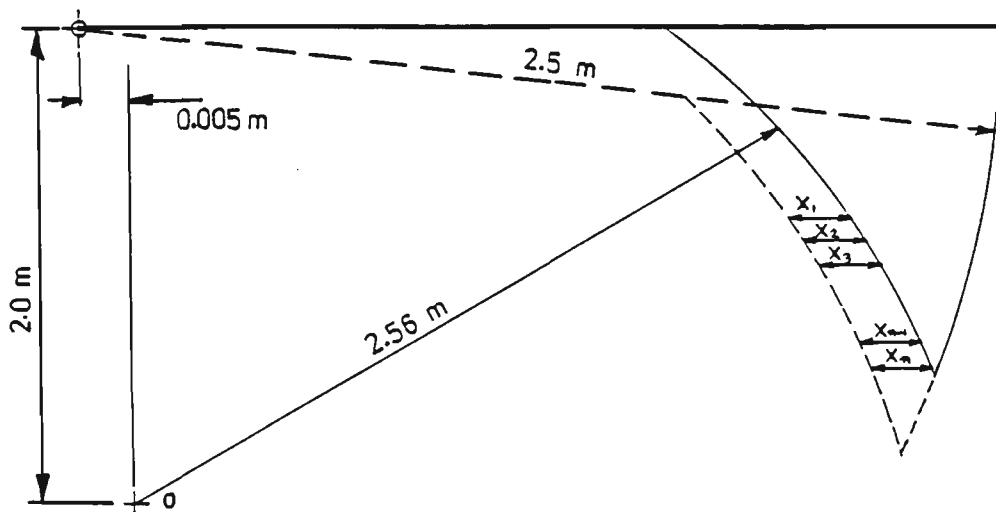


Figure 4.4. Wave maker dimensions.

The mathematical formulation of the generating surface profile is given, in detail, in appendix B.

The plunger is a welded aluminium structure designed with a high stiffness to mass ratio in order to optimize the response characteristics of the system and to minimize positioning errors arising from structural deflections when operating under dynamic conditions. The plunger, made of aluminium sheeting, comprises five vertical ribs each 3 mm thick with the rear and front surfaces each 5 mm thick as shown in figure 4.5.

Supports made of aluminium angle sections were fixed to the plunger to provide a firm and rigid base for attachment to the pivot beam.

The plunger was made to fit in the wave tank with a clearance of 5 mm on each side.

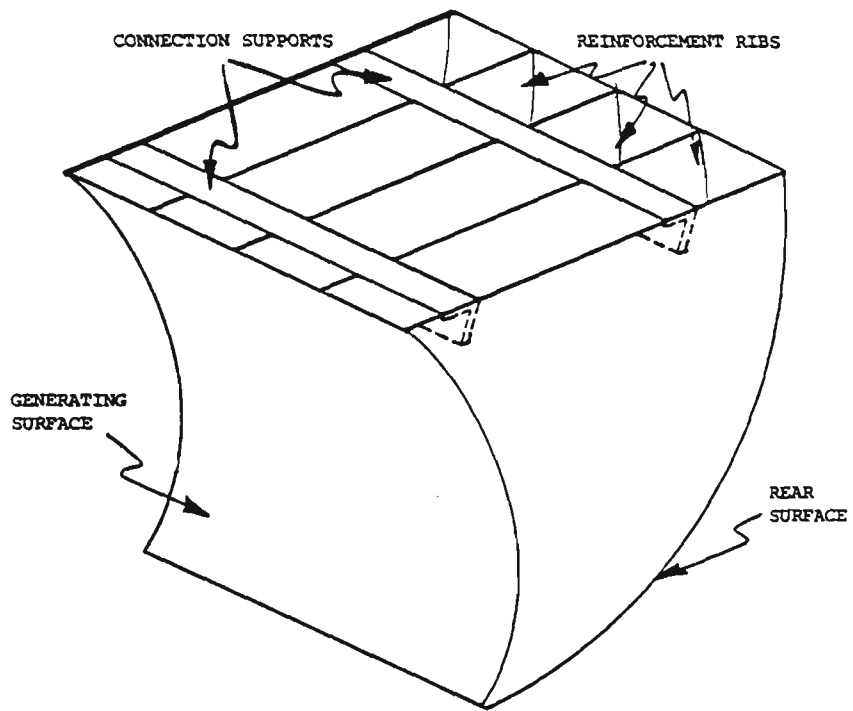


Figure 4.5. Wave maker plunger.

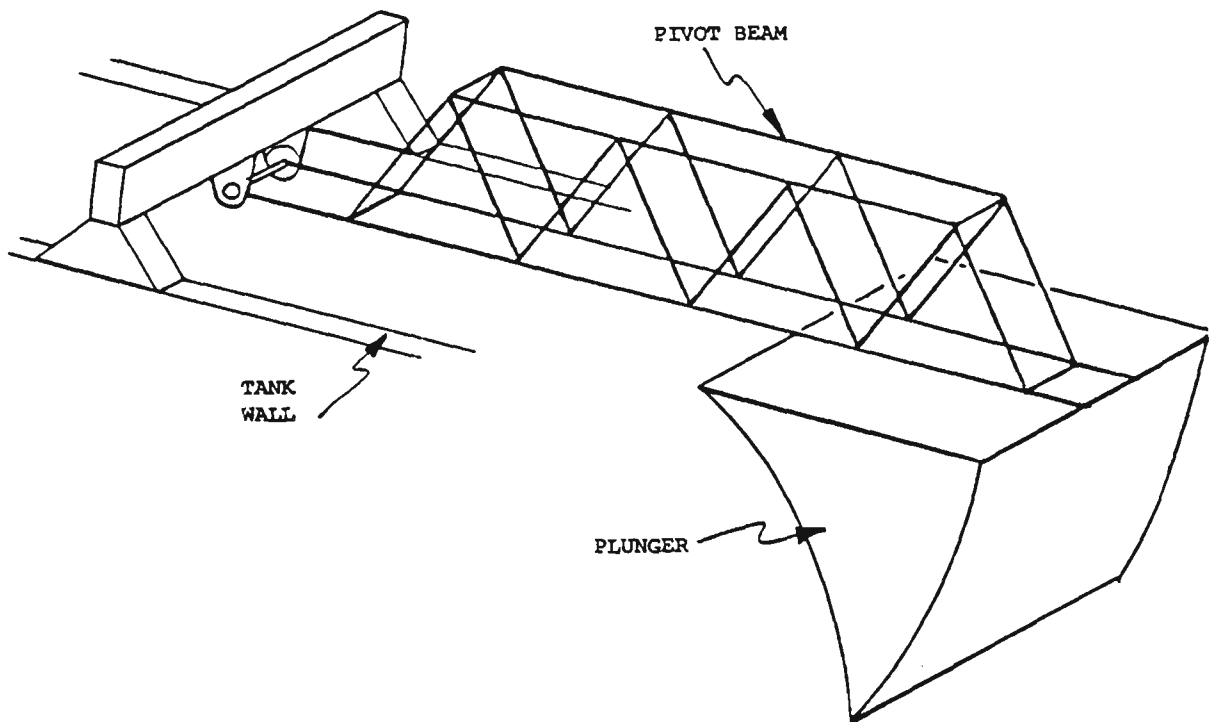


Figure 4.6. Wave maker arrangement.

The pivot beam is a welded steel truss made of rolled hollow steel (RHS) sections of the following dimensions: 76 mm x 38 mm x 3.2 mm and 25 mm x 25 mm x 2.0 mm. The pivot beam was also designed to achieve high rigidity and low inertia and was firmly bolted to a shaft supported by two pairs of tapered roller bearings to eliminate slack. The bearings and bearing housing consist of a hub arrangement similar to that used in road vehicles. The bearing housings were rigidly bolted to an RHS section of 250 mm x 150 mm x 10 mm straddling the wave tank as shown in Figure 4.6. The support beam was rigidly bolted to the 180 mm wide reinforced concrete tank walls with epoxy acrylate adhesive anchors.

The hydraulic servo-actuator hangs vertically from a steel frame to which it was hinged via a pair of tapered roller bearings. The support structure forms an 'A' frame consisting of four steel columns and two channel sections mounted horizontally as shown in Figure 4.7.

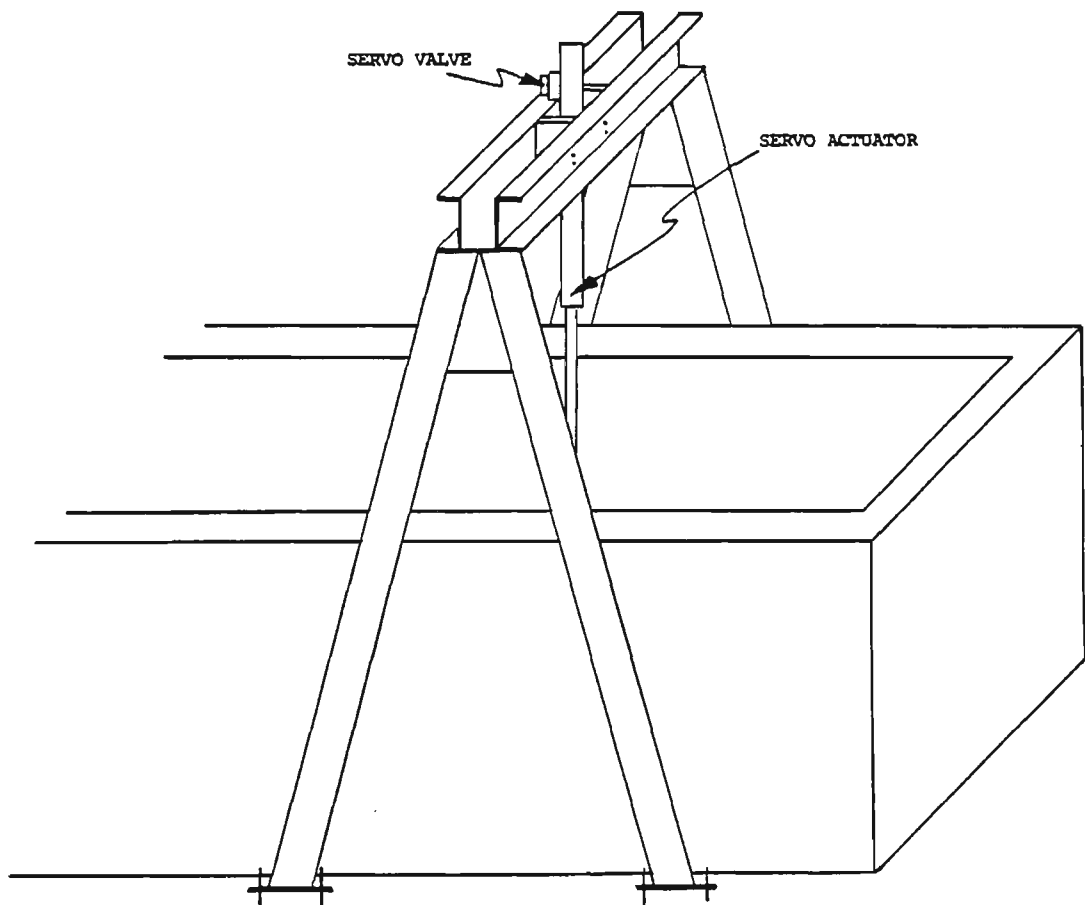


Figure 4.7. Wave generator arrangement

The 'A' frame straddles the wave tank and was firmly bolted to the concrete floor. The mechanical advantage of the wave maker may be changed if desired by moving the 'A' frame to various positions along the wave tank. The rod end of the hydraulic actuator and the pivot beam were coupled by a pair of tapered roller bearings and bearing housing arrangement rigidly fixed to the pivot beam.

Estimates of the resonant frequencies and corresponding mode shapes of the pivot beam and the 'A' frame were obtained by finite element analysis using the McNeal-Schwendler Corporation's FEA computer software package, MSC-PAL.

A computer based finite element model of the 'A' frame was created and the structure was analysed by simulating a dynamic load applied at the hydraulic actuator connecting point as shown in figure 4.8.

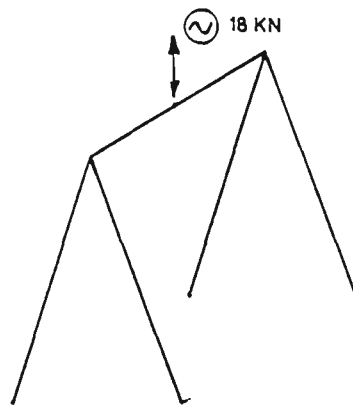


Figure 4.8. Force excitation of A frame model for Finite Element Analysis.

The load was made to vary sinusoidally at an amplitude of 18 kN and at frequencies ranging between 0 and 300 Hz. The results of the analysis, displayed in figure 4.9, indicate the presence of a resonant frequency at approximately 190 Hz. The ordinate scale represents displacement in decibels. Since it is expected that the wave maker will not operate at frequencies higher than 4 Hz, the 190 Hz resonance is well above the recommended separation limit of 10 decades between the maximum operating frequency and the first natural frequency.

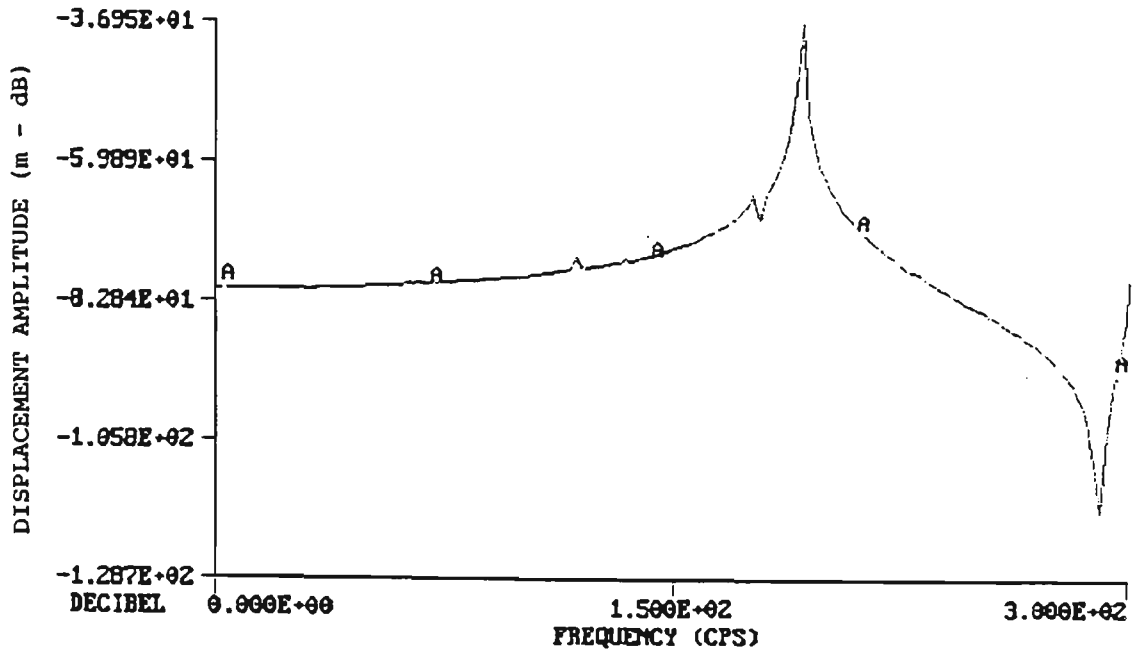


Figure 4.9(a). Deflection response of A frame.

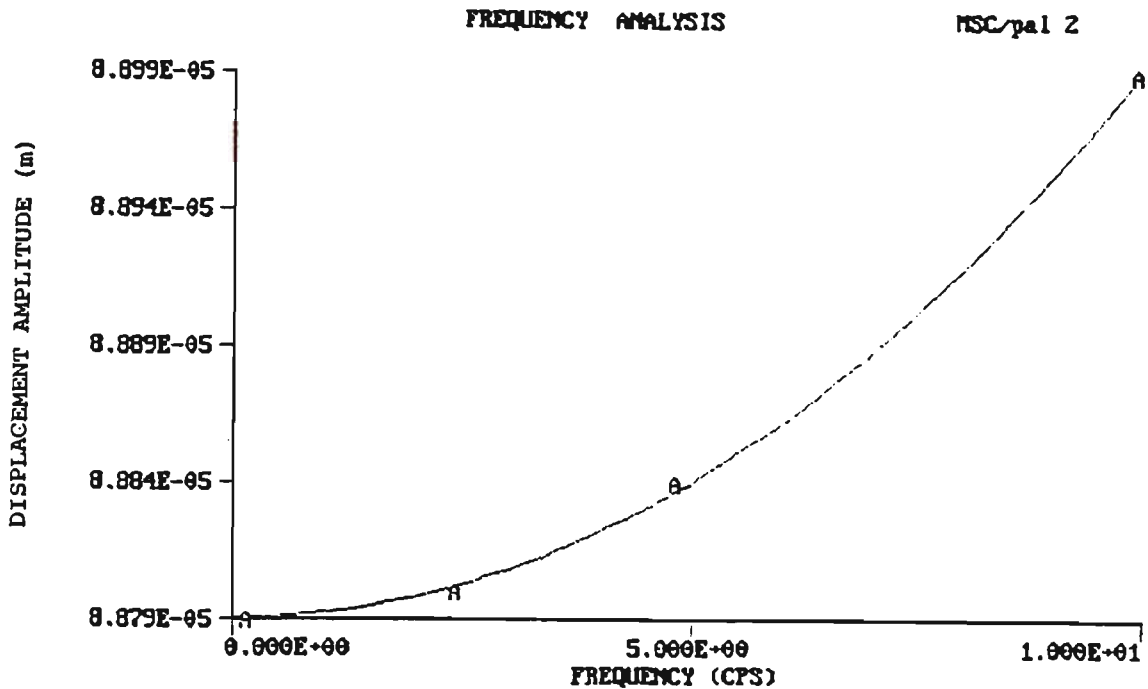


Figure 4.9(b). Deflection response of A frame.

Figure 4.9(a) shows the deflection response of the A frame to excitation frequencies between 0 and 300 Hz, while Figure 4.9(b) gives a more accurate representation of the expected deflections of the 'A' frame at the actuator connecting point for dynamic loads with frequencies ranging between 0 and 10 Hz. The ordinate scale is in metres (linear). As can be seen from figures 4.9(a) and (b), the expected vertical deflections of the 'A' frame

predicted by finite element analysis are negligible and thus demonstrate adequate stiffness of the structure.

Similarly to the 'A' frame, a finite element model of the pivot beam was created and analysed. A vertical dynamic displacement function was programmed to act at point 'i' along the beam as shown in figure 4.10. The displacement function was defined as sinusoidal with an amplitude of 0.1 metres and frequencies ranging between 0 and 200 Hz.

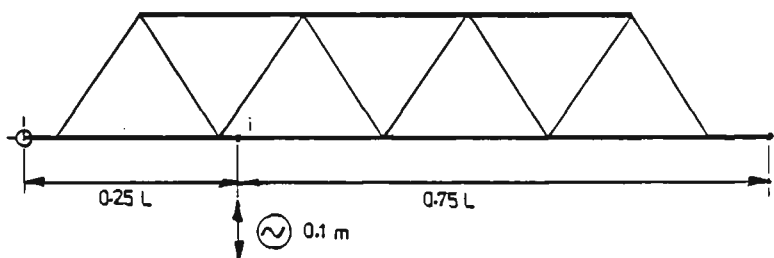


Figure 4.10. Displacement excitation of pivot beam for FEA.

The resulting amplitude of motion at point 'o' is plotted against frequency in figure 4.11(a) and indicates the existence of a resonant frequency at approximately 86 Hz. The ordinate scale represents displacement in decibels. It must be noted that, because of the mechanical advantage, the expected displacement amplitude at point 'o' for a d.c. input is 0.4 metres or -7.96 dB.

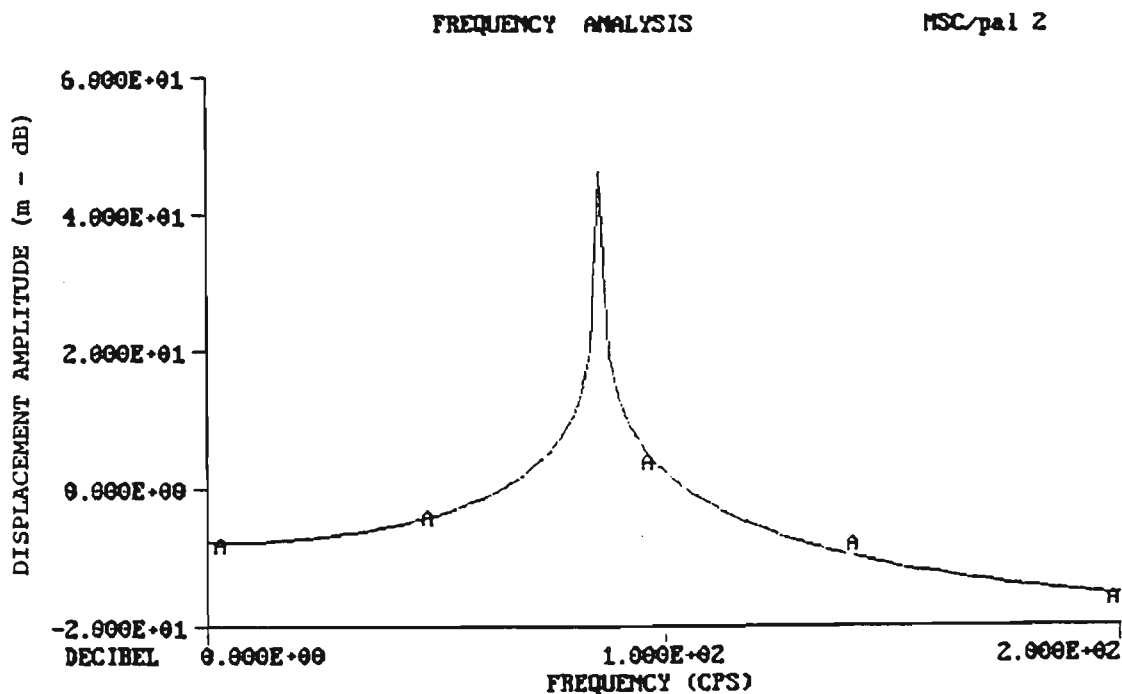


Figure 4.11(a). Displacement response of pivot beam.

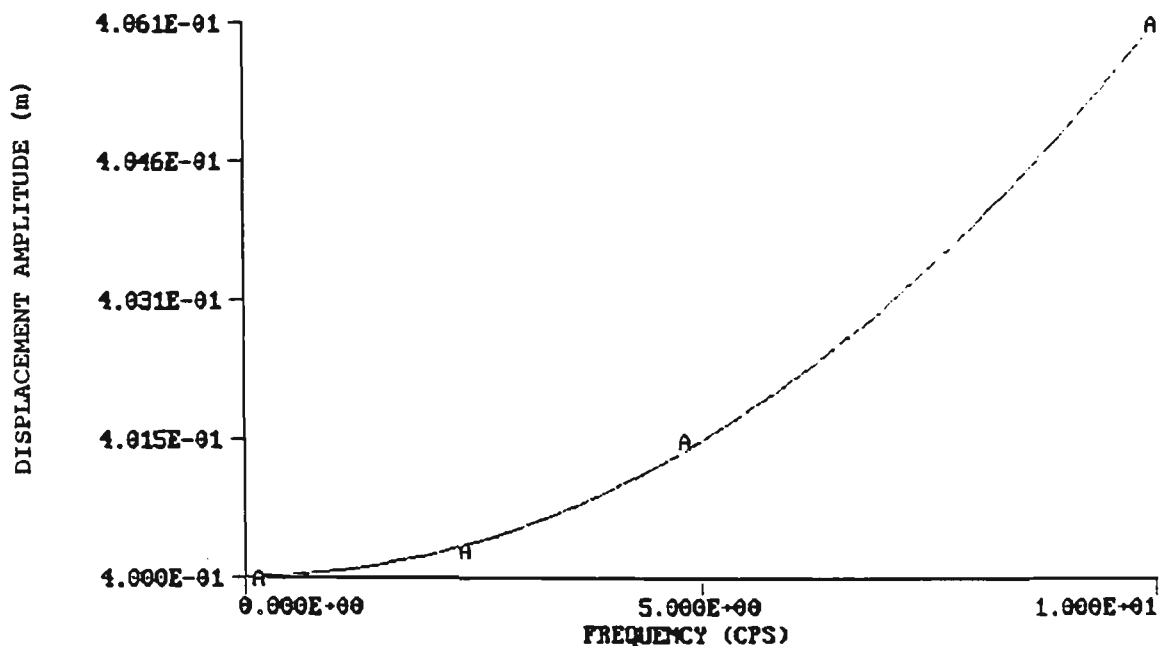


Figure 4.11(b). Displacement response of pivot beam.

Figure 4.11.(b) shows the frequency response at point 'o' for frequencies of 10 Hz or less with the ordinate scale in metres (linear). The expected dynamic displacement error,  $e_d$ , at 4 Hz, may be evaluated as follows:

$$\begin{aligned}
 [e_d]_{4 \text{ Hz}} &= [(0.401011 - 0.4)/0.4] \\
 &= 0.0025 \\
 &= 0.25 \%
 \end{aligned}
 \tag{4.4}$$

These results verify that the structural properties of the pivot beam are satisfactory under the worse expected dynamic loading conditions.

The stresses in both the 'A' frame and the pivot beam were also computed by finite element analysis and were found to be well within acceptable limits.

The electro-hydraulic system consists of a MOOG series M852 servo-actuator which incorporates a hydraulic actuator, servo-valve and position transducer. The hydraulic actuator, of 50.8 mm bore and 600 mm stroke, was fitted with a 76 series flow control servo-valve capable of handling a flow rate of up to 40 litres per minute when extending and 35 litres per minute when retracting. The contactless 'GYTL' magnetostrictive displacement transducer was mounted inside the hydraulic actuator and was connected to a

displacement signal conditioner which provided an analogue voltage output directly proportional to the position of the actuator. A schematic diagram of the electro-hydraulic wave generator system is shown in Figure 4.12.

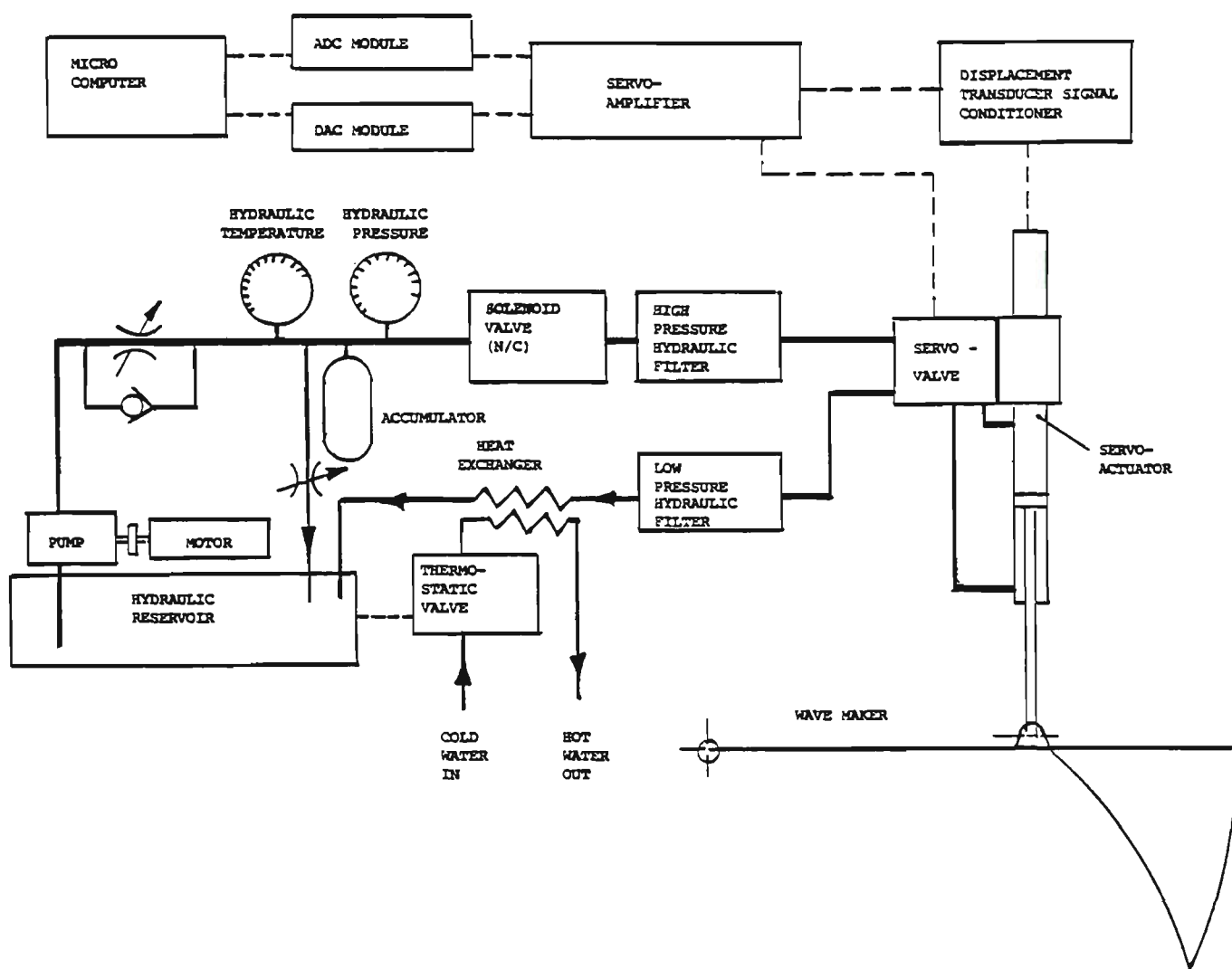


Figure 4.12. Electro-hydraulic wave generator system.

The servo-actuator operates as a closed loop feedback positioning system controlled by a MOOG servo-amplifier type M121-823. The servo-amplifier incorporates means of adjusting the loop gain, bias (zero offset) and span of the command signal. A dither signal generator is also included in the servo-amplifier to help overcome actuator stiction (static friction) during operation at low frequencies. Listed below are some characteristics of the servo-actuator system.

Maximum actuator velocity : 330 mm/sec.  
Maximum output force : 18 kN @ 11.8 Mpa.  
Expected static position accuracy :  $\pm 0.5$  mm

Displacement transducer specifications:

Resolution : 0.01% FS  
Nonlinearity : 0.05% FS  
Repeatability : 0.01% FS  
Operating temperature range : 0 - 50 °C

Hydraulic power was provided by a VICKERS hydraulic power unit supplying hydraulic oil at 40 litres per minute and 14 MPa. The unit consists of a 15 kW three-phase electric motor, a variable displacement pressure compensated piston pump and a 6.3 litre nitrogen charged accumulator. The unit also includes a water cooled heat exchanger, controlled by a thermostatic valve, with a cooling capacity of 18 kW. The hydraulic power unit was connected to the servo-actuator with 25.4 mm teflon-lined flexible hoses. The hydraulic oil was filtered by a MOOG 15-micron high pressure filter model HP020 located in the high pressure line and a MOOG 3-micron low pressure filter model LPA0250 located in the return line.

#### 4.3. Wave Probe.

Water surface elevation was measured by means of a capacitance type wave probe consisting of a perspex frame supporting a single strand of enamel coated copper wire 0.24 mm in diameter. The wave probe operates on the principle that the capacitance between the insulated copper wire and the body of water varies linearly with depth of submergence. The wave probe formed the active component of an AC capacitance bridge which was excited by a SANGAMO carrier amplifier card type 911001-85. The amplifier card also included a demodulator, signal amplifier and low-pass filter to provide a stable analogue voltage signal proportional to water surface elevation. Additionally, the amplifier permitted the selection of a wide range of sensitivities as well as zero balancing adjustments.

Further specifications of the SANGAMO carrier amplifier card are listed below:

Oscillator output: :  $5 V_{RMS}$  sine wave @ 5 kHz  
 Selectable sensitivity range : 0.5 mV/V to 750 mV/V  
 Range of gain settings : Coarse : 500:1  
 : Fine : 3:1  
 Maximum output range : + 5 V  
 Output ripple :  $< 5 mV_{pp}$   
 Low-pass filter : 3rd order, 500 Hz cutoff frequency  
 Nonlinearity :  $< 0.02 \% FS$   
 Operating temperature range : 0 - 70 °C

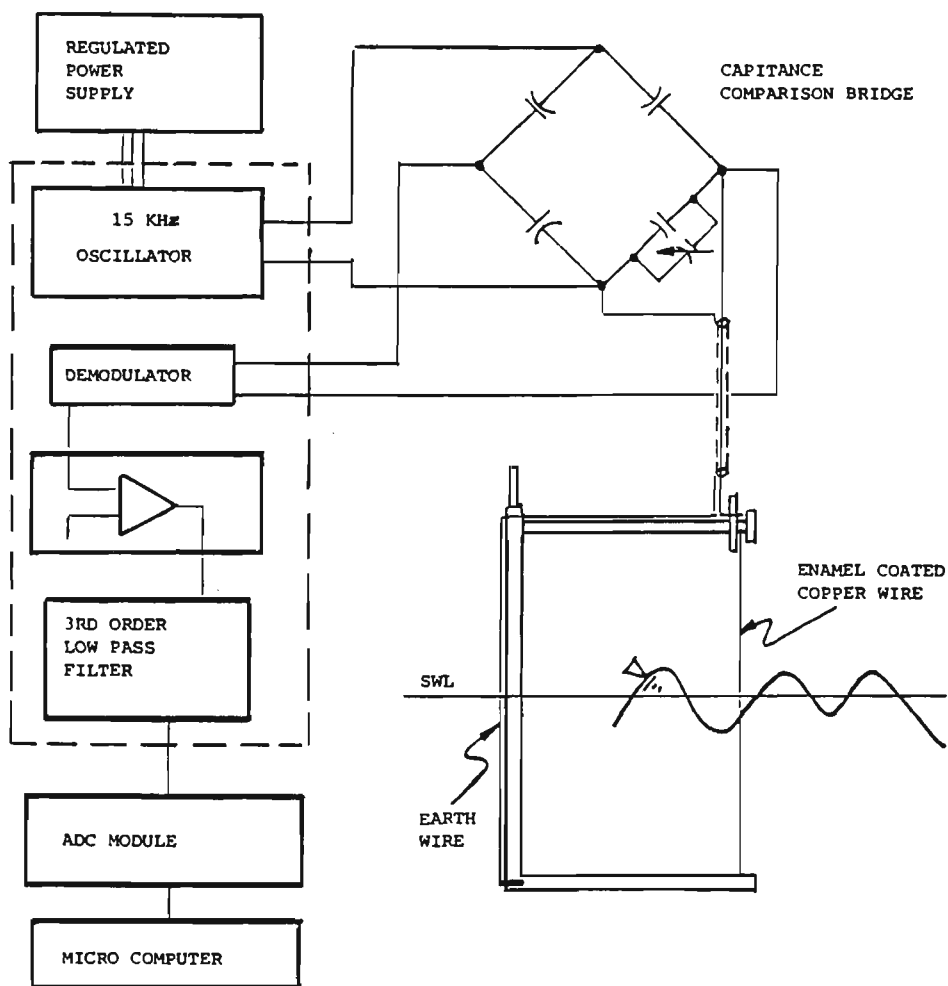


Figure 4.13. Wave probe.

A schematic diagram of the wave probe is displayed in Figure 4.13. The vertical arm of the perspex frame supporting the copper wire was streamlined to minimize fluid disturbances near the copper wire. The diameter of the enamel coated copper wire was kept to a practical minimum in order to lessen errors due to meniscus. The wave probe was mounted on a carriage which may be wheeled along the length of the tank manually or by an electric motor and pulley arrangement. The carriage consists of an aluminium frame fitted with a screw thread to which the wave probe was secured. The screw thread was used to move the probe vertically for static calibration purposes.

#### 4.4. Wave Absorbers.

In order to reduce reflection of generated waves, a wave energy absorber was located at the non-generating end of the wave tank. The wave absorber consists of two parts: a pile of clay bricks arranged to form an average slope of 18 degrees from the horizontal and a parabolic shaped perforated aluminium sheet lined with eight (8) layers of nylon knitted shade cloth. The wave absorber is shown in figure 4.14.

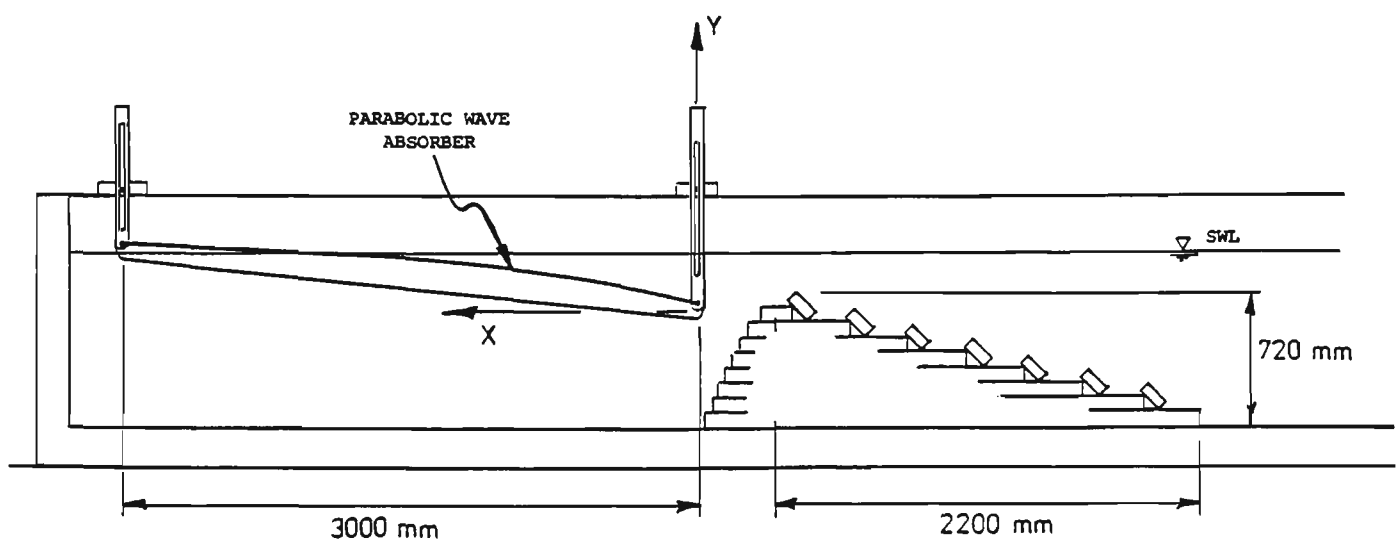


Figure 4.14. Wave energy absorber.

The parabolic wave absorber was made from 2 mm thick aluminium sheet perforated in a regular pattern with 15 mm diameter holes. In addition, rows of louvre perforations 10 mm high were pressed in the aluminium sheet in a random pattern. The width of the louvre perforations varies between

35 and 240 mm. The pattern of the wave absorber surface is shown in Figure 4.15.

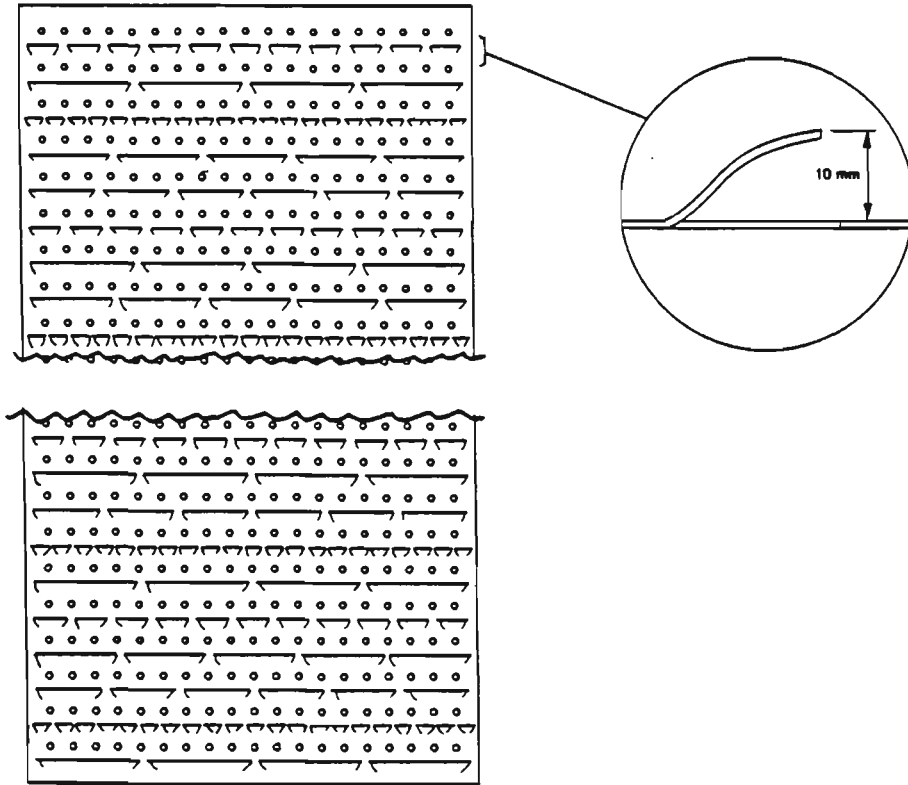


Figure 4.15. Parabolic wave absorber pattern.

The parabolic wave absorber was based on the work of Svendsen and Jonsson (1976) who demonstrated that a parabolic profile yields efficient dissipation of wave energy. Due to the relatively short length of the wave tank, the parabolic wave absorber was kept as short as practically possible and was shaped according to the following equation

$$y = 0.3x - 0.03x^2 \quad \text{for } 0 < x < 3 \text{ metres} \quad (4.5)$$

where  $x$  and  $y$  are defined in figure 4.14.

The slope, depth and position of the parabolic wave absorber were made adjustable to allow optimisation of energy absorbed.

The wave tank was fitted with a second energy absorber aimed at reducing disturbances behind the wave maker. This absorber was made entirely of clay bricks and occupied most of the space between the plunger and the back

wall of the wave tank (see figure 4.3). The narrow passages formed by the wave absorber reduces spurious fluid disturbances created by the wave maker.

#### 4.5. Control System.

The wave generator control system was based on a PC-AT 286 micro-computer system with 640 kilobyte Random Access Memory (RAM) equipped with a 40 Mb hard disk for mass data storage and a 80287 floating point math co-processor. The micro-computer was interfaced with a DATA TRANSLATION data acquisition card type DT2806 hosting an analogue-to-digital (A/D) conversion module type DTX311 and a digital-to-analogue (D/A) conversion module type DTX328. Analogue to digital conversions are accomplished by a 12 bit monolithic converter capable of up to 20,000 conversions per second. The DTX311 provides eight differential input channels and is configured to receive bipolar signals ranging between -5 and +5 volts. Specifications of the DTX311 are listed below:

Resolution	: $\pm 0.5$ bit
Nonlinearity	: $< 0.5$ LSB (Least Significant Bit)
Operating temperature range	: 0 - 70 °C

The DTX328 digital-to-analogue conversion module is capable of 3300 conversions per second and provides four bipolar output channels each ranging between -5 and +5 volts. Specifications of the DTX328 are listed below:

Resolution	: $\pm 0.5$ bit
Nonlinearity	: $< 0.5$ LSB (least Significant Bit)
Operating temperature range	: 0 - 55 °C

The digital position command signal, generated from the microcomputer, is converted into an analogue voltage by the D/A conversion module and transmitted to the servo-amplifier which in turn controls the position of the servo-actuator. The water surface elevation record measured by the wave probe is captured by the A/D conversion module and stored in the micro-computer's Random Access Memory for future processing.

#### 4.6. Software Development.

Computer software developed for the control and management of the wave generation facility was based on the commercial software package DAOS (Data Acquisition Operating System) released by Laboratory Software Associates. DAOS is a high level operating environment and language implemented using the C programming language and was designed to specifically meet the needs of laboratory automation applications. DAOS comprises modules such as REALTIME for data generation and acquisition, PLOT which contains graphical display functions, CHEF for interactive screen and menu management, and FFT for forward and inverse Fast Fourier Transformations. Preliminary assessment of this software package revealed its suitability for this project.

A number of program libraries, each containing a collection of subroutines or macros, were designed and developed specifically for the management of the wave generation facility. The function of each of these libraries are briefly outlined below and later described in greater detail.

- WPCAL - for static calibration of wave probes.
  
- WGRECO - for determination of wave reflection characteristics of the wave tank and also used to generate wave trains consisting of up to three regular wave components.
  
- WGTFSS - for determination of the frequency response characteristics of any part of the system.
  
- WGENSP - for generation of random waves based on spectral models.
  
- WGSTAT - for statistical analysis of measured wave data from random wave experiments.

##### 4.6.1. Wave Probe Calibration - WPCAL.

Although the variation of the wave probe calibration constant with time was found to be small, it is desirable to calibrate the wave probe

before and after each experiment. In order to facilitate frequent static calibration of wave probes, the collection of subroutines contained in this program library were developed.

Calibration was simply performed by manually adjusting the height of the wave probe relative to the still water level and capturing the sampled output signal in the computer memory via the A/D conversion module. After a specified number of calibration points were recorded a line of best fit using the least squares method was computed. The gradient of the line of best fit was stored on the system hard disk to be latter retrieved as required. The data points may then be printed and or plotted on screen or plotter.

#### 4.6.2. Reflection Evaluation and Regular Wave Generation - WGRECO.

This collection of subroutines enables generation of a command signal composed of the sum of up to three sinusoidal waveforms. The frequency, amplitude and phase of each sinusoidal component may be specified independently. The subroutines also allows the water surface elevation signal, measured by a wave probe, to be recorded.

The reflection characteristics of the wave energy absorber are determined by generating a regular wave train while recording the water surface elevation from a wave probe moving along the tank. The resulting water surface elevation record will be that of the envelope of the standing wave or partial clapotis resulting from the addition of the incident and reflected waves trains. The incident wave steepness and the reflection coefficient are then determined graphically.

The menu driven programs allows the user to set the frequency and amplitude of the command signal while the wave length is automatically computed by iteration, using the relationship between wavelength and frequency given by equation (2.65).

The command signal is then transmitted to the wave maker through the digital-to-analogue conversion module. The water surface elevation time history, as monitored by the moving wave probe, is captured through the

analogue-to-digital conversion module and displayed graphically. If required, any portion of the measured water surface elevation record may be expanded graphically on screen. A line cursor moving vertically on the computer screen allows the operator to graphically determine the height of the nodes and antinodes from which the amplitude reflection coefficient may be calculated using equation (2.132). Alternatively, the nodes and antinodes heights may be measured from a paper plot of the water surface elevation time history.

#### 4.6.3. Random Wave Generation - WGENSP

As mentioned in section 4.1, real sea conditions may be simulated in the laboratory by reproducing an actual time history of the ocean surface elevation. Alternatively, random waves may be simulated by using a synthesised command signal derived from a mathematical spectral model. This wave generation system uses of the Inverse Digital Fast Fourier Transform to generate random signals from a specified spectral model, scaled according to Froude's similarity law.

A simple spectral feedback compensation technique was employed to accurately achieve the desired wave conditions in the wave tank. The control method is illustrated in figure 4.16.

Signal compensation was performed in the frequency domain by comparing the measured spectral estimate with the target spectrum and correcting for differences over the complete frequency range. The compensated spectrum was corrected for discrepancies after each completed control loop until acceptable agreement between the target spectrum and the measured spectral estimates was achieved. A specific spectral model may be continuously reproduced as an aperiodic signal by allocating a new set of random values, uniformly distributed between 0 and  $2\pi$ , to the phase component of the compensated spectrum at the beginning of each control loop. Both the acquired surface elevation data and its corresponding spectral estimates may be saved on hard disk to be later available for statistical analysis. Spectral estimates of the water surface elevation are computed by means of the Fast Fourier Transform after the captured time data are initially passed through a rectangular window to suppress

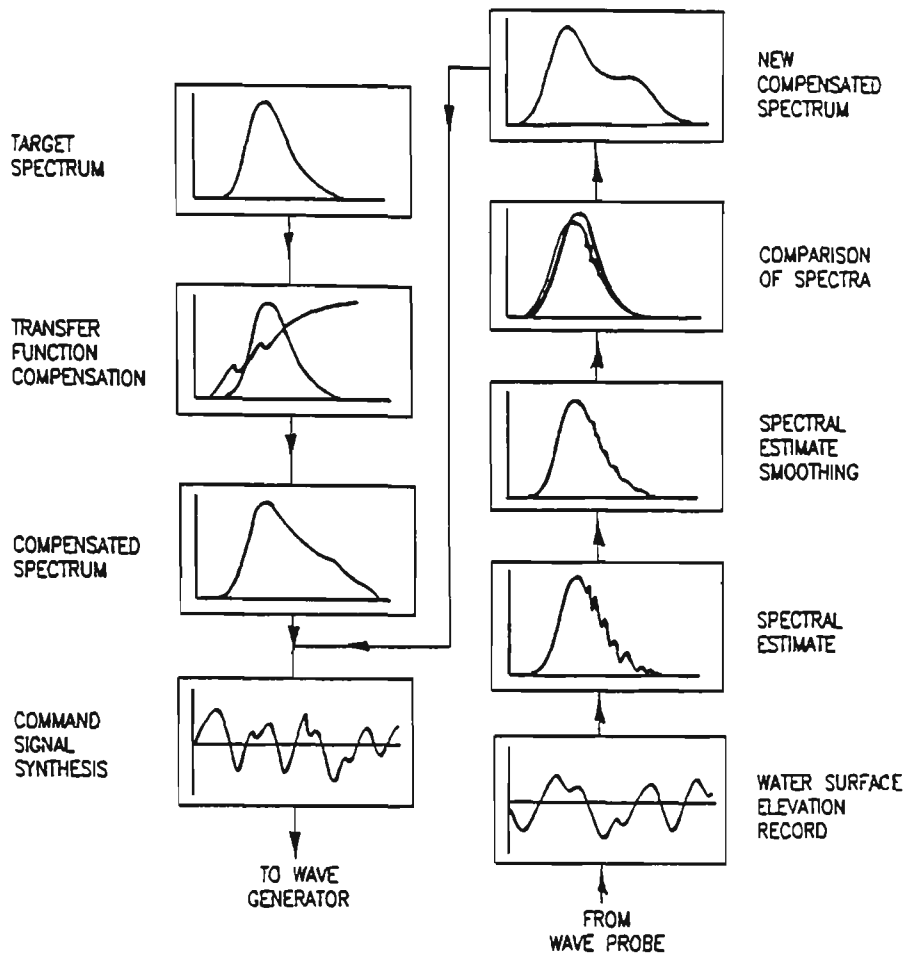


Figure 4.16. Illustration of control method for random wave generation.

side-lobe leakage. Aliasing was eliminated by ensuring that the sampling frequency exceeds the Nyquist frequency. The spectral estimate may be smoothed by means of a moving spectral window whose weighting function and bandwidth are selectable. A compromise must be made when selecting the spectral window bandwidth in order to retain a reasonable frequency resolution while reducing the variance of each spectral estimate.

For control purposes only, better results are obtained if the measured spectral estimates are smoothed before being compared with the target spectrum. The final spectral estimates from an experiment can be obtained from the average the raw spectral estimates stored at each loop of operation or, if desired, the raw spectral estimates may be smoothed by the moving spectral window method before being averaged thus combining both spectral smoothing methods mentioned in section 3.1.

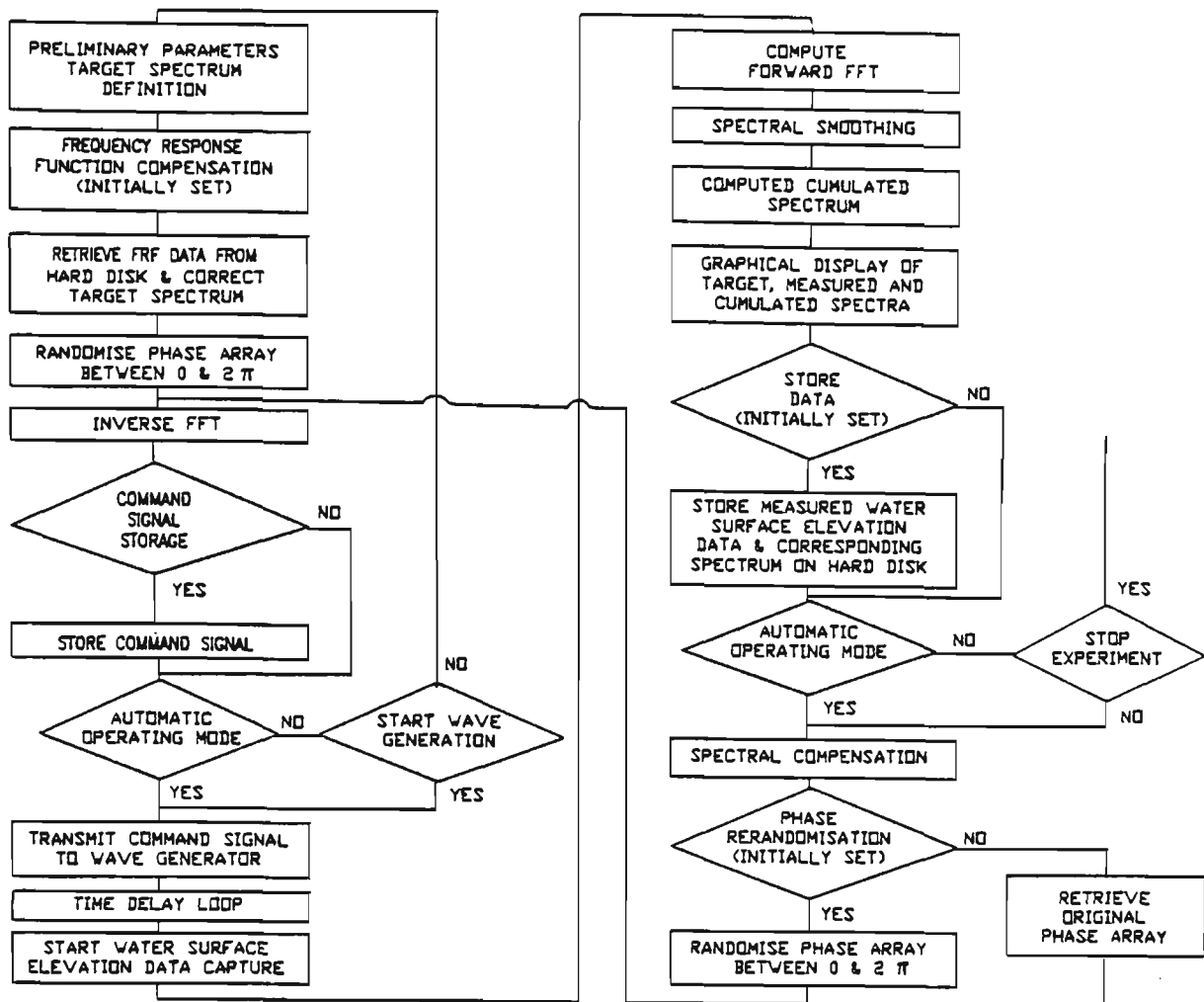


Figure 4.15. Random wave generation control flow chart .

Figure 4.15 shows the flow chart describing the operation of the WGENSP program library. The on-line screen menu, shown in figure 4.16, enables the operator to set the preliminary parameters required for random wave generation.

**Target spectrum definition.** Provisions have been made to generate the Pierson-Moskowitz, JONSWAP, and Wallops (single and double peak) spectral models. The desired target spectrum is computed by specifying the required spectral parameters, namely, spectral peak frequency, peakedness parameter (JONSWAP) and significant wave field slope (Wallops). The capability to simulate an arbitrary frequency spectrum has also been made available. This feature allows a frequency spectrum of arbitrary shape to be created by graphically specifying values of spectral density at specific frequencies. These arbitrary frequency spectra may vary from a single frequency component, resulting in a

sinusoidal command signal in the time domain, to a wide band spectrum of any specific shape. This feature may become useful in the simulation of experimentally measured spectra which are not represented mathematically.

WAVE GENERATION FACILITY  
CLOSED LOOP SPECTRUM BASED WAVE GENERATION  
(WALLOPS)

```

          OPTIONS                :[ ]  SPECTRUM SETTINGS                :[W]
GENERATE MODEL SPECTRUM          :[G]  FEEDBACK ATTENUATION (%) :[ 65 ]
START DATA GENERATION          :[S]  TIME DELAY (S) :[ 10 ]
STOP DATA GENERATION & AQUISITION :[ ]  SPECTRUM DURATION CODE :[ 2 ]
PLOT SPECTRA [L=LOG P=LINEAR]   :[P]  [ 1 = 32 SECS ] [ 8 = 256 SECS ]
ESCAPE TO DAOS                  :[E]  [ 2 = 64 SECS ] [ 16 = 512 SECS ]
RETURN TO MAIN MENU (DOS) [SHIFT]:[R]  [ 4 = 128 SECS ]
RESET ARRAYS                     :[Y]
SAVE DATA (1=YES 0=NO)         :[ 0 ]  SMOOTHING METHOD (SELECT) :[ 3 ]
DATA FILE NAME [7 CHARACTERS]:[ ]  SMOOTHING BANDWIDTH :[ 7 ]
NUMBER OF DATA SETS SAVED      :[ 0 ]  DEVICES CONSTANTS
GENERATE STORED COMMAND SIGNAL   :[ 0 ]  WAVE GENERATOR (B/■) :[ 6.827]
COMMAND SIGNAL FILENAME [5]:[ ]  WAVE PROBE (B/■) :[ 11.305]
LOOP INTERRUPT (1=YES 0=NO)     :[ 1 ]  GRAPHICS SETTINGS
TF CORRECTION (1=ON 0=OFF)     :[ 1 ]  FREQUENCY AXIS MIN.(Hz) :[ ]
PHASE RE-RANDOMIZATION ( 1/0 ) :[ 1 ]  FREQUENCY AXIS MAX.(Hz) :[ 2.200]
FEEDBACK LOOP NUMBER            :[ 0 ]  SPECTRAL DENSITY MIN. :[ ]
                                   SPECTRAL DENSITY MAX. :[ 2000]

```

Figure 4.16. On-line menu for random wave generation.

**System Frequency Response Compensation.** This option enables the initial command signal to be compensated for the frequency response characteristics of the system. When the option is invoked, the system frequency response function, previously measured and stored, is retrieved from the computer hard disk and divided into the target spectrum to provide a system-compensated spectrum. It must be noted that after generation of the initial command signal, the original system frequency response estimates become redundant as any further compensation is performed by comparison of the target spectrum with the measured spectral estimates.

**Loop Duration Code.** The loop duration code determines the nominal duration of each set of generated and acquired data and therefore the frequency resolution of both the generated spectrum and the measured (raw) spectral estimate. Both the target spectrum and the measured

spectral estimates are based on 2048 elements long arrays and the sampling rate may be set to 64, 32, 16, 8 and 4 Hz by varying the duration code. Selection of the duration code should be based on the highest frequency component of the command signal. Since the same sampling rate is used to both generate the command signal and capture the water surface elevation signal, the minimum sampling frequency should not, in this case, be based on the Nyquist frequency but on the ability of the wave generator to operate smoothly under a discrete command signal. It is recommended that the minimum sampling rate,  $f_s$ , should be governed by

$$f_s > 12 f_{max} \quad (4.6)$$

**Phase Re-randomization.** This option enables the generation of truly random waves (non periodic) as opposed to pseudo-random waves where the same random command signal is repeatedly generated over a pre-specified period. When this option is invoked, the phase of the compensated spectrum at each loop of operation is reassigned with a new set of random numbers uniformly distributed between 0 and  $2\pi$  to eliminate repetition. When this option is not used, the original phase array is combined with the compensated spectrum thus generating a pseudo-random command signal. The option may be activated or deactivated at any time during an experiment without causing any disruption to the system operation.

**Feedback Attenuation.** The level of the spectral compensation parameter,  $C_f$ , may be set initially and varied as desired during the simulation of random waves. Spectral compensation is performed according to

$$\text{Old Spectrum} = \text{New Spectrum} + C_f \left( \text{Target Spectrum} - \text{Measured Spectrum} \right) \quad (4.7)$$

When  $C_f$  is set to zero, compensation in the frequency domain does not occur and the system operates under open-loop control.

**Mode of Operation.** The closed-loop spectral feedback control system may be operated in the interrupt or automatic mode. In the

interrupt mode, the command signal is repeatedly generated until the operator allows a new, system-compensated command signal to be generated. In the automatic mode, a new system-compensated command signal is automatically generated after spectral compensation has been performed. The mode of operation may be changed at any time without disruption to the wave generating process.

**Time Delay.** In order to allow generated waves to travel from the wave maker to the wave probe, a time delay, set by the operator, is introduced between the generation of the command signal and the acquisition of the water surface elevation data.

**Spectral Smoothing Method.** Smoothing of the measured spectral estimates may be undertaken by ensemble averaging, moving spectral window or a combination of both. For control purposes, the measured raw spectral estimates at each loop of operation is smoothed (when required) by using the moving spectral window method. Two spectral window shapes are available for selection: (1) rectangular window with variable width defined by

$$G(f_i) = \frac{1}{N} \sum_{n=i-0.5(N-1)}^{n=i+0.5(N-1)} G(f_n) \quad (4.8)$$

where  $N$  is the the number of adjacent spectral components defined by the window width, and (2) three-element triangular window, also known as the Hanning spectral window, and defined by

$$G(f_i) = 0.25 G(f_{i-1}) + 0.5 G(f_i) + 0.25 G(f_{i+1}) \quad (4.9)$$

When using the rectangular window smoothing method, the window bandwidth may be adjusted during an experiment to enable the optimisation of spectral smoothing without interrupting the operation of the system. The final spectral estimates from an experiment can be computed by averaging the raw or smoothed spectral estimates stored at each loop of operation.

**Data Storage.** At any time during operation the save option may be switched on to effect permanent storage of the measured water

surface elevation data and its corresponding spectral estimates (both raw and smoothed) on the computer hard disk at each loop of operation. This option is usually activated when the agreement between the target and the measured spectral estimates is satisfactory. The stored data may subsequently be used for statistical analysis.

**Wave Probe Calibration Constant.** The most recent wave probe calibration constant, previously measured and stored, is automatically retrieved from the computer hard disk at the beginning of each experiment.

**Graphics Settings.** The range of the frequency and spectral density axes may be specified by the operator for graphical display of the target spectrum and the instantaneous and cumulated spectral estimates. This option becomes important when visually assessing agreement between the target spectrum and the measured spectral estimates.

After specification of preliminary parameters, the target spectrum is generated in an array and displayed graphically. If the system characteristics compensation option has been enabled, the previously measured frequency response estimates are retrieved, in numerical form, from the computer hard disk and are divided into the target spectrum to produce the system-compensated spectrum which is also displayed on the screen. The phase array, containing random numbers uniformly distributed between from 0 to  $2\pi$ , is merged with the system-compensated spectrum array to form a complex array. The inverse Fourier transform of the complex array is computed, resulting in the corresponding time data array which is displayed on the computer screen. When the request to start data generation is granted, the command signal is continuously transmitted to the wave maker via the digital-to-analogue conversion module. After execution of the time delay loop, the water surface elevation data, as monitored by the wave probe, are recorded through the analogue-to-digital conversion module. On completion of the data acquisition period, the spectral estimate of the recorded signal is computed by FFT and, if requested, smoothed according to the prescribed spectral smoothing method. Except for the first loop of operation, the cumulated spectral estimates

are then computed by either linear or exponential averaging. The latter is achieved by dividing the sum of the cumulated measured spectral estimates and the most recently measured spectral estimates by two. If enabled, the save option will activate the storage of both the measured water surface elevation data and its corresponding raw and smoothed spectral estimates on the computer hard disk.

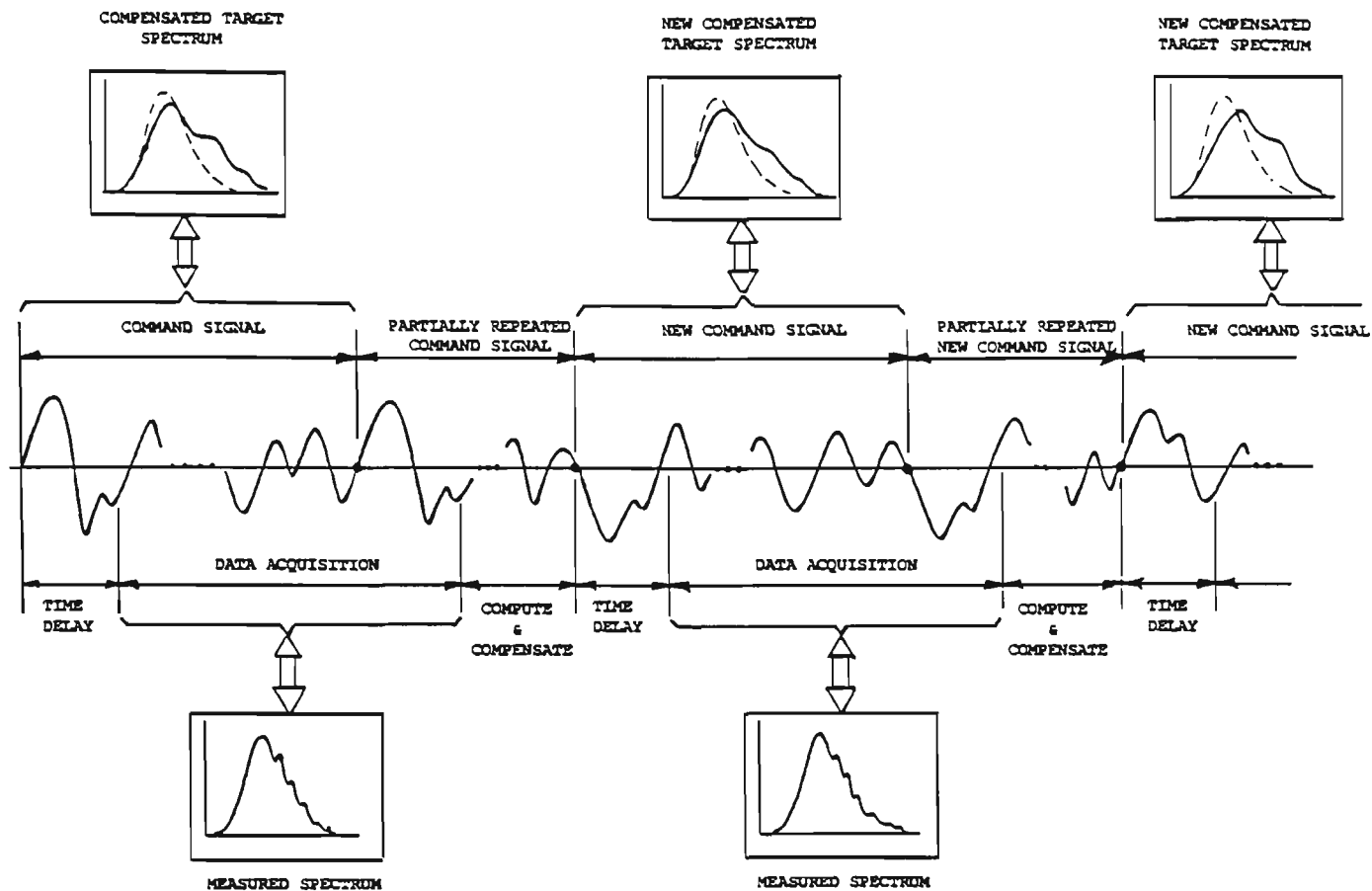


Figure 4.17. Signal generation and acquisition method for random wave generation.

The target spectrum and the measured instantaneous and cumulated spectral estimates are then displayed on screen as well as the control loop number, the feedback attenuation level, the smoothing window width, the phase re-randomisation status, the interrupt status, the save status and the number of averaged spectral estimates. If the interrupt option is activated, the operator is given the option to proceed or to stop the wave maker and terminate the experiment. Otherwise, compensation in the frequency domain is automatically undertaken and, depending on the status of the phase re-randomization option, the compensated spectrum is

merged with the original phase array or with a newly randomized phase array to form a complex array. The inverse Fourier transform of the complex array is computed resulting in a compensated command signal which is subsequently transmitted to the wave generator, overriding the previous command signal.

This method of signal generation and closed-loop spectral control enables the simulation of random waves of any duration by generating a number of relatively short time records in succession as can be seen from figure 4.17.

#### 4.6.4. System Frequency Response Measurement - WGTFS.

This program library contains a series of subroutines used to determine the frequency response characteristics of any portion of the system, for example, the command signal-to-wave maker motion frequency response function or the wave maker motion-to-water surface elevation frequency response function. The software makes use the generation of band-limited white noise synthesised into a time domain random command signal by inverse FFT. Likewise, the measurement of the frequency response is achieved by FFT. The specification of preliminary parameters, as required by the menu driven software, are outlined below:

- Noise generation level.
- Noise generation frequency range.
- Spectrum duration code - which determines the nominal duration of the command signal and therefore the frequency resolution of both the generated spectrum and the measured (raw) spectral estimates. The generated and acquired data are based on arrays of 2048 elements and the sampling rate may be set to 64, 32, 16, 8 and 4 Hz by varying the duration code.
- Number of data sets (spectral estimates) to be averaged - the frequency response function is based on the linear average of a predetermined number of raw spectral estimates.
- Time delay - the delay required to allow the waves to reach the wave probe and for the system to stabilise.

Having specified the preliminary parameters, the spectral density function array is merged with a phase array containing random numbers uniformly distributed between 0 to  $2\pi$  to form a complex array. The inverse Fourier transform of that array is then computed to produce a random time signal which is continuously transmitted to the wave maker via the digital-to-analogue conversion module. The generation of a truly random (non periodic) command signal is achieved by re-randomization of the phase array as described in section 4.6.3.

At the request of the operator the analogue-to-digital conversion module is activated after a specified time delay to simultaneously capture the system input and system output signals, for example the computer generated signal (input) and the wave probe signal (output). At the end of each data acquisition period, as determined by the loop duration code, the spectral estimates of both measured signals are computed by FFT and stored on the computer hard disk.

On completion of the data acquisition session, the raw spectral estimates are retrieved from the computer hard disk and their linear average computed to obtain smoothed spectral estimates of the input and output signals. The system frequency response function is then computed and subsequently displayed graphically on screen or plotter. The operator is then given the option to smooth the frequency response function further by one of the moving spectral window methods described in section 4.6.3. The frequency response characteristics may then be stored in numerical form on the computer hard disk for later use.

#### 4.6.5. Statistical Analysis - WGSTAT.

This collection of subroutines was developed to enable various statistical analyses of both the time and frequency domain data measured and stored during random wave simulation experiments. Initially, the experimental time records are retrieved from the computer hard disk and used to compute the highest water surface elevation peak, the lowest water surface elevation trough and the root mean square water surface elevation,  $\eta_{rms}$ . The water surface elevation maxima, defined as the points which satisfy the conditions  $\dot{\eta} = 0$  and  $\ddot{\eta} < 0$  (maxima either

above or below the mean water level), are then detected as well as the highest water surface elevation maxima and the root mean square surface elevation maxima,  $\eta_{m.rms}$ .

The zero-up-cross wave heights, defined as the difference between the highest peak and the lowest trough between two subsequent zero-up-crossing points of the time record, are detected as well as the maximum zero-up-cross wave height and the root mean square zero-up-cross wave height,  $H_{rms}$ . Similarly, the crest-to-trough wave heights, defined as the difference between any positive or negative maxima (crest) and the subsequent minima (trough), are detected as well as the maximum crest-to-trough wave height and the root mean square crest-to-trough wave height,  $H_{rms}^*$ . Finally, the spectral width parameter,  $\epsilon$ , and the significant wave height,  $H_s$ , are computed from the time records using equations (3.38) and (3.53) respectively.

Statistical analysis on the experimental spectral estimates may be performed by firstly retrieving the stored spectral data from the computer hard disk. The spectral estimates may all be displayed simultaneously to show any variation in measured spectral estimation during the experiment and the average of a specified number of spectral estimates may be computed. The zeroth, first, second and fourth spectral moments as well as the second central moment of the average measured spectral estimate are computed numerically. Due to the introduction of potentially large errors when numerically computing the higher order moments, each elementary spectral area is treated as a trapezoid and its centroid is computed accordingly as illustrated in figure 4.18. The  $n^{th}$  spectral moment  $M_n$  is computed according to

$$M_n = \sum_{i=0}^K (\omega_i)^n \cdot 0.5 [G(\omega_i) + G(\omega_{i+1})] \quad (4.10)$$

and the second central moment  $\mu_2$  is computed according to

$$\mu_2 = \sum_{i=0}^K (\omega_i - \bar{\omega})^2 \cdot 0.5 [G(\omega_i) + G(\omega_{i+1})] \quad (4.11)$$

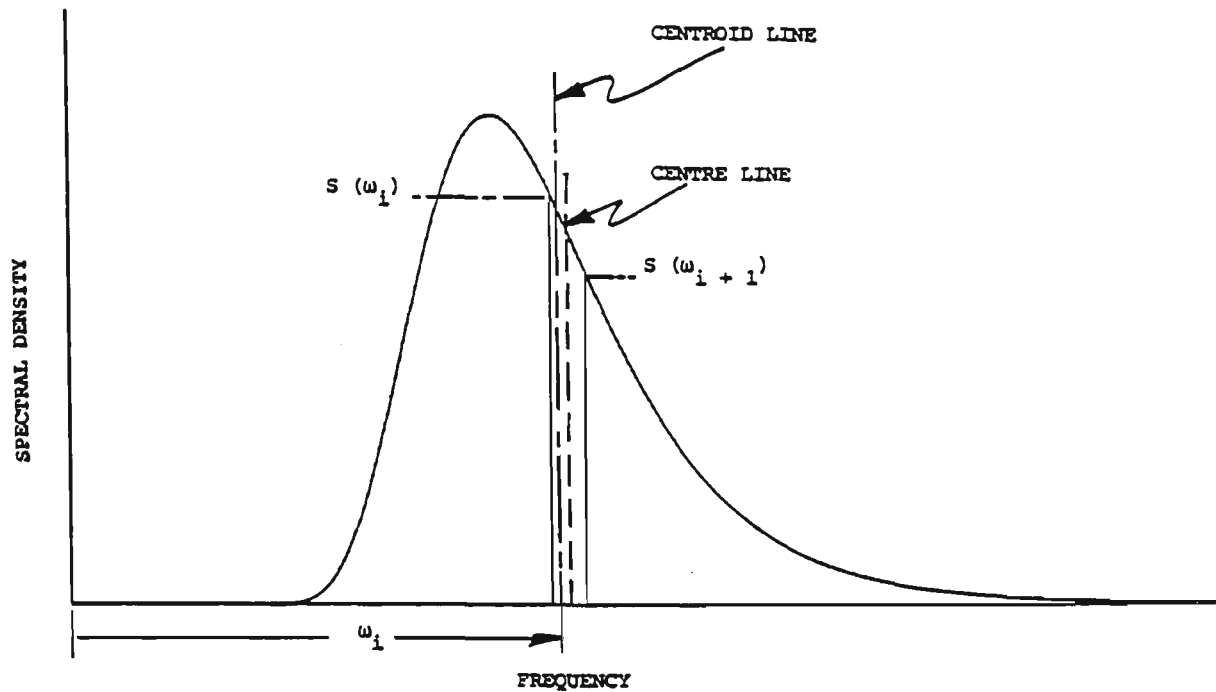


Figure 4.18. Spectral moments computation method.

The spectral width parameter,  $\epsilon$ , and the spectral bandwidth,  $\nu$ , are then computed numerically using equations (3.37) and (3.39). For single peak Wallops spectral models only, the theoretical values of  $\epsilon$  and  $\nu$  are also computed from the target spectrum - (Refer to appendix B for theoretical relationships). Finally, the following statistical parameters are computed from the average of the measured spectral estimates and displayed on the screen:

Root mean square water surface elevation - equation (3.31)

Root mean square wave amplitude - equation (3.35)

Mean frequency - equation (3.41)

Zero-up-crossing frequency - equation (3.47)

Expected height of highest maxima - equation (3.43)

Root mean square wave height - equation (3.52)

Significant wave height - equation (3.60)

The menu-driven software may then be directed to compute any of the following statistical distributions:

The water surface elevation distribution: a histogram of the normalised water surface elevation distribution ( $\eta/\eta_{rms}$ ) is computed and displayed graphically together with the theoretical Gaussian distribution (eqn. 3.34). The number of classes in the histogram is set by default to  $1.87 (N)^{0.4}$  - Cacko et. al. (1988). However, both the variance range and the number of histogram classes are selectable.

The distribution of water surface elevation maxima: a histogram of the distribution of normalised water surface elevation maxima ( $\eta_m/\eta_{m.rms}$ ) is displayed graphically together with the theoretical distribution as defined by Cartwright and Longuet-Higgins (1956) (eqn. 3.37).

The zero-up-cross wave height distribution: a histogram of the normalised zero-up-cross wave height distribution ( $H/H_{rms}$ ) is computed and displayed graphically together with the Rayleigh distribution (eqn. 3.55).

The crest-to-trough wave height distribution: a histogram of the normalised crest-to-trough wave height distribution ( $H^*/H^*_{rms}$ ) is computed and displayed graphically together with the theoretical Rayleigh distribution (eqn. 3.55).

## 5. RESULTS AND DISCUSSION

### 5.1. Experiments.

A number of experiments aimed at evaluating the performance of the wave generator and its components are presented in this chapter. Each section contains a description of the experimental methods employed together with the presentation and discussion of results.

### 5.2. Wave Probe Characteristics.

The static calibration of the wave probe was performed using the WPCAL program library described in section 4.6.1. Figure 5.1 displays the calibration curves of the wave probe for two different sensitivities.

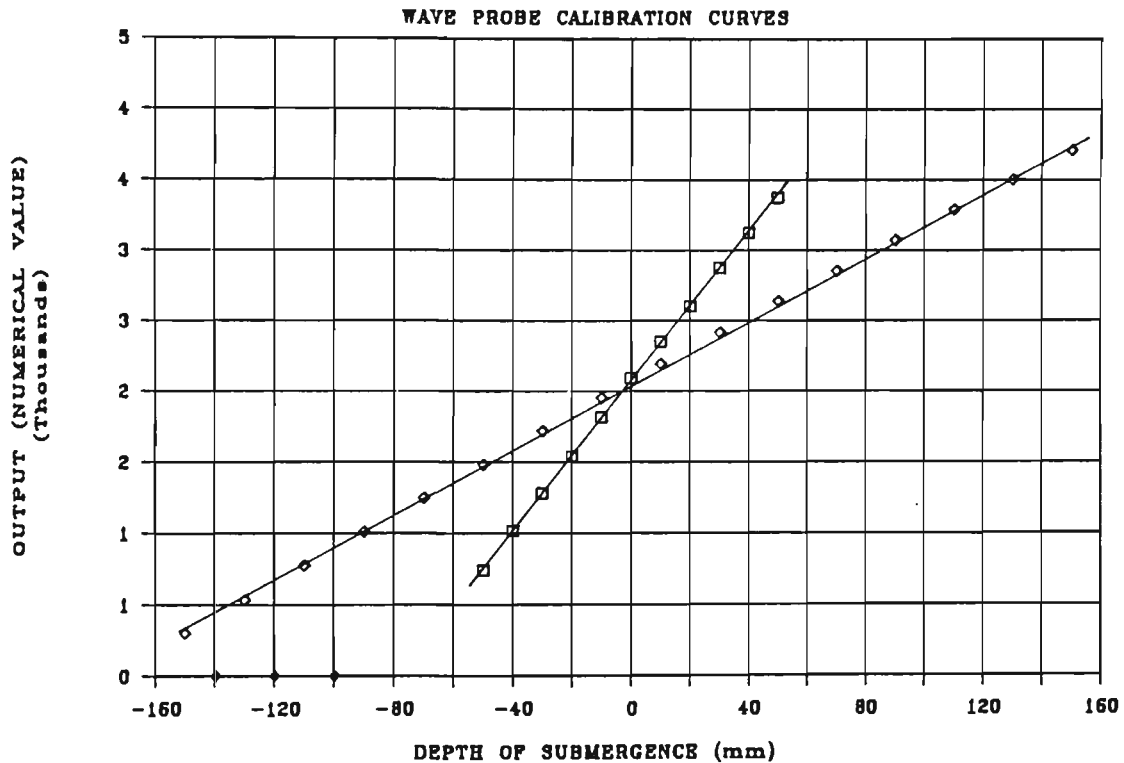


Figure 5.1. Wave probe static calibration curves.

The output is represented in numerical value as a result of the conversion of the analogue output signal by the A/D conversion module in which, for 12 Bit conversions, -5 and +5 volts are equivalent to 0 and 4095 numerical values respectively. Linear regression analysis on the

calibration data points was automatically performed by the WPCAL software. The nonlinearity of the wave probe was found to be less than 0.5 % full scale and the resolution less than 0.15 % full scale.

Another experiment aimed at establishing the dynamic response properties of the wave probe was conducted. In order to obtain the time domain response characteristics, the wave probe was subjected to a mechanical step input by means of a tension spring. The wave probe was manually raised against the spring to approximately 50 mm from a reference point and released suddenly to return to its original position. Both the motion of the wave probe, as monitored by a linear potentiometric displacement transducer, and the wave probe output (proportional to the depth of submergence) were simultaneously recorded by the micro-computer via the analogue-to-digital conversion module. The results of this experiment are displayed graphically in figure 5.2 and indicate that the time response properties of the wave probe permits the accurate measurement of vertical water surface velocity of up to 0.78 m/s. However, it must be noted that this result does not establish the true limitation of the wave probe because the step function motion attributed to the probe was not realised.

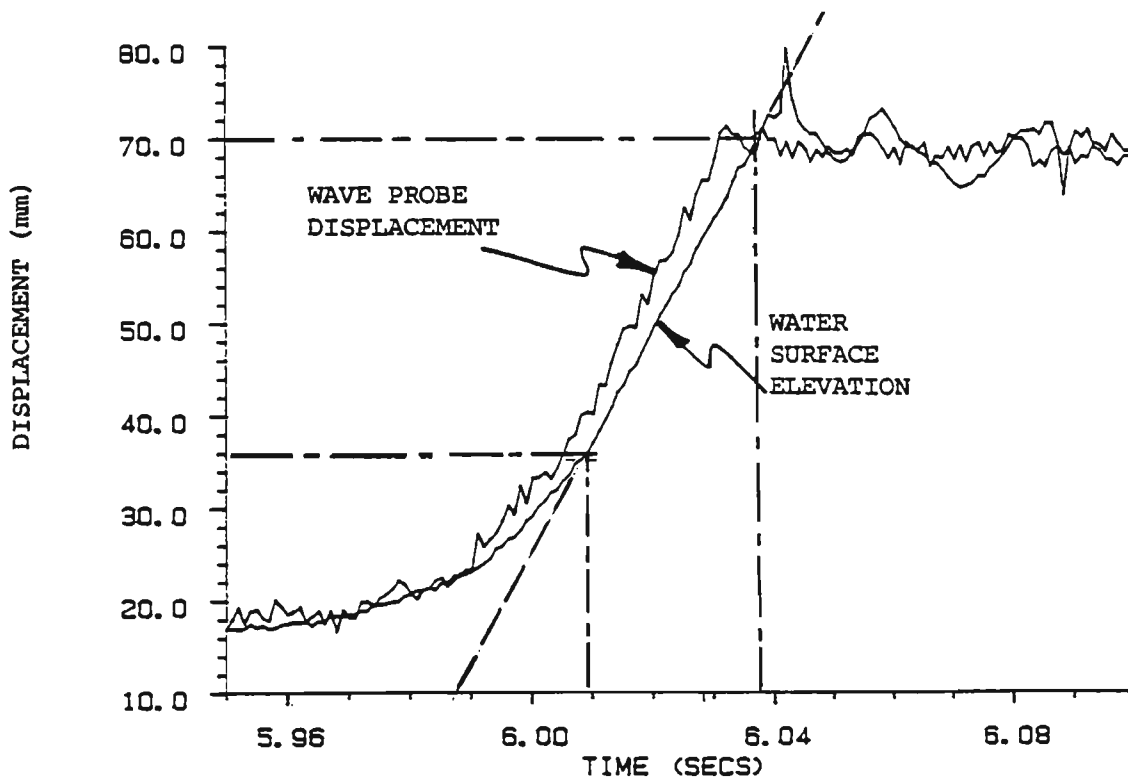


Figure 5.2. Time response characteristics of wave probe.

In order to estimate the dynamic range of the wave probe, the maximum vertical particle velocities of second order Stokes waves at the breaking limit were computed over a relevant range of frequencies. For classical Stokes waves, the maximum crest angle of a wave before breaking is 120 degrees as shown in figure 5.3.

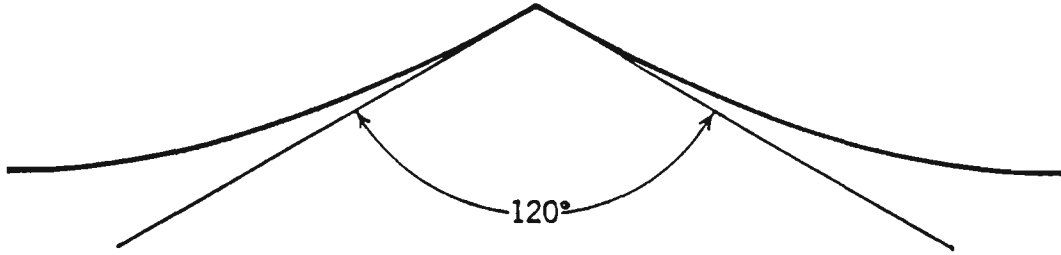


Figure 5.3. Stokes breaking wave profile.

From figure 5.3 the maximum crest angle is written as

$$\frac{d\eta}{dL} = \frac{1}{\tan(60)} \tag{5.1}$$

since  $L = C T$ , then

$$\frac{dL}{dt} = C \tag{5.2}$$

And the maximum vertical particle velocity,  $w_{max}$ , at the breaking limit is

$$w_{max} = \frac{d\eta}{dt} = \frac{d\eta}{dL} \frac{dL}{dt} \tag{5.3}$$

or

$$w_{max} = \frac{C}{\tan(60)} \tag{5.4}$$

By using equations (2.86) and (2.87) to compute the celerity,  $C$ , and the wavelength,  $L$ , respectively, the maximum vertical particle velocity at the breaking limit is plotted against frequency in figure 5.4. Additionally, the corresponding wave heights, computed from

$$H_{\max} = 0.143 L$$

(5.5)

which defines the maximum wave steepness, are also plotted against frequency as shown in figure 5.4. As can be seen from figure 5.4, the results of the time response experiment suggests that the wave probe is capable of measuring Stokes breaking waves with frequencies greater than 1.05 Hz with a still water level of 900 mm. It must be emphasized that figure 5.4 does not represent the true limitation of the wave probe which is believed to be higher than those presented here.

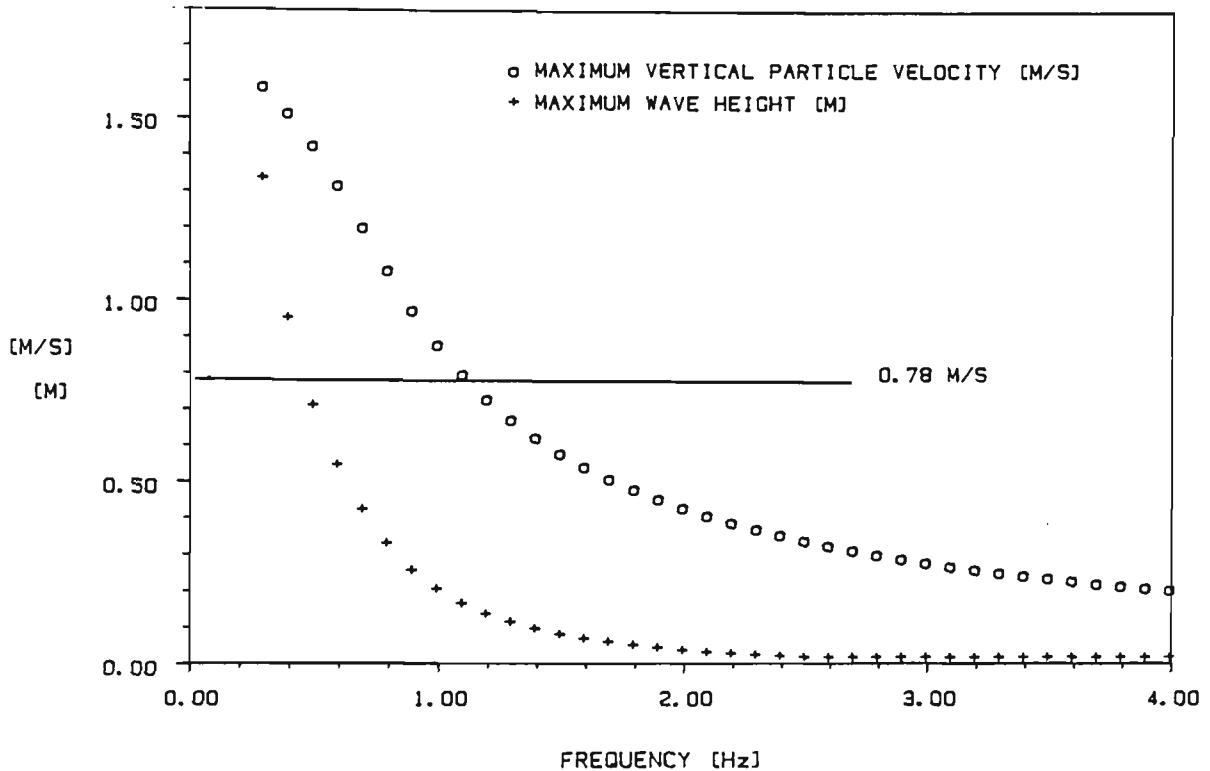


Figure 5.4. Breaking wave measurement.

### 5.3. Wave Energy Absorber Characteristics.

The performance characteristics of the wave energy absorbers were assessed using the WGRECO program library described in section 4.6.2. The reflection characteristics were determined at specific wave frequencies and slopes by generating a single component regular wave train while recording the water surface elevation from a wave probe moving along the tank. The amplitude reflection coefficient was then derived from the heights of the nodes and antinodes of the standing wave created by the addition of the incident and reflected wave trains. Experiments were conducted with

various wave slopes for regular waves with nominal frequencies of 0.5, 0.7, 0.9 and 1.1 Hz. The results are displayed graphically in figure 5.5. The wave slope was derived from the ratio of the incident wave height to wavelength where the latter was computed iteratively from the wave frequency according to the linear theory relationship of equation (2.65) which also applies to second order Stokes waves.

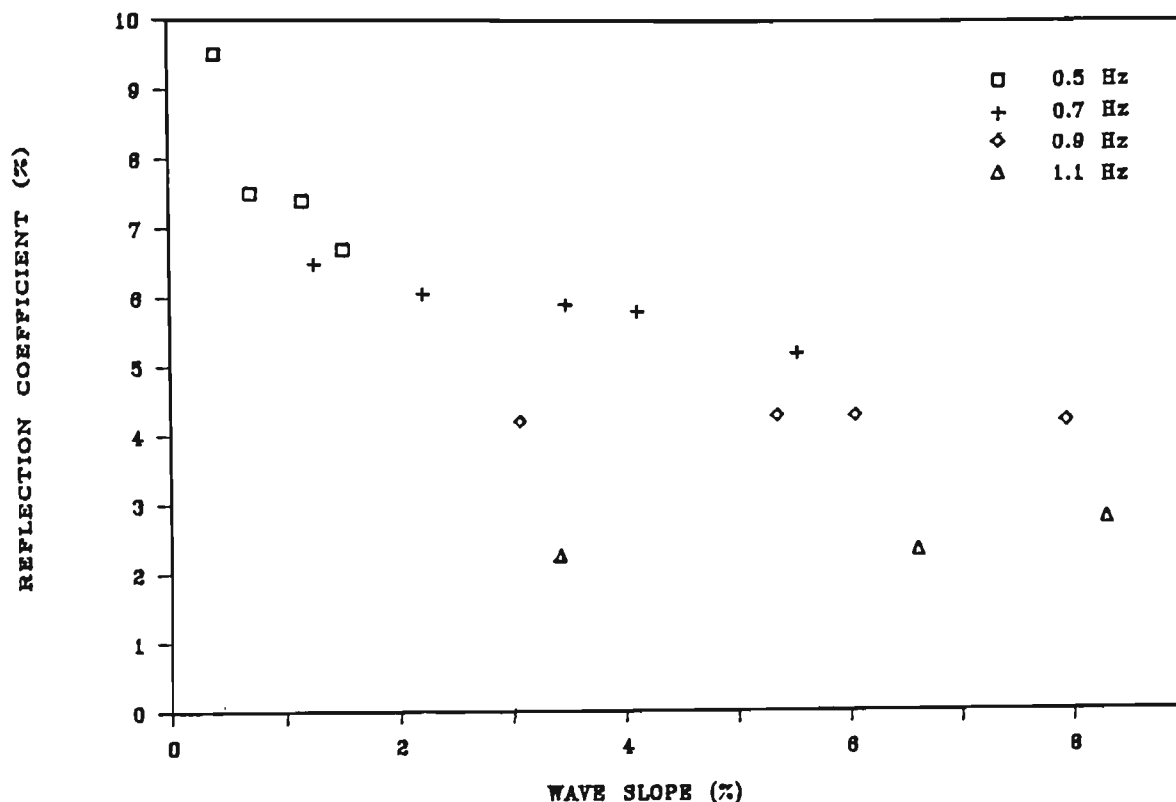


Figure 5.5. Amplitude reflection characteristics of wave tank

The above evaluation of the reflection characteristics of the wave energy absorbers shows that the amplitude reflection coefficient varied between 9.5 % for waves of small slope ( $H/L = 0.0046$ ) and approximately 2.5 % for steeper waves ( $H/L = 0.08$ ).

#### 5.4. System Frequency Response Evaluation.

A series of experiments aimed at determining the linear frequency response characteristics of the wave generator under various operating conditions were conducted using the WGTf program library described in section 4.6.4.

The system frequency response functions were determined by passing a band-limited white noise command signal through the system and using spectral analysis, namely the FFT, to graphically describe the frequency response characteristics. As shown in figure 5.6, the wave generation facility may be considered as a single or dual stage linear system.

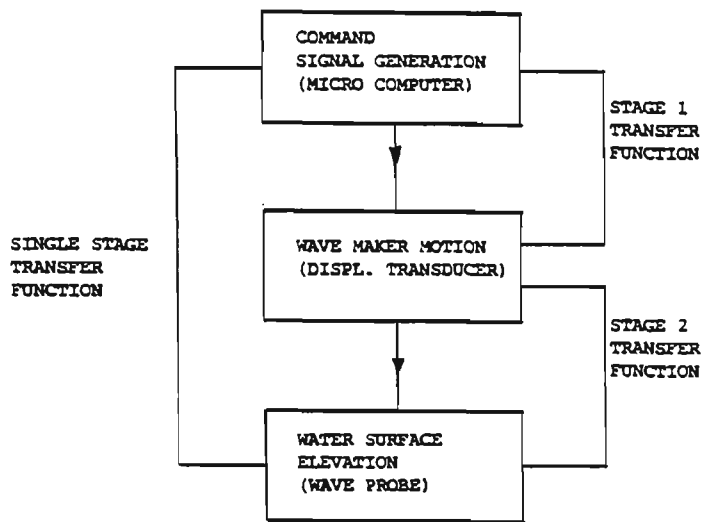


Figure 5.6. Definition of single and dual stage systems.

Characterization of the single stage linear system was made by establishing the frequency response function between the command signal as generated by the micro-computer and the water surface elevation as monitored by the wave probe. As a dual stage linear system, characterization was made by establishing two frequency response functions: firstly that between the command signal and the wave maker motion (wave generator frequency response), and secondly that between the wave maker motion and the water in the flume (hydrodynamic frequency response).

The results of the experiments are described below. All experiments were conducted with a mean water level of 900 mm.

Firstly, an experiment was conducted to establish the frequency response characteristics of stages 1 and 2 of the system independently and to determine the level of agreement with the frequency response characteristics of the single stage system.

### Experimental conditions:

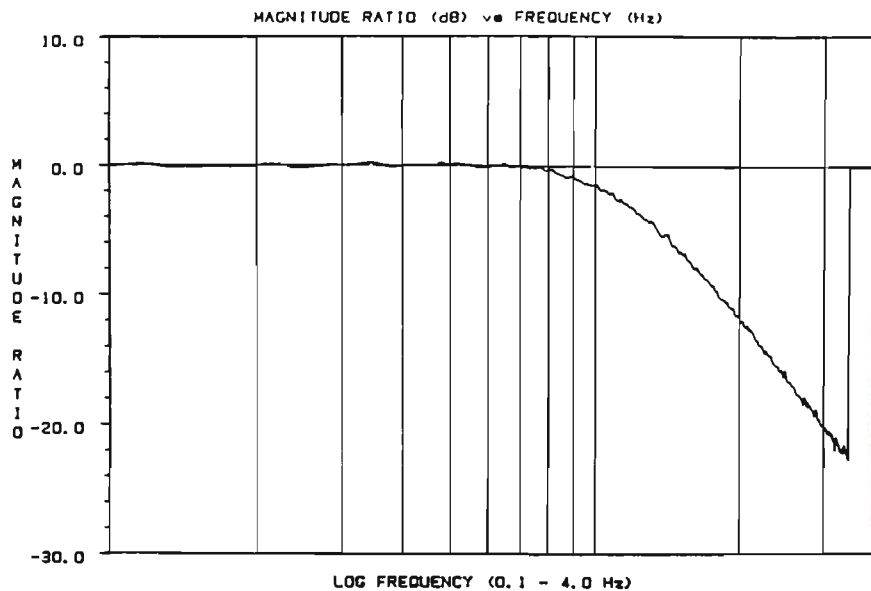
Command signal level	: 150 mm <sup>2</sup> /Hz
Command signal frequency range	: 0 - 3.5 Hz
Sampling frequency	: 32 samples per seconds
Frequency resolution	: 1/64 Hz
Wave probe location	: 10.38 m (from wave maker)
Number of spectral averages	: 30

Figures 5.7.(a) and (b) represent the resulting frequency response estimates for the first stage and second stage respectively while the frequency response estimate of the single stage system is presented in figure 5.7.(c). The frequency response estimates are the result of 30 linearly averaged raw spectra.

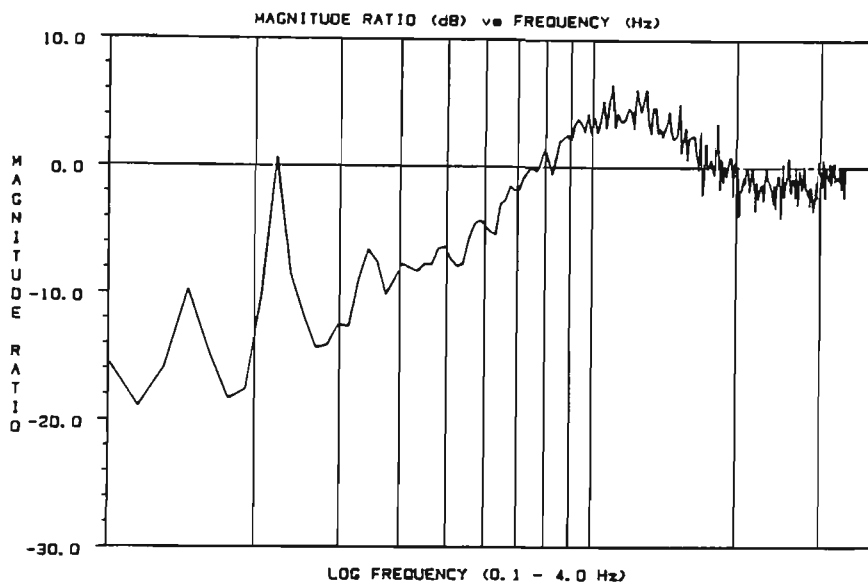
The stage 1 frequency response function - figure 5.7.(a) - reveals behaviour typical of a second order linear system with a gain drop of 40 dB per decade. The frequency response function of stage 2 - figure 5.7.(b) - shows an increase in magnitude ratio with frequency followed by a convergence towards a constant gain value which is typical of the hydrodynamic frequency response characteristics of mechanically generated waves described in the literature. The resonance peaks at approximately 0.15 and 0.29 Hz are due to the resonant frequencies of the water motion in the tank. The wavelengths corresponding to these frequencies, as approximated by equation (2.65), were found to be 19.74 and 9.825 metres respectively which correspond approximately to the effective length and half length of the wave tank.

It can be seen that the frequency response estimates of the single stage system presented in figure 5.7.(c) is characterised by the combination of both single stage systems.

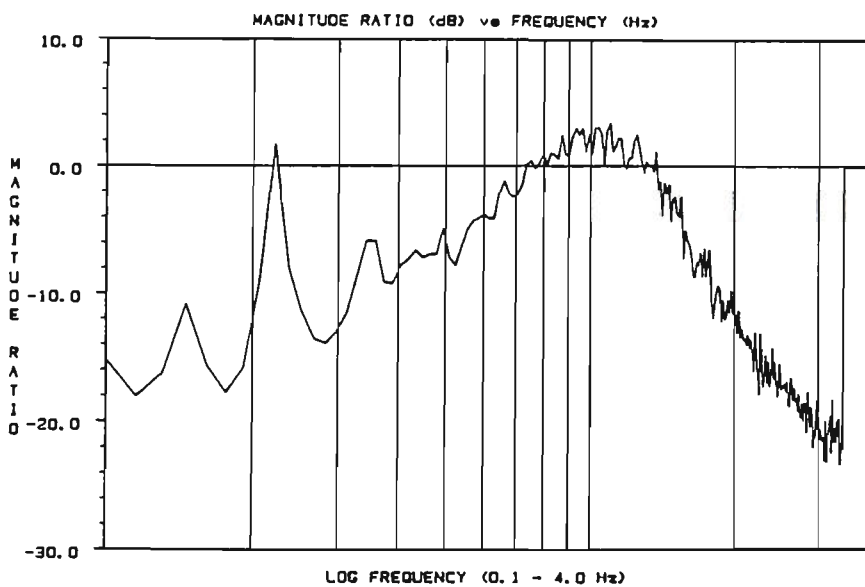
With the aim of demonstrating the additive properties of the system, the frequency response estimates of stages 1 and 2 of the dual stage system shown together in figure 5.7.(d) are combined together in figure 5.7.(e) and compared with the single stage frequency response estimate in figure 5.7.(f).



(a) Stage 1 - dual stage system.

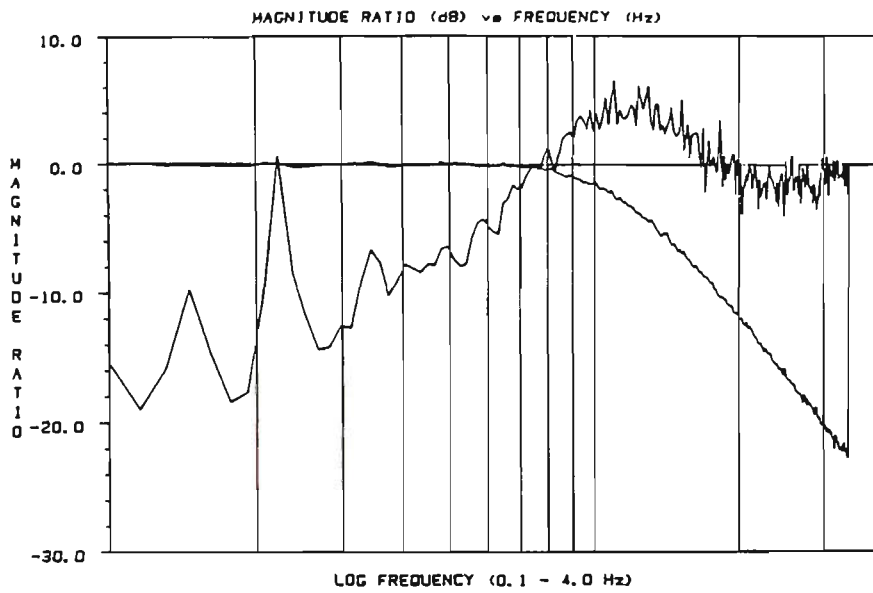


(b) Stage 2 - dual stage system.

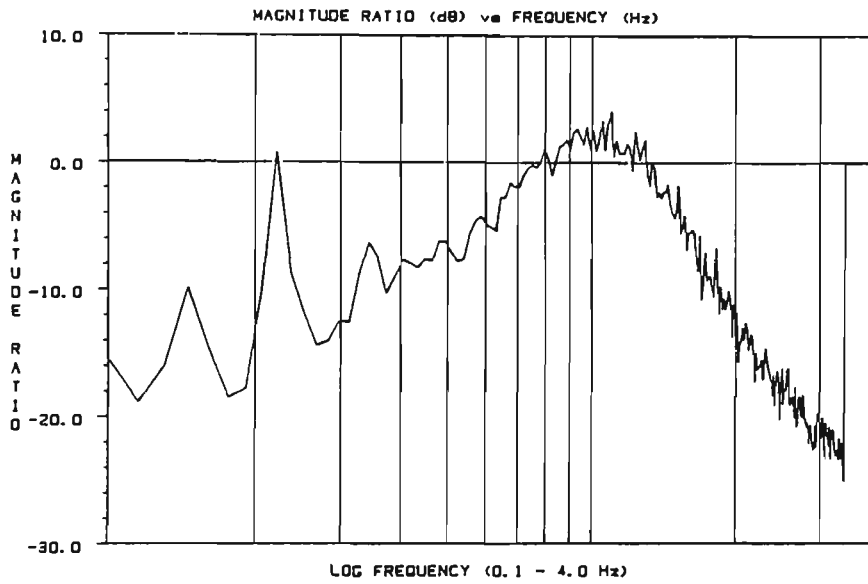


(c) Single stage system.

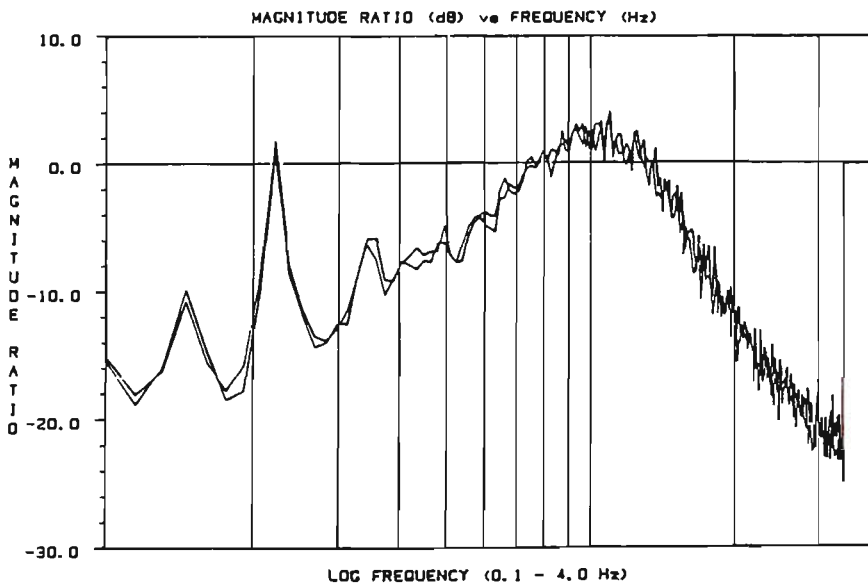
Figure 5.7. Single and dual stage system frequency response estimates.



(d) Stages 1 and 2 of dual stage system.



(e) Combination of stages 1 and 2 of dual stage system.



(f) Single & dual stage system.

Figure 5.7. Single and dual stage system frequency response estimates.

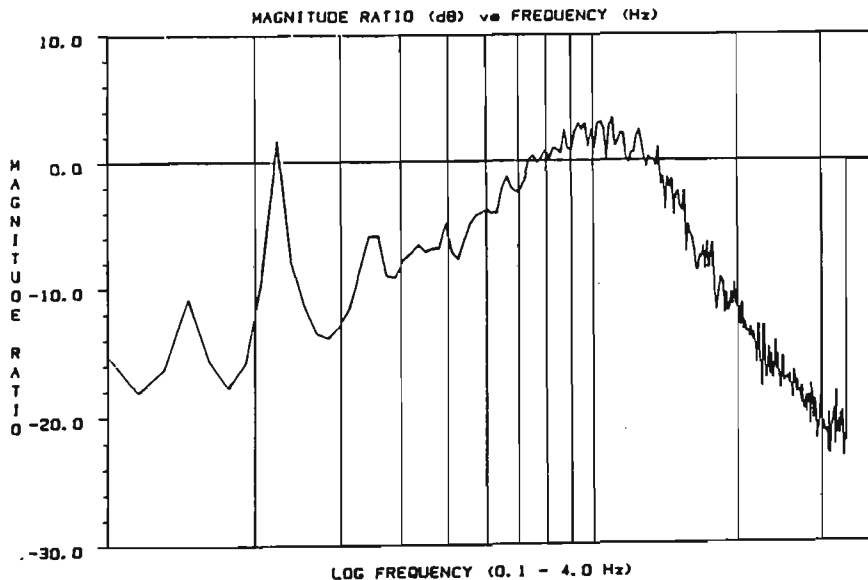
As can be seen from figure 5.7.(f), good agreement exists between both methods of estimating the system frequency response characteristics.

It was thought of interest to investigate the effects, if any, of the location of the wave probe on the system frequency response characteristics. A second experiment was conducted in which a band-limited white noise command signal was used measure the system frequency response with the wave probe located at 12.25, 9.50 and 6.75 metres from the wave maker.

**Experimental conditions:**

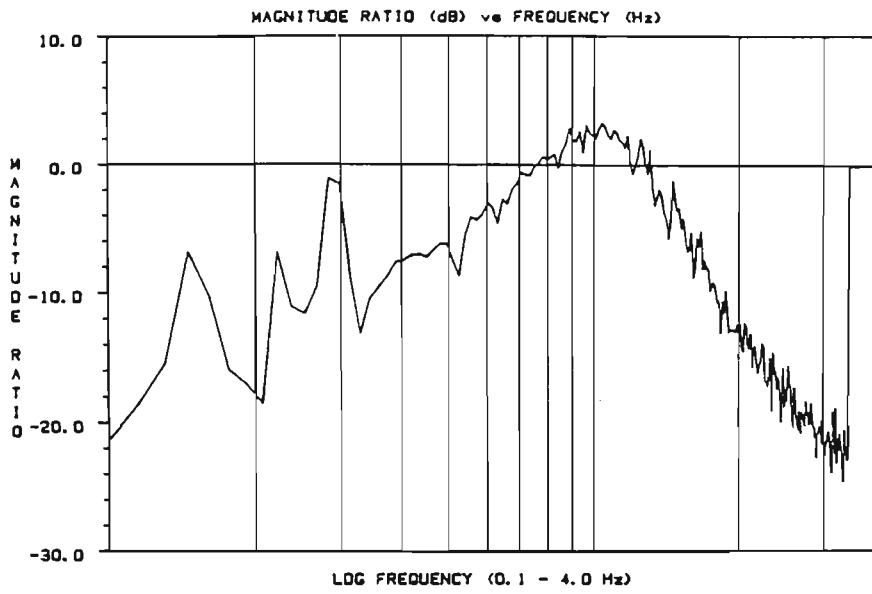
Command signal level	: 150 mm <sup>2</sup> /Hz
Command signal frequency range	: 0 - 3.5 Hz
Sampling frequency	: 32 samples per seconds
Frequency resolution	: 1/64 Hz
Number of spectra averaged (per test)	: 30

The resulting frequency response estimates are displayed in Figures 5.8.(a), (b) and (c) for the wave probe located at 6.75 metres, 9.50 metres and 12.25 metres from the wave maker respectively. In order to facilitate comparison, all three spectral estimates are also displayed on common axes in figure 5.8.(d).

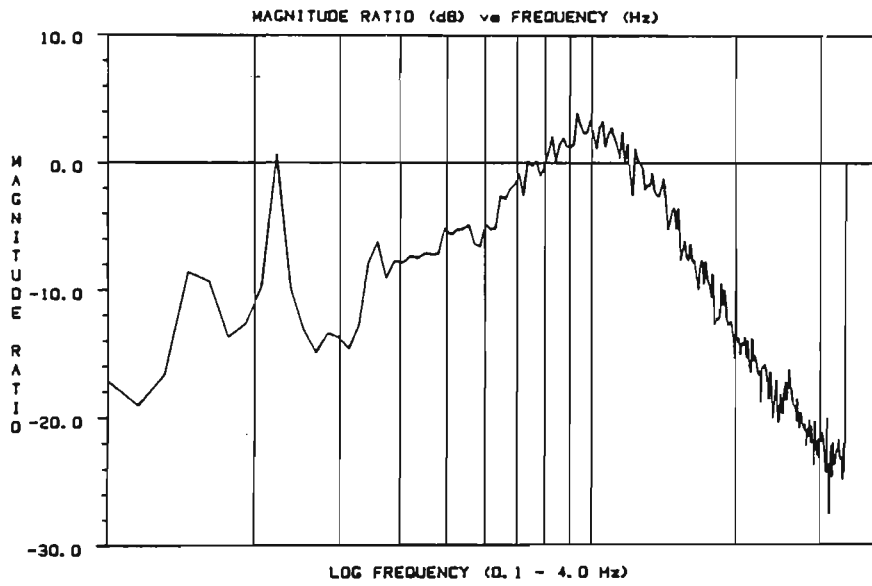


(a) Wave probe at 6.75 metres.

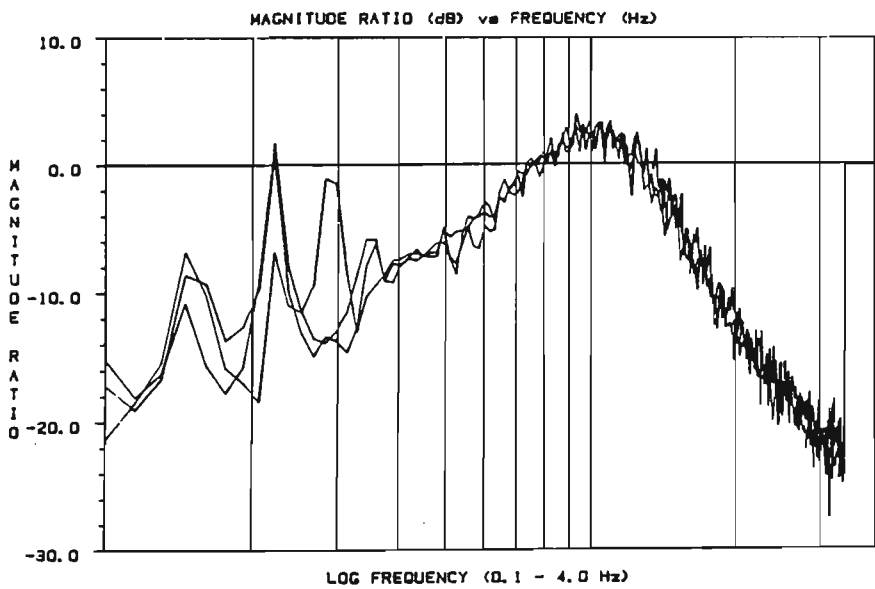
Figure 5.8. Variation of frequency response with wave probe location.



(b) Wave probe at 9.50 metres.



(c) Wave probe at 12.25 metres.



(d) Wave probe at 6.75, 9.50 and 12.25 metres.

Figure 5.8. Variation of frequency response with wave probe location.

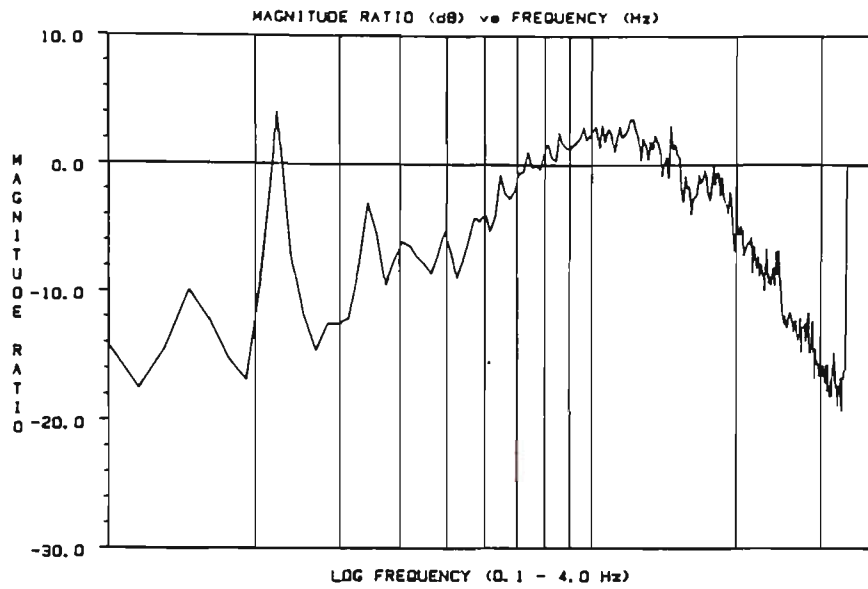
It can be seen from these graphical results that the location of the wave probe has negligible effect on the measured system frequency response over the range of distance studied.

An third experiment, aimed at investigating the effects of the level of a band limited white noise input signal on the frequency response characteristics of the system, was conducted. Two separate tests were conducted in which all relevant parameters were kept constant with the exception of the white noise input signal level which was set at 25  $\text{mm}^2/\text{Hz}$  for the first test and 150  $\text{mm}^2/\text{Hz}$  for the second test.

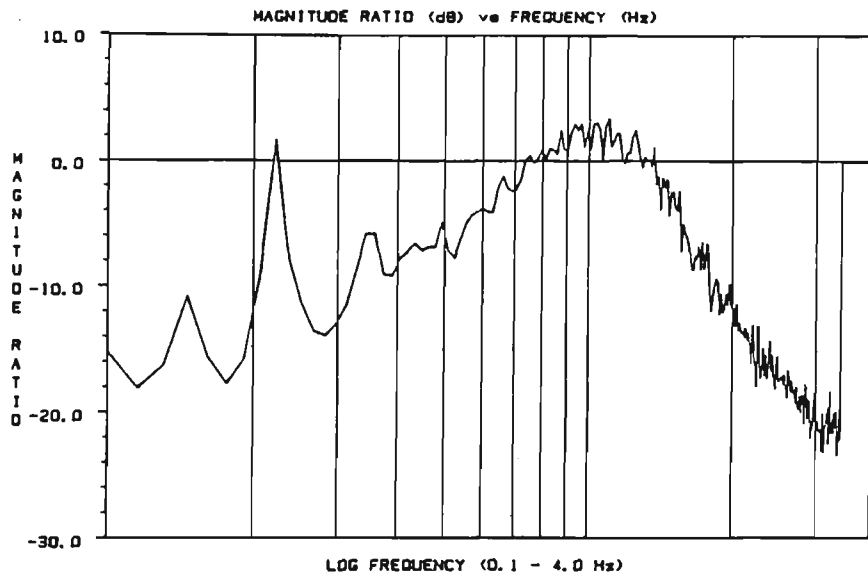
**Experimental conditions:**

Command signal level	: 25 and 150 $\text{mm}^2/\text{Hz}$
Command signal frequency range	: 0 - 3.5 Hz
Sampling frequency	: 32 samples per seconds
Frequency resolution	: 1/64 Hz
Number of spectra averaged (per test)	: 30

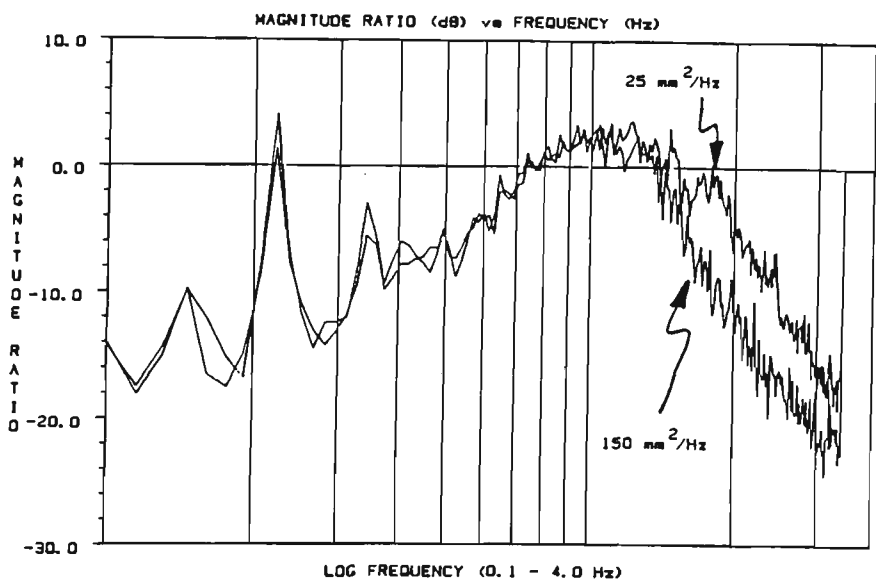
The resulting frequency response estimates are shown in Figure 5.9.(a) and (b) for the first and second tests respectively. From figure 5.9(c), where the frequency response estimates of both tests are plotted together, it is evident that the system frequency response function was affected by the level of the input signal especially for frequencies exceeding 1 Hz. These results confirm the presence of nonlinearities in the system.



(a) Input signal level:  $25 \text{ mm}^2/\text{Hz}$ .



(b) Input signal level:  $150 \text{ mm}^2/\text{Hz}$ .



(c) Input signal levels:  $25$  &  $150 \text{ mm}^2/\text{Hz}$ .

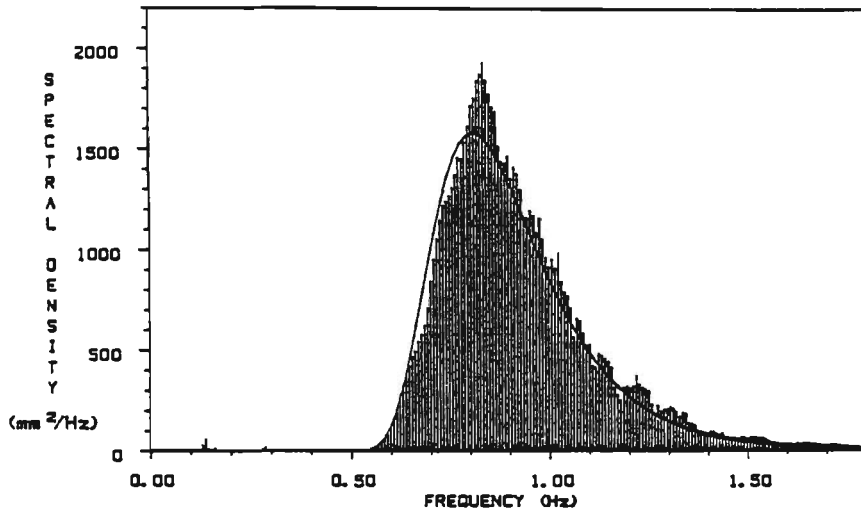
Figure 5.9. Variation of frequency response with input signal level.

### 5.5. Comparison of Open and Closed-Loop Random Wave Generation Control.

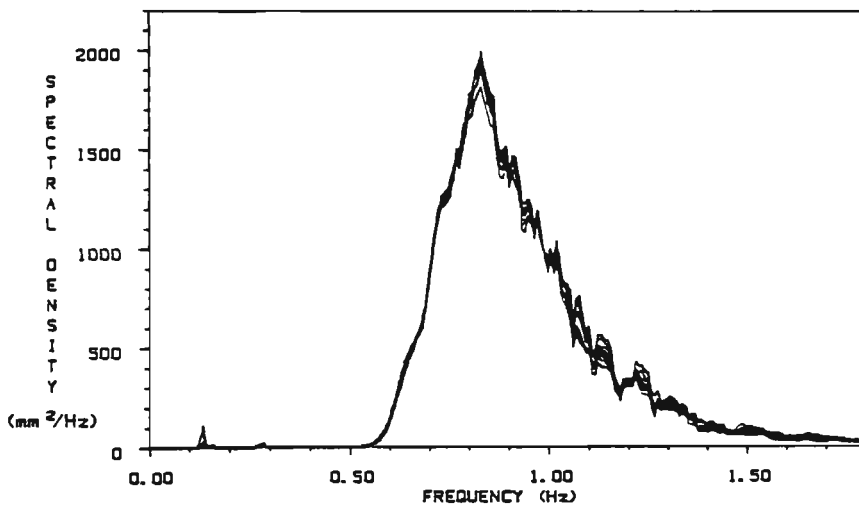
A number of experiments were conducted with the aim of demonstrating the superiority of the closed-loop spectral feedback compensation control technique over open-loop control. This was achieved by generating random waves based on a spectral model using the WGENSP software described in section 4.6.3. All experiments were conducted with a still water level of 900 mm. A Wallops spectrum with a spectral peak frequency of 0.8 Hz and a significant wave field slope of 0.01 was selected as a target spectrum. The duration of the time signal for each loop of operation was set at 128 seconds. After specifying parameters defining the target spectrum and the operating conditions of the machine, the wave generator was switched on and the command signal transmitted to the system. The save option was immediately activated to enable the storage of both the measured water surface elevation data and their corresponding spectral estimates. Upon reaching a predetermined period of wave generation, the system was halted and the linear average of the measured spectral estimates was computed. All experimental results are displayed graphically on linear scales.

In the first experiment, the target spectrum was compensated to accommodate the system frequency response function which was measured and stored prior to the experiment. Random waves were then simulated for 12 loops of operation with the control system set to open-loop. The experiment was then repeated under the same conditions for 12 loops of operation with the control system set to closed-loop. The results from both the open and closed-loop tests are shown in figure 5.10 and 5.11 respectively. All measured spectral estimates were smoothed with a rectangular moving spectral window of 0.0703 Hz (9/128 Hz) bandwidth before being averaged to obtain the final spectral estimate. Graphs (a) of figures 5.10 and 5.11 show the linear average of all 12 measured spectral estimates together with the target spectrum while graphs (b) show all 12 individually measured spectral estimate at each loop of operation.

As may be seen from figures 5.10 and 5.11, the measured spectral estimates obtained from the generation of random waves under both open and closed-loop control exhibit good agreement with the target spectrum. Although quite satisfactory, wave generation under open-loop control was inferior to that under closed-loop control.

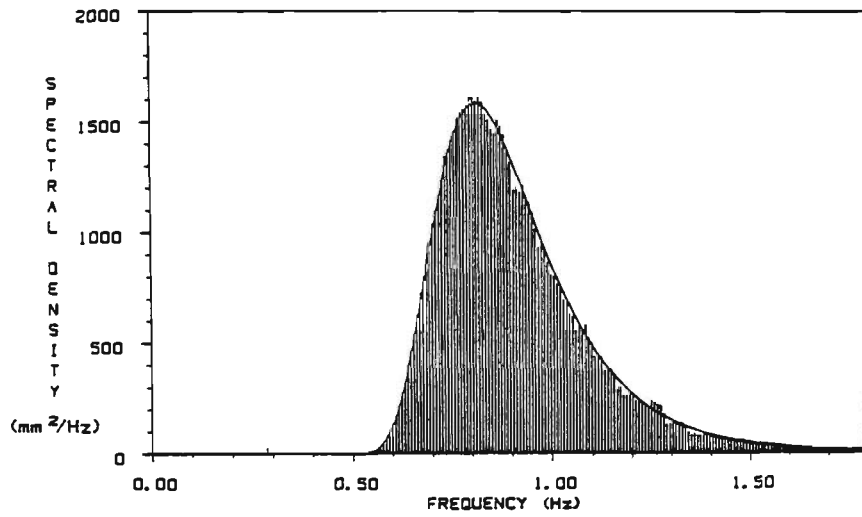


(a) Average of 12 measured spectral estimates.

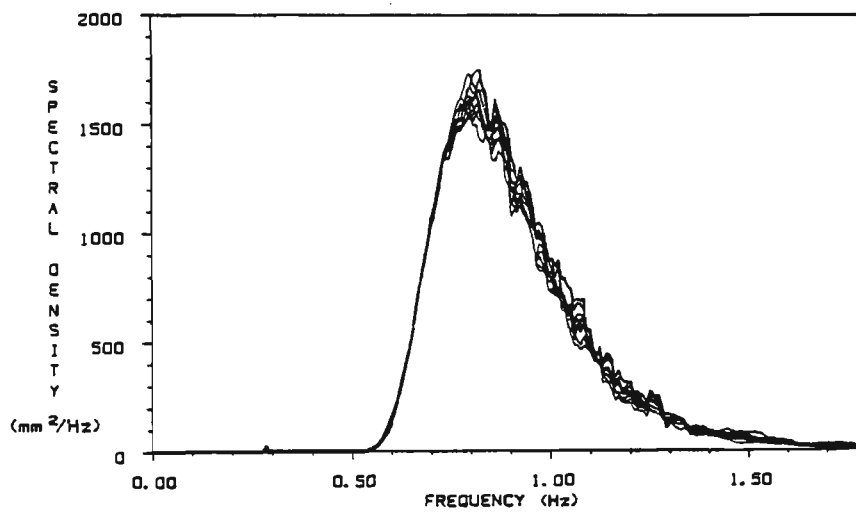


(b) Individually measured spectral estimates (12).

Figure 5.10. Open-loop spectral estimates.



(a) Average of 12 measured spectral estimates.

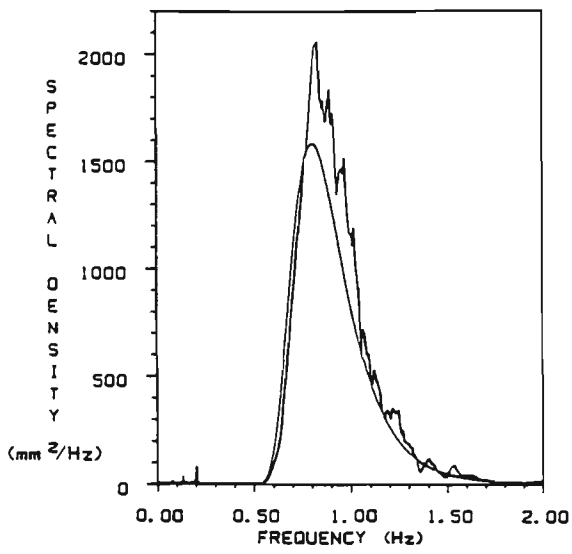


(b) Individually measured spectral estimates (12).

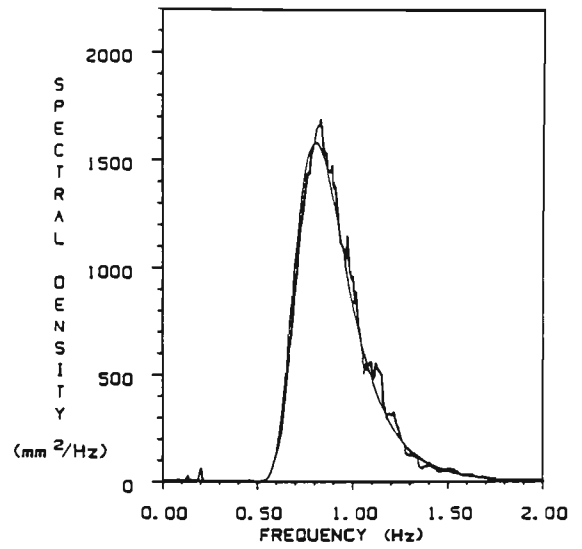
Figure 5.11. Closed-loop spectral estimates.

Using the same target spectrum and experimental conditions as in the previous experiment, random waves were generated under closed-loop control with the feedback attenuation parameter set at 65 %. However, the initial command signal was not compensated to account for the system frequency response characteristics. Random waves were generated until agreement between the measured spectral estimates and the target spectrum was achieved. Figure 5.12 shows the history of the measured spectral estimates for each loop of operation together with the target spectrum. All measured spectral estimates were smoothed with a rectangular moving spectral window of 0.0703 Hz (9/128 Hz) bandwidth.

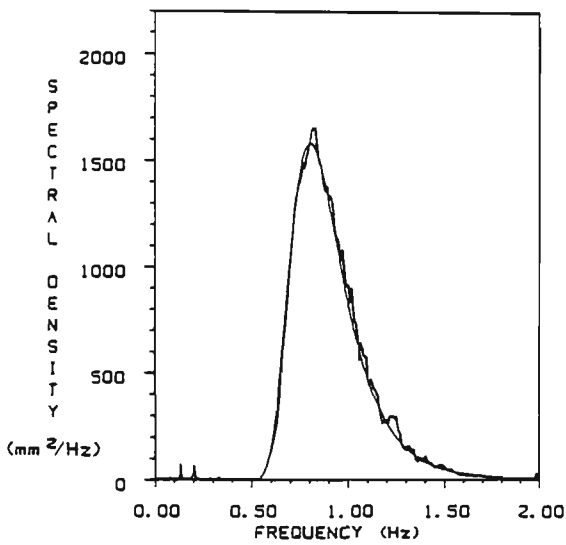
As may be seen from figure 5.12, the agreement between the target spectrum and the measured spectral estimates improves with time and becomes acceptable after just the second loop of operation. These results demonstrate that the generation of random waves with the closed-loop spectral compensation technique can be achieved without the need to accurately evaluate the system frequency response before each experiment.



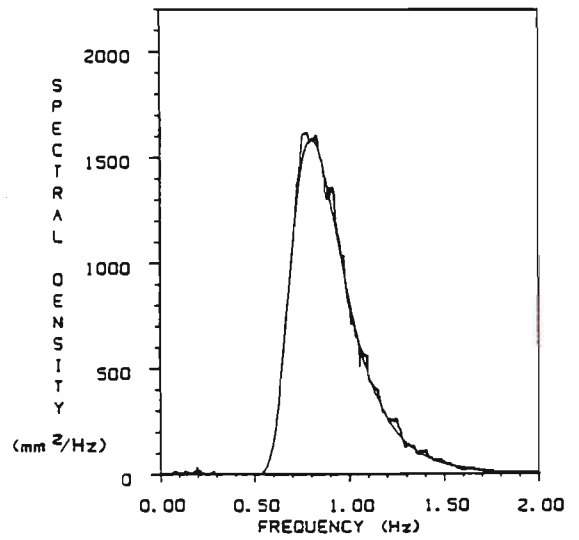
(a) Loop 1.



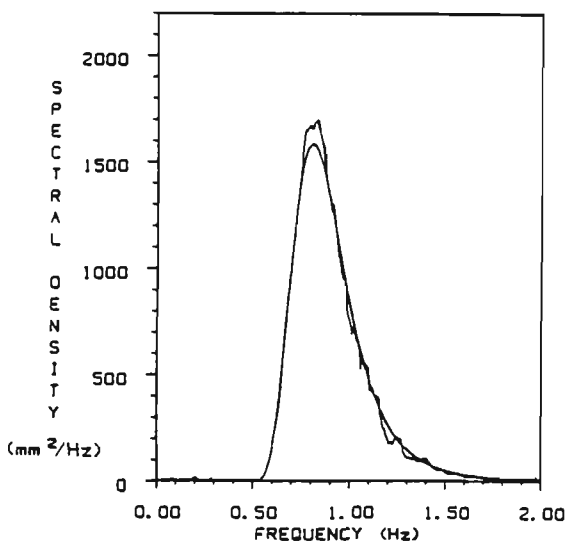
(b) Loop 2.



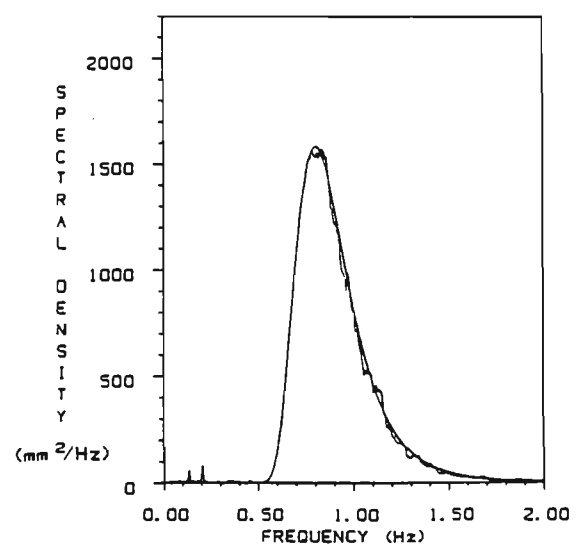
(c) Loop 3.



(d) Loop 4.



(e) Loop 5.

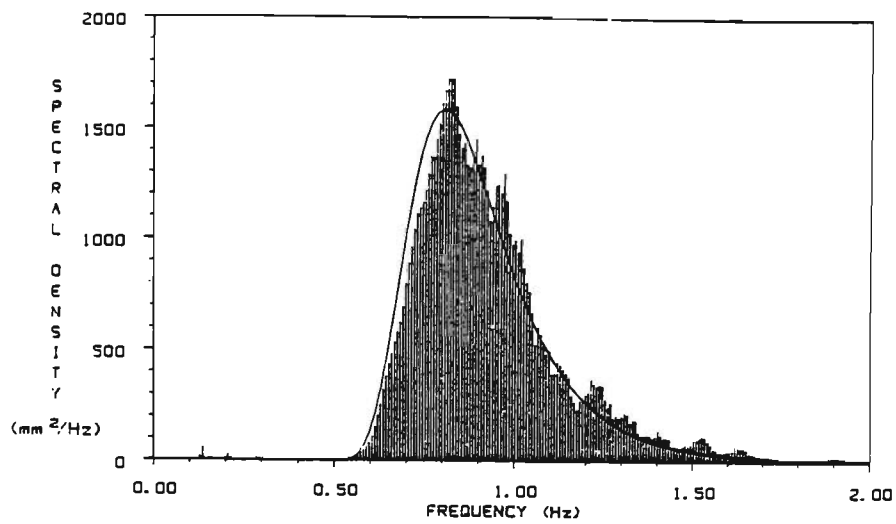


(f) Loop 6.

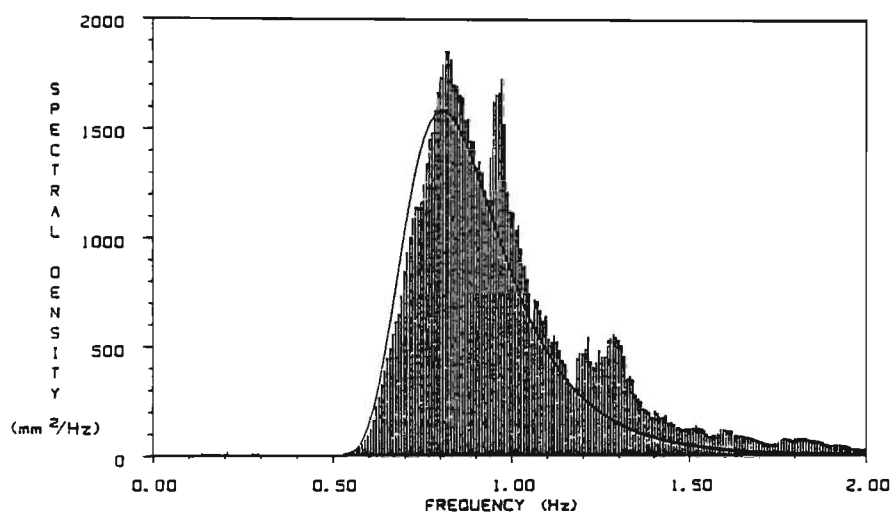
Figure 5.12. History of measured spectral estimates.

A third experiment was conducted to characterise the behaviour of the control system when a disturbance was introduced into the wave field. The target spectrum, compensated to accommodate the system frequency response characteristics, was generated with the control system initially set on open loop. During the fifth loop of operation an obstruction, in the form of a 0.5 metre wide by 1.0 metre long rectangular barge weighting 30 kg, was placed in the wave tank 3 metres behind the wave probe. During the 10th loop of operation the closed-loop spectral feedback compensation control system, with the feedback attenuation parameter set to 65 %, was activated with the barge still in the wave tank. Wave generation was then continued for a further 4 control loops. All measured spectral estimates were smoothed with a rectangular moving spectral window of 0.0703 Hz (9/128 Hz) bandwidth before being averaged to obtain the final spectral estimate.

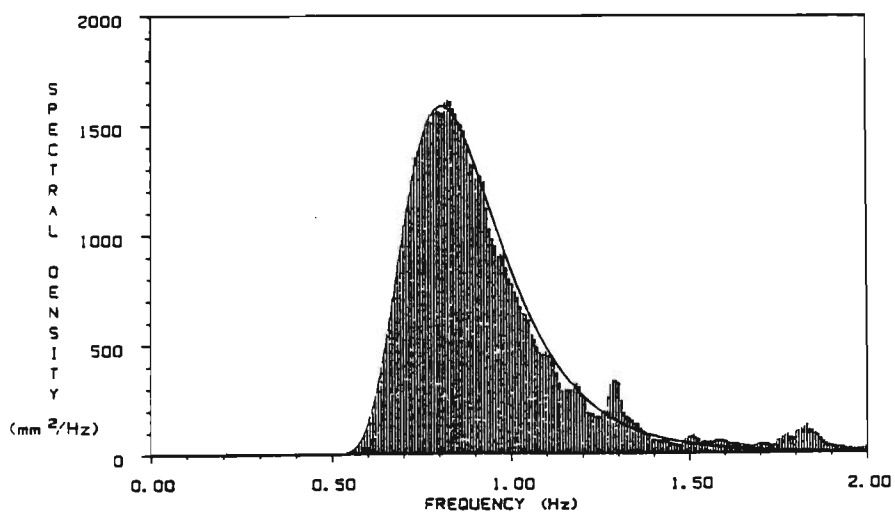
Figure 5.13(a) shows the linear average of the measured spectral estimates for the first 4 loops of operation (open-loop), figure 5.13(b) shows the linear average of the measured spectral estimates for loops 5 to 9 inclusive (open-loop with obstruction) and figure 5.13(c) shows the linear average of the measured spectral estimates for loops 10 to 15, inclusive, (closed-loop with obstruction). For comparison, the target spectrum is also displayed with the linear average of the measured spectral estimates. As may be seen from figure 5.13(a), reasonable agreement between the target spectrum and the measured spectral estimates is initially achieved under open-loop control. However, the introduction of an obstruction creates disturbances in the wave field which cannot be compensated by open-loop control, as shown in figure 5.13(b). It can be seen from figure 5.13(c), however, that the agreement between the target spectrum and the measured spectral estimates is improved by introducing closed-loop spectral feedback control which compensates for the spurious disturbances in the wave field.



(a) Average of 4 spectral estimates - open-loop.



(b) Average of 5 spectral estimates - open-loop with obstruction.



(c) Average of 6 spectral estimates - closed-loop with obstruction.

Figure 5.13. Control system recovery.

As may be seen from the results of the initial experiment, the generation of random waves from spectral models may be undertaken with an open-loop system when the target spectrum is initially compensated for the system frequency response. The agreement between the target spectrum and the measured spectral estimates is superior when the system operates under closed-loop spectral feedback compensation control. This suggests that the performance of the system under open-loop control is highly dependent on the accuracy of the separately measured system frequency response.

As demonstrated in the second experiment, the generation of random waves from spectral models under closed-loop control may be achieved without initially compensating the target spectrum for the system frequency response. Compensation was in fact achieved within the first two loops of operation. This feature eliminates the need to reassess the system frequency response before each experiment when one or more system-dependent parameters are varied, for example, the still water level, the shape of target spectrum or the level of the input command signal. It must be noted that although the closed-loop control system requires some time for agreement to be reached between the target spectrum and the measured spectral estimates (approximately 2 loops or 4 minutes in this case), the accurate measurement of the system frequency response characteristics would be much more time consuming.

The superiority of closed-loop spectral feedback control over the open-loop control was further emphasized by the results of the final experiment where the recovery of agreement between the target spectrum and the measured spectral estimates by closed-loop control was demonstrated. The ability of the closed-loop control system to recover from the introduction of disturbances in the wave field should prove a useful feature when conducting scale modelling tests.

### 5.6. Generation of Single Peak Spectral Models.

This series of experiments were conducted to investigate the effectiveness of the facility for generating a range of single peak spectra. Various single peak spectral models were simulated using the WGENSP program library described in section 4.6.4. Statistical analysis of the measured water surface elevation records together with their corresponding spectral estimates were performed with the WGSTAT program library described in section 4.6.5. Four Wallops spectra and one Pierson-Moskowitz spectrum with various spectral bandwidths, spectral peak frequencies and spectral densities, were selected as target spectra in five separate experiments. These spectral models, displayed in figure 5.14, were selected to represent a wide range of sea conditions ranging from gentle swells to storms. All experiments were conducted with a still water level of 900 mm and the control system was set on the closed-loop spectral feedback mode.

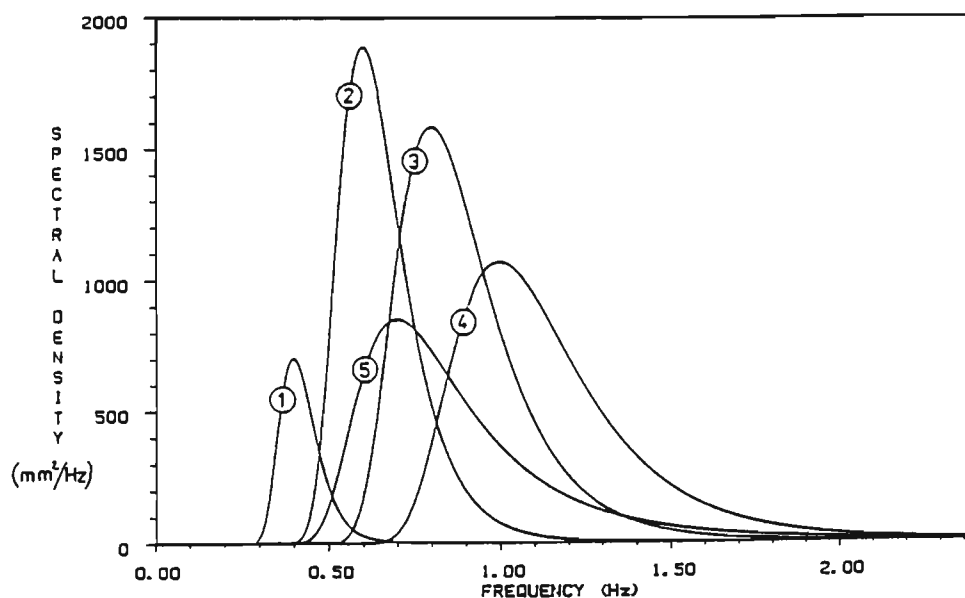


Figure 5.14. Single peak target spectra.

In order to establish the statistical properties of the input command signal, the normalised distribution of a typical sample command signal was computed and is displayed in figure 5.15 together with the theoretical Gaussian distribution. As can be seen from figure 5.15, it may be assumed that the input command signal is Gaussian.

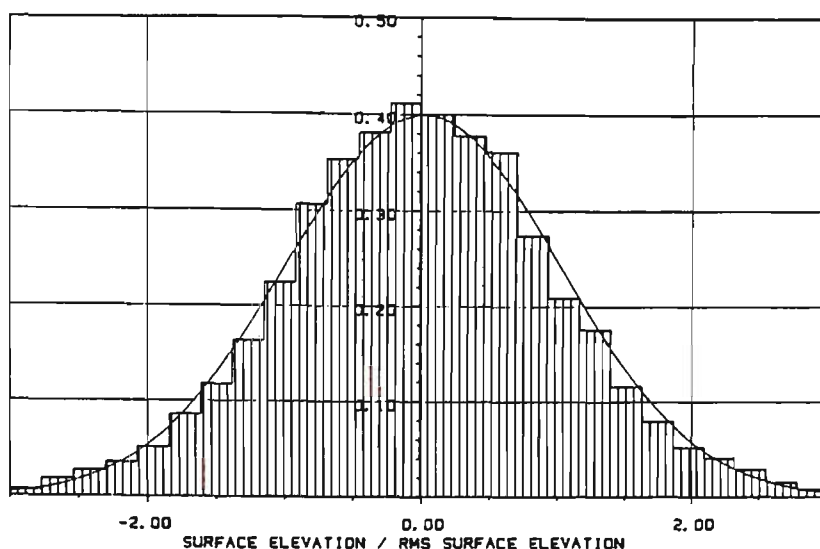


Figure 5.15. Typical command signal distribution.

Each target spectrum, together with the experimental conditions, are specified in table 5.1 below.

Experiment number	:	1	2	3	4	5
Target spectral model	:	Wallops	Wallops	Wallops	Wallops	P-M
Spectral peak frequency (Hz)	:	0.4	0.6	0.8	1.0	0.7
Significant slope of wave field, $\xi$	:	0.001	0.005	0.01	0.15	n/a
Nominal energy content ( $\text{mm}^2$ )	:	95.2	470.2	595.1	548.5	416.6
Nominal spectral width parameter, $\epsilon$	:	0.299	0.389	0.464	0.533	
Loop duration (seconds)	:	256	128	128	128	64
Frequency resolution (Hz)	:	3/256	5/128	9/128	13/128	6/64
Number of spectral estimates	:	8	20	12	5	6

Table 5.1. Experimental conditions - single peak spectrum.

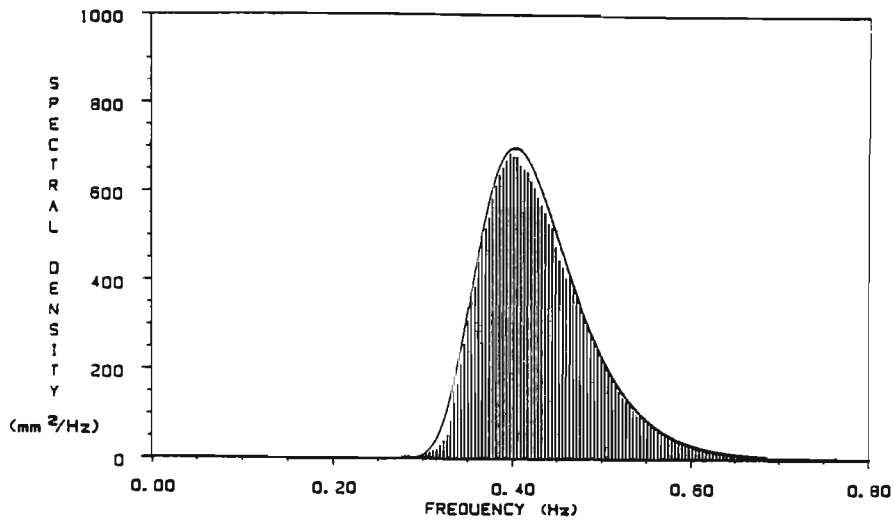
The results of experiments 1 to 5 are displayed in figure 5.16 to figure 5.20 respectively where graphs (a) show both the linear average of the measured spectral estimates together with the target spectrum while graphs (b) show the individually measured spectral estimates of the simulated wave field at each loop of operation. Finally, in graphs (c) the normalised water surface

elevation distribution of the measured wave field is presented together with the theoretical normalised Gaussian distribution.

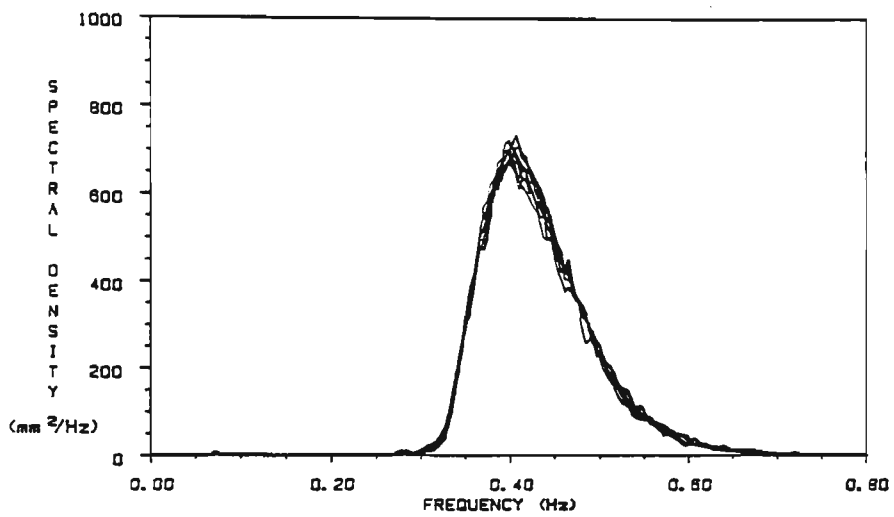
The results of statistical analyses on the stored experimental data are tabulated below.

Experiment number	:	1	2	3	4	5
Energy content, $M_0$ ( $\text{mm}^2$ )	:	90.3	475.2	600.3	524.4	420.3
RMS water surface elevation (mm)						
from time record	:	9.5	21.8	24.6	23.0	20.5
from spectral estimates	:	9.5	21.8	24.6	22.9	20.5
Spectral width parameter, $\epsilon_t$						
from time record	:	0.317	0.404	0.473	0.461	0.700
Spectral width parameter, $\epsilon_s$						
from spectral estimates	:	0.29	0.387	0.443	0.467	0.629

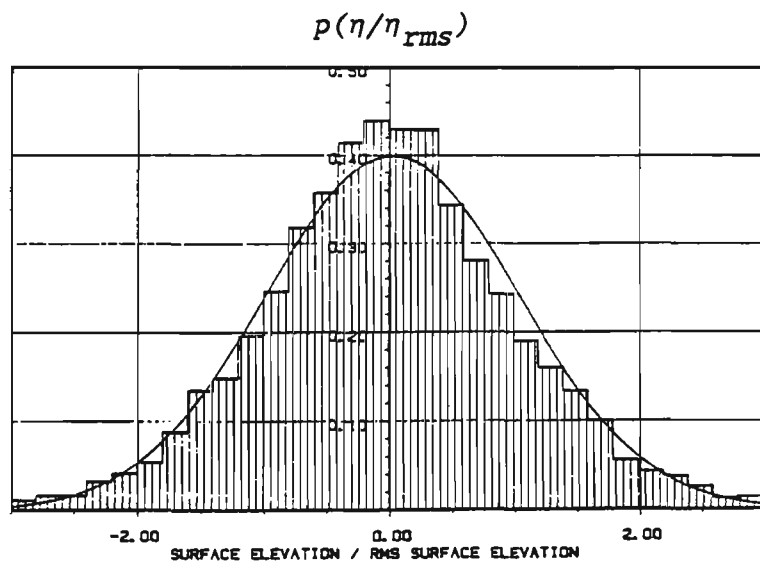
Table 5.2. Statistical results - single peak spectrum.



(a) Average of measured spectral estimates.

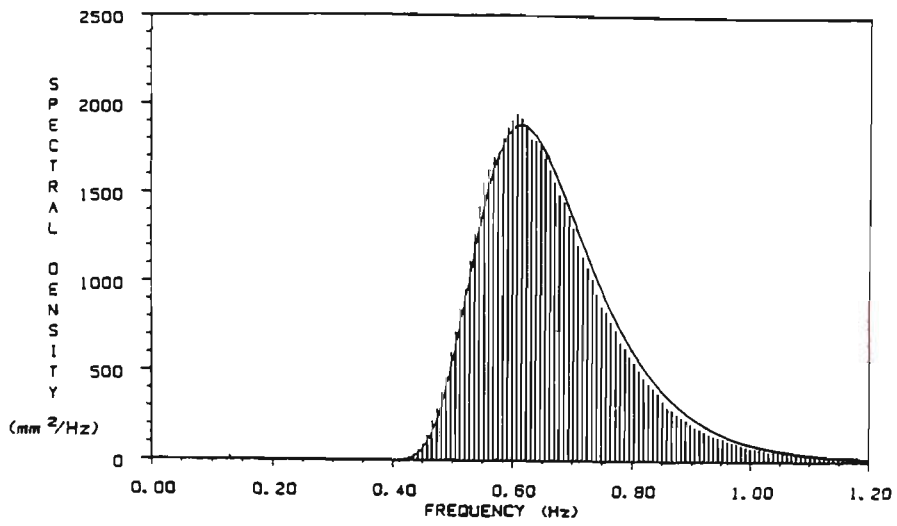


(b) Individually measured spectral estimates.

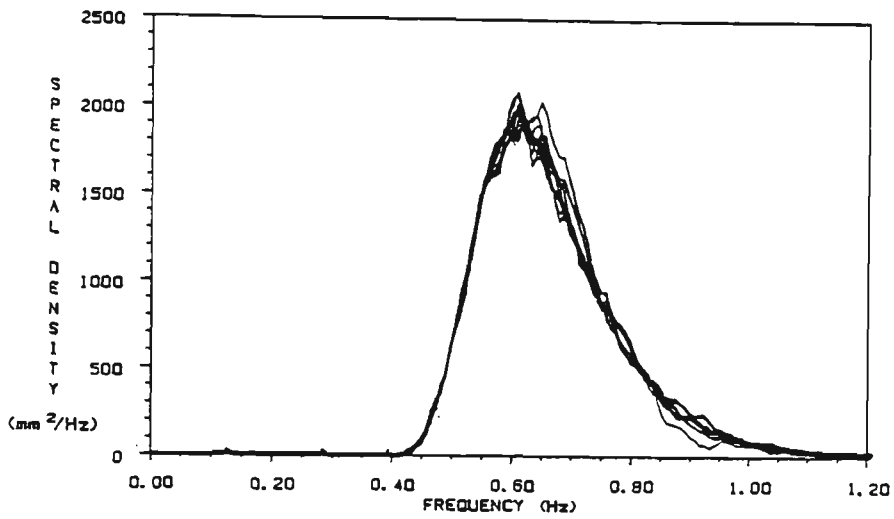


(c) Surface elevation distribution.

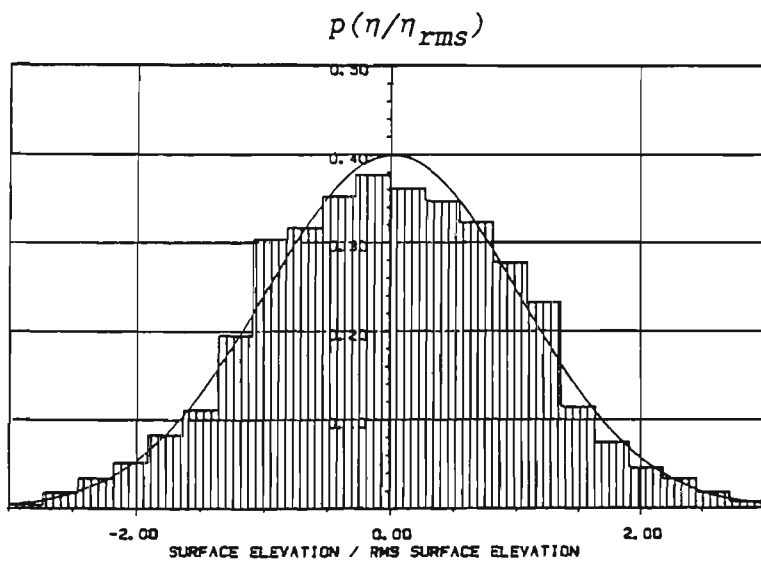
Figure 5.16. Single peak spectrum - Experiment 1.



(a) Average of measured spectral estimates.

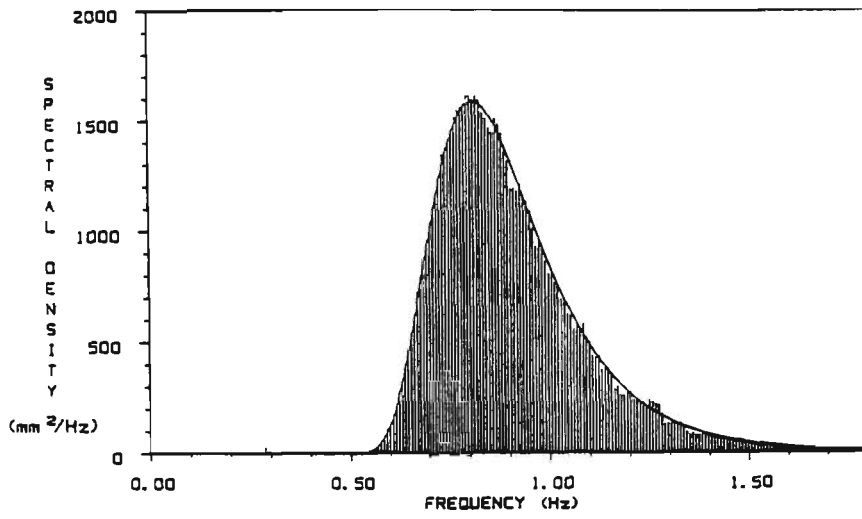


(b) Individually measured spectral estimates.

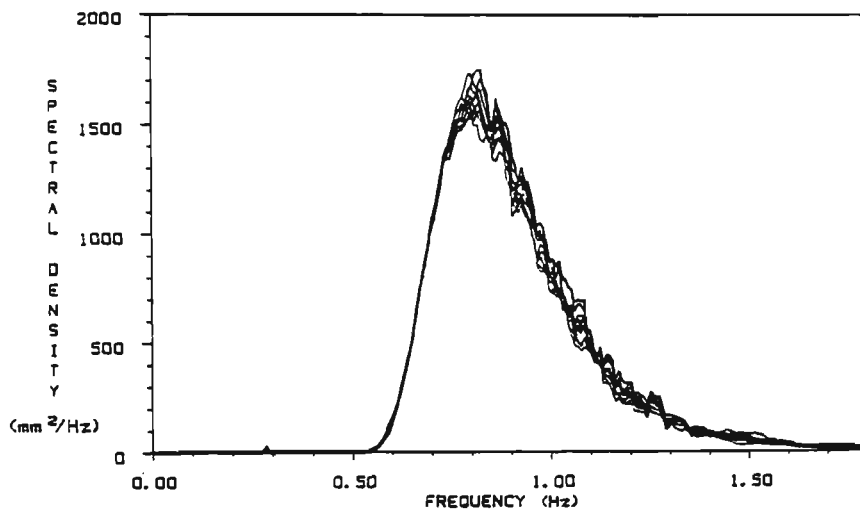


(c) Surface elevation distribution.

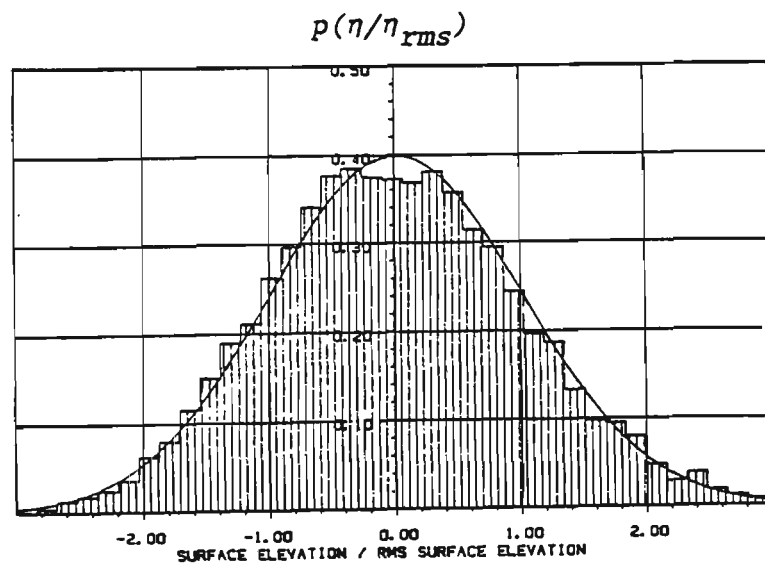
Figure 5.17. Single peak spectrum - Experiment 2.



(a) Average of measured spectral estimates.

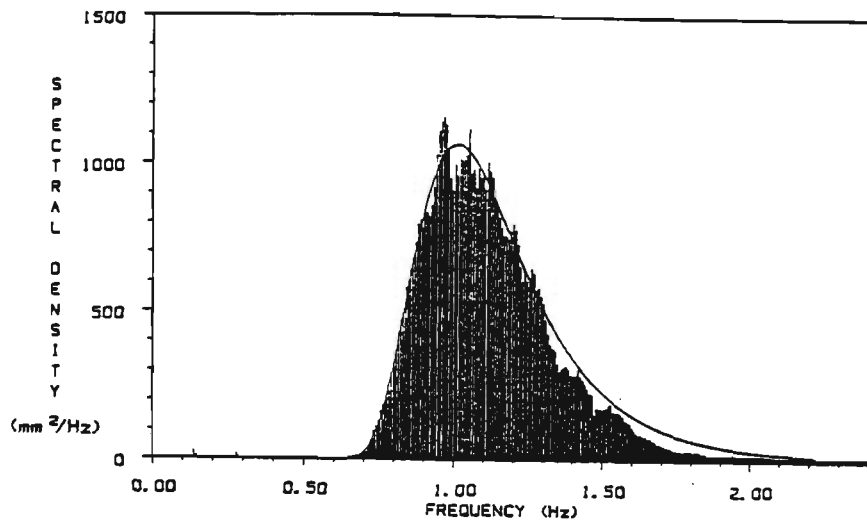


(b) Individually measured spectral estimates.

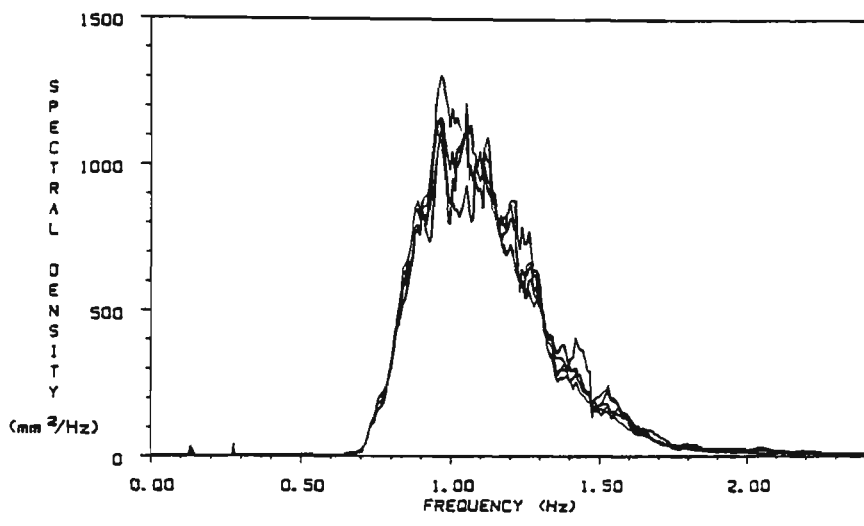


(c) Surface elevation distribution.

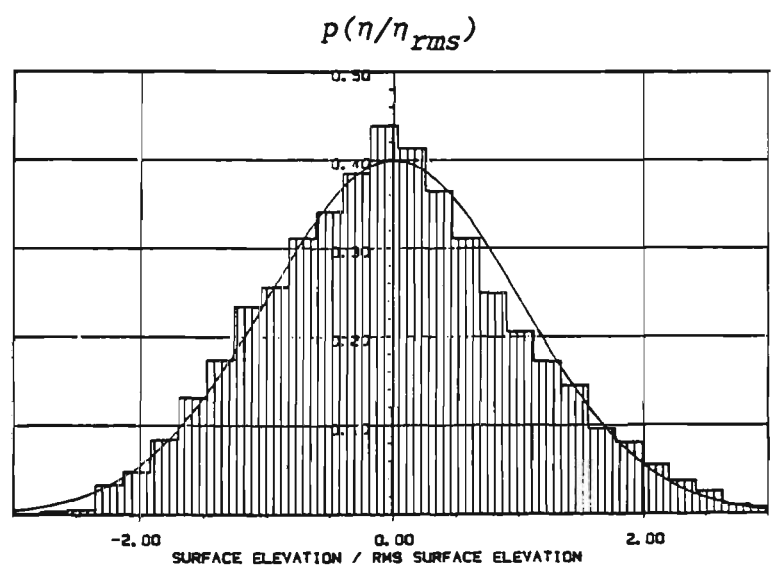
Figure 5.18. Single peak spectrum - Experiment 3.



(a) Average of measured spectral estimates.

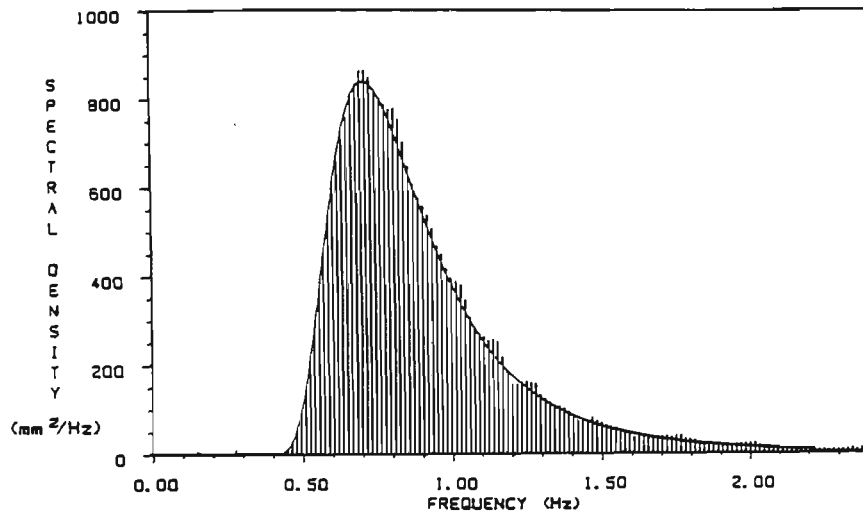


(b) Individually measured spectral estimates.

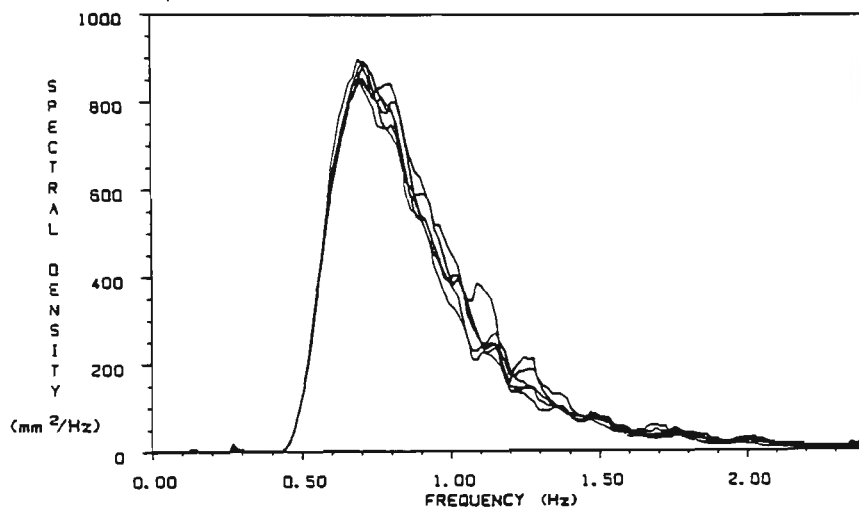


(c) Surface elevation distribution.

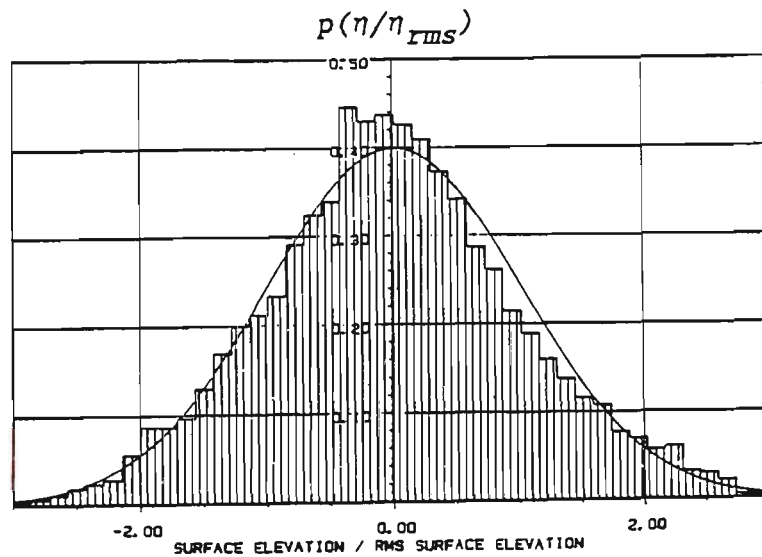
Figure 5.19. Single peak spectrum - Experiment 4.



(a) Average of measured spectral estimates.



(b) Individually measured spectral estimates.



(c) Surface elevation distribution.

Figure 5.20. Single peak spectrum - Experiment 5.

In can be seen from graphs (a) of figures 5.16 - 5.20 that good agreement was achieved between target and measured spectral estimate for spectral models with relatively narrow spectral bandwidths, namely experiments 1, 2, and 3. The small discrepancies between target and measured spectral estimates for spectral models with broader spectral bandwidths (experiments 4 and 5) may be attributed to unrecoverable loss of energy between the wave maker and the wave probe due to the breaking of the steeper waves in the flume.

Graphs (b) of figures 5.16 - 5.20 show that the variation of the individually measured spectral estimates with respect to time, as new compensated command signals are generated, was small for spectral models with a small spectral width parameter - namely experiments 1, 2 and 3. The steady simulation of broader spectral models - experiments 4 and 5 - proved to be more difficult to achieve. This may be explained by the increasingly nonlinear nature of generated waves with greater significant wave field slopes which may not be readily controlled by simple linear spectral feedback compensation techniques.

The water surface elevation distributions were found to agree well with the Gaussian distribution as shown in graphs (c) of figures 5.16 - 5.20. A slight skewness of the distribution histograms from experiments 4 and 5 may be detected and may be attributed to the nonlinearity of the wave field as often observed in nature.

The statistical analysis results displayed in table 5.2 are in generally good accord with the theoretical values of table 5.1. The spectral width parameters  $\epsilon_s$  and  $\epsilon_t$  from experiment 4 ( $\epsilon_s = 0.467$ ) and ( $\epsilon_t = 0.461$ ) can be seen to differ considerably with the theoretical value ( $\epsilon_s = 0.533$ ). This may be explained by referring to graph (a) of figure 5.19 where the linear average of the measured spectral estimates is noticeably narrower than the target spectrum; hence the discrepancy in measured and theoretical spectral width parameters.

## 5.7. Generation of Double Peak Spectral Models.

This series of experiments were conducted with the aim of investigating the ability of the facility to generate various double peak spectral wave models. Three double peak Wallops spectral models representing swell together with various sea conditions were used as target spectra and are displayed in figure 5.21. Generation was undertaken with the WGENSP program library described in section 6.4.4. Statistical analysis of the measured water surface elevation records together with their corresponding spectral estimates were performed with the WSTAT program library described in section 6.4.5. All experiments were conducted with a still water level of 900 mm and the control system was set to closed-loop spectral feedback mode.

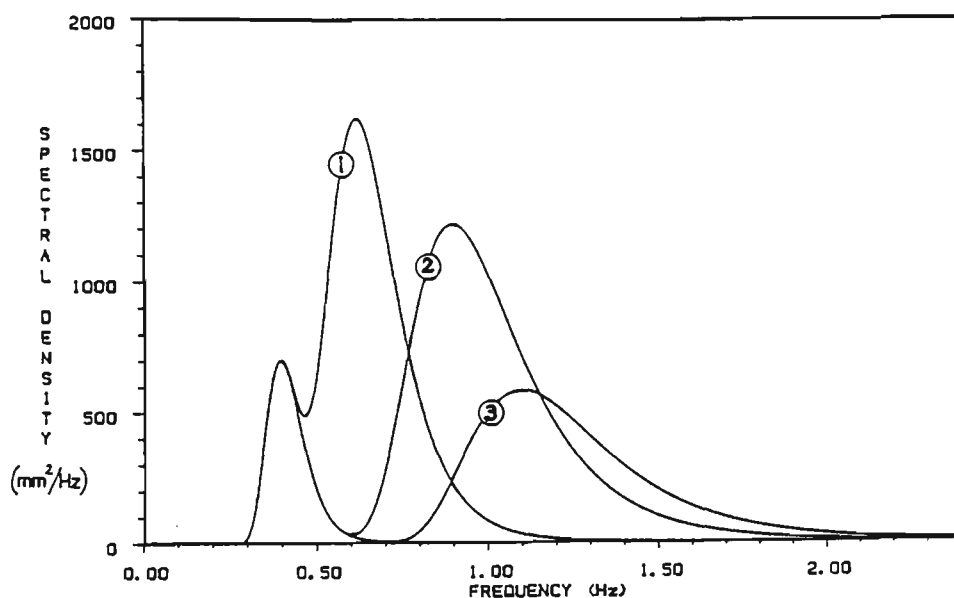


Figure 5.21. Double peak target spectra.

As for the generation of single peak spectral models, the distribution of a typical command signal was computed and was found to be in good agreement with the Gaussian distribution.

After the preliminary parameters defining the target spectrum and the required operating conditions of the machine were specified, the wave generator was switched on and the command signal transmitted to the system. The process was then allowed to stabilize while operating in the closed-loop spectral compensation mode. While random waves were continuously generated for an predetermined period of time, both the water surface elevation data and its corresponding spectral estimate were stored

on the system hard disk. Statistical analysis of the stored experimental water surface elevation data was carried later. The specifications of each target spectrum are outlined in table 5.3 together with the experimental conditions.

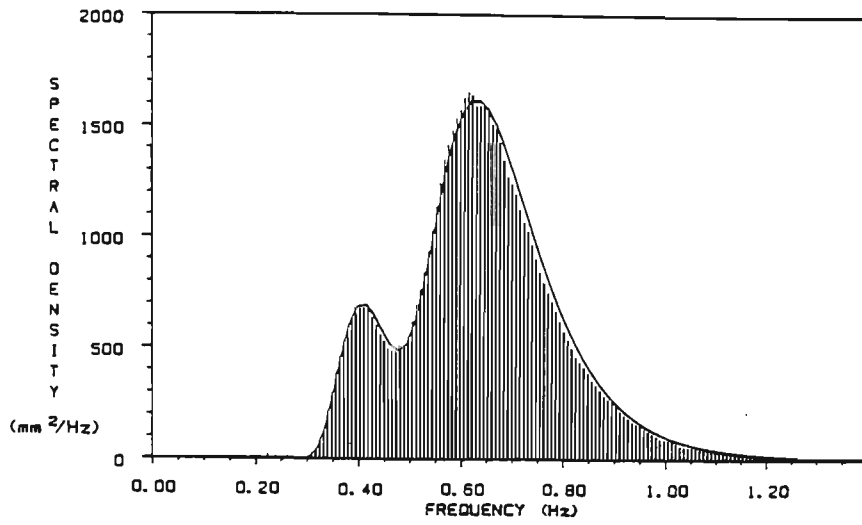
Experiment number	:	1	2	3
Target spectral model (double peak)	:	Wallops	Wallops	Wallops
Spectral peak frequency (Hz) (swell)	:	0.4	0.4	0.4
Spectral peak frequency (Hz) (sea)	:	0.62	0.9	1.1
Significant wave field slope, $\xi$ (swell)	:	0.001	0.001	0.001
Significant wave field slope, $\xi$ (sea)	:	0.005	0.012	0.014
Nominal total energy content ( $\text{mm}^2$ )	:	507.6	630.2	421.5
Loop duration (seconds)	:	128	128	64
Frequency resolution (Hz)	:	5/128	11/128	9/64
Number of spectral estimates	:	10	10	12

Table 5.3. Experimental conditions - double peak spectrum.

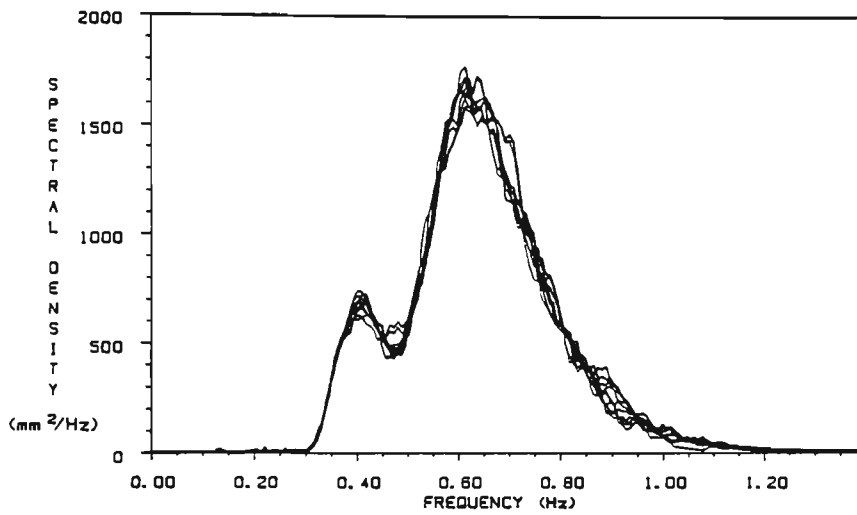
The results of experiments 1, 2 and 3 are displayed in figures 5.22 - 5.24 respectively where graphs (a) show the linear average of the measured spectral estimates together with the target spectrum model while graphs (b) show the individually measured spectral estimates of the simulated wave field at each loop of operation. Finally, in graphs (c) the normalised water surface elevation distribution of the measured wave field is presented together with the theoretical Gaussian distribution. The results of statistical analyses on the experimental data are displayed in table 5.4 below.

Experiment number	:	1	1	3
Energy content, $M_0$ ( $\text{mm}^2$ )	:	506.3	625.0	420.3
RMS water surface elevation, (mm)	:			
from time record	:	22.5	25.2	20.8
from spectral estimates	:	22.5	25.0	20.5
Spectral width parameter, $\epsilon_t$	:			
from time record	:	0.472	0.571	0.766
Spectral width parameter, $\epsilon_s$	:			
from spectral estimates	:	0.446	0.496	0.561

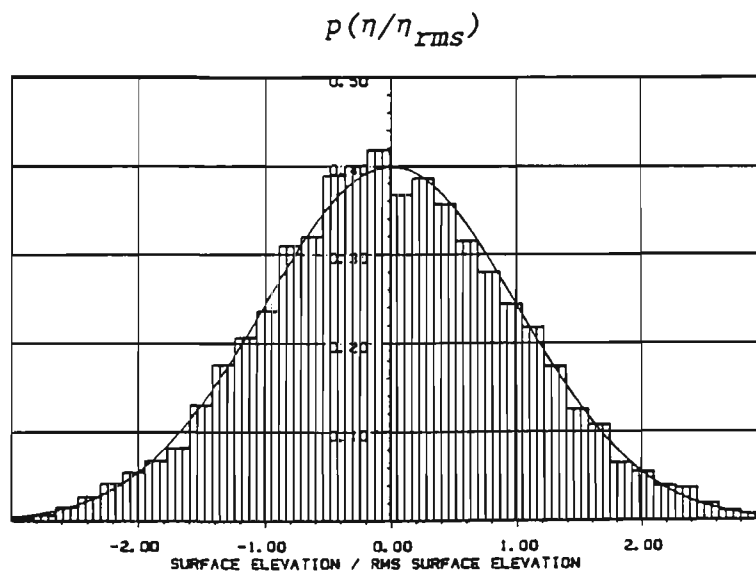
Table 5.4. Statistical results - double peak spectrum.



(a) Average of measured spectral estimates.

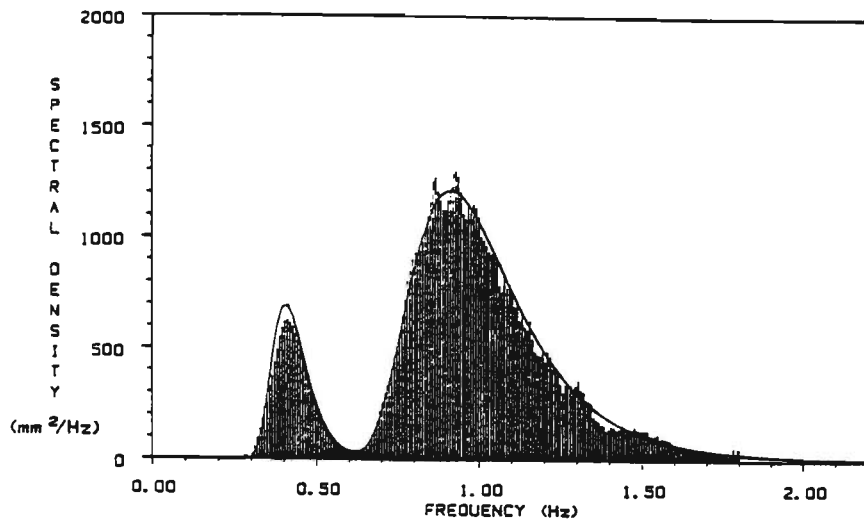


(b) Individually measured spectral estimates.

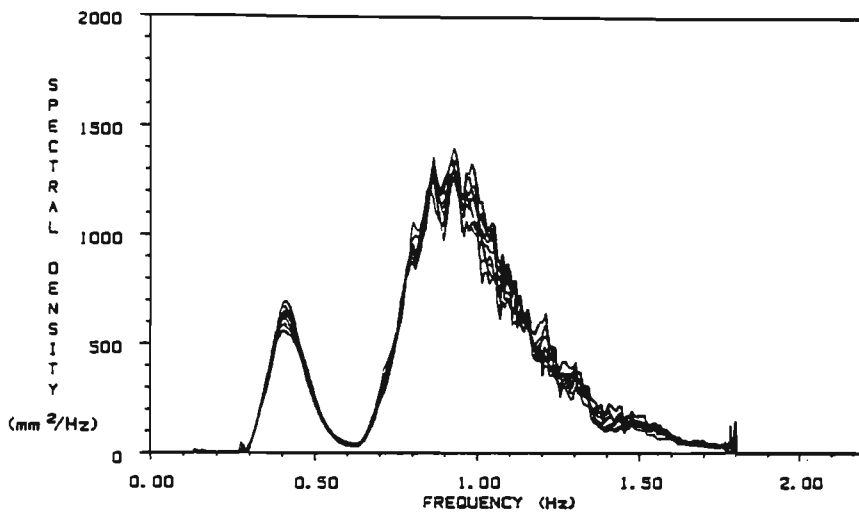


(c) Surface elevation distribution.

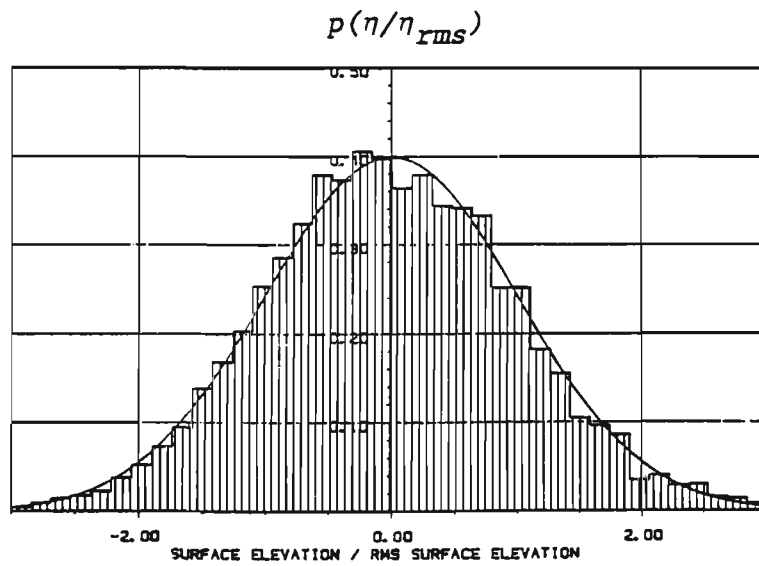
Figure 5.22. Double peak spectrum - Experiment 1.



(a) Average of measured spectral estimates.

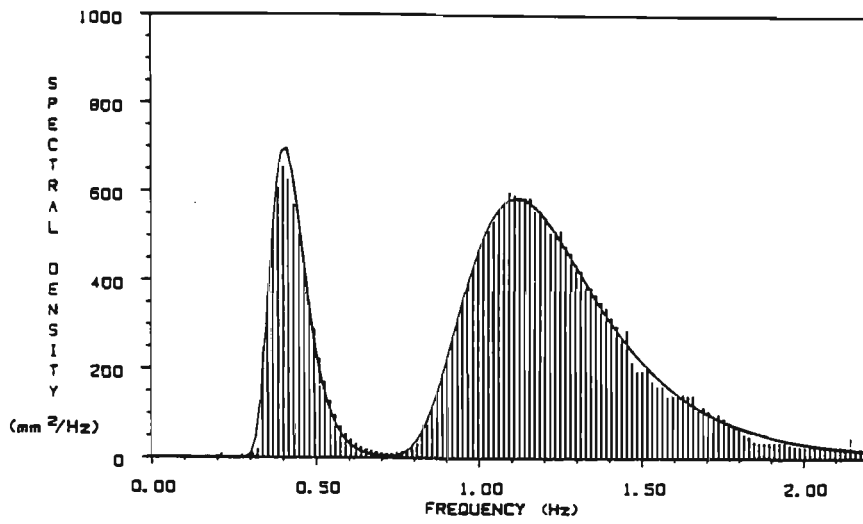


(b) Individually measured spectral estimates.

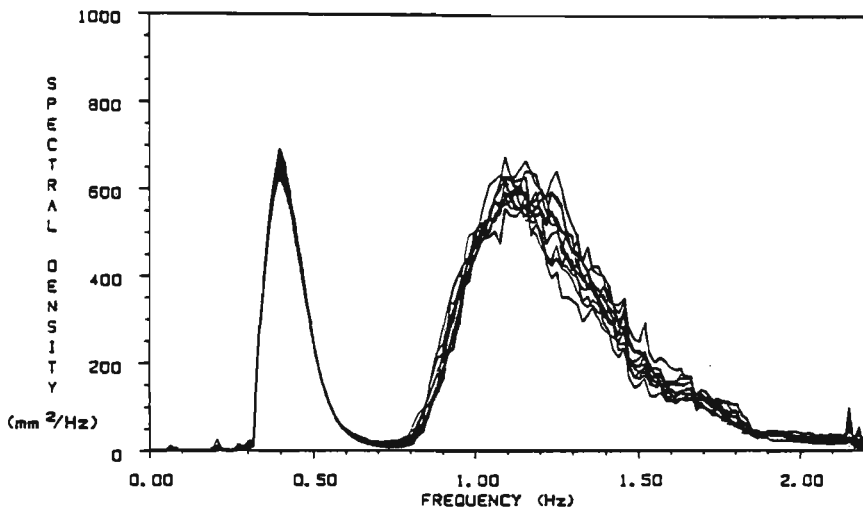


(c) Surface elevation distribution.

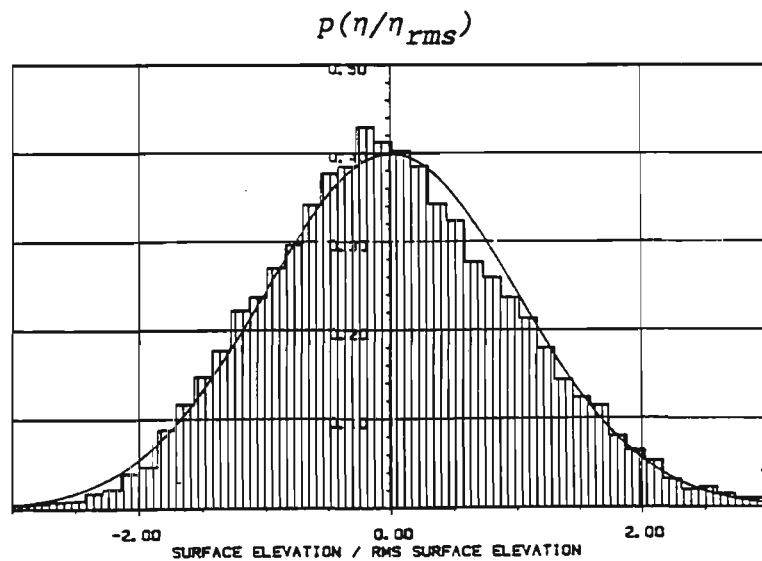
Figure 5.23. Double peak spectrum - Experiment 2.



(a) Average of measured spectral estimates.



(b) Individually measured spectral estimates.



(c) Surface elevation distribution.

Figure 5.24. Double peak spectrum - Experiment 3.

It can be seen from graphs (a) of figures 5.22 - 5.24 that the linear average of the measured spectral estimates is in reasonably good agreement with the target spectra. It can also be seen from graphs (b) of figures 5.22 - 5.24 that the variation of the measured spectral estimates with respect to time (or loop of operation) seems to increase with the nonlinearity of the wave field.

The distribution of the water surface elevation, displayed in graphs (c) of figures 5.22 - 5.24, appear to be in reasonable accordance with the theoretical Gaussian distribution. Furthermore, it can be seen that, although not quantified, the skewness of the water surface elevation distribution histograms increases slightly with the nonlinearity of the wave field.

The results from further statistical analysis of the experimental data, displayed in table 5.4, generally show good agreement with the theoretical values of table 5.3. It can be seen from table 5.3 that the spectral width parameter  $\epsilon_s$ , computed from the spectral estimates of experiments 2 and 3, are inferior to those computed from the time records of the same experiments. These discrepancies are, in this case, attributed to the fact that the cutoff frequencies of the measured spectral estimates were set at only twice the spectral peak frequency of the 'sea' spectrum (i.e. cutoff frequencies of 1.8 Hz and 2.2 Hz for experiments 2 and 3 respectively). It is made evident from graphs (a) and (b) of figures 5.23 and 5.24 that these cutoff frequencies were excessively low leading to difficulties in the accurate computation of the spectral moments.

## 6. CONCLUSIONS

A laboratory facility for generating water waves comprising a flume, electro-hydraulic wave generator, wave absorbers and wave probe was designed and commissioned. Tasks associated with generating waves such as: calibration of wave probes, assessment of wave reflection characteristics, evaluation of system frequency response, data acquisition and statistical analyses of wave records were successfully accomplished using specially developed software.

The electro-hydraulic wave generator, under the command of a micro-computer, was rigorously tested over a range of operating conditions and functioned very well. Algorithms devised to create random waves from ocean wave spectral models were written using the Inverse Fast Fourier Transform and closed-loop spectral feedback compensation techniques. Experiments carried out confirmed that the system performed better under closed-loop spectral feedback control than under open-loop control. The generation of long random wave trains was successfully achieved by continuously reproducing shorter segments each complying with the original target spectral density and distribution functions.

The amplitude reflection coefficients of the wave absorbers were measured for waves ranging from 0.5 to 1.1 Hertz and were found to vary between 9.5 % and 2.5 %.

A range of single peak spectral wave models were simulated using spectral feedback compensation. Four single peak Wallops spectra, with various spectral peak frequencies and significant wave field slopes, along with one P-M spectrum were generated. Three double peak Wallops spectra, representing swell together with a variety of seas, were also simulated with generally good agreement between target spectra and measured spectral estimates. Analysis of recorded wave data showed that the probability distribution of the water surface elevation compared favourably with the Gaussian distribution.

## BIBLIOGRAPHY

- BENDAT, J.S. & PIERSOL, A.G. 1971. *Random Data Analysis and Measurement Procedures*. Wiley - Interscience, John Wiley & Sons, New York.
- BENDAT, J.S. & PIERSOL, A.G. 1980. *Engineering Applications of Correlation and Spectral Analysis*. Wiley - Interscience, John Wiley & Sons, New York.
- BENDAT, J.S. & PIERSOL, A.G. 1986. *Random Data Analysis and Measurement Procedures*. (2nd Ed.). Wiley - Interscience, John Wiley & Sons, New York.
- BIESEL, F. & SUQUET, F. 1951 (b). *Les appareils generateurs de houle en laboratoire*. *La Houille Blanche*, 6 (2 & 4), pp 147 - 165, pp 475 - 483.
- BLACKMAN, R.B. & TUKEY, J.W. 1959. *The Measurement of Power Spectra from the Point of View of Communications Engineering*. Dover Publications, New York.
- BLOOMFIELD, P. 1976. *Fourier Analysis of Time Series: an Introduction*. John Wiley & Sons, New York.
- BORGMAN, L.E. 1969. *Ocean wave simulation for engineering design*. *Journal of the Waterways and Harbours Division*, proc. ASCE, 95 (ww 4), pp 557 - 583
- BRIGHAM, E.O. 1974. *The Fast Fourier Transform*. Prentice - Hall, New Jersey.
- CACKO, J., BILY, M. & BUKOVECZKY, J. 1988. *Random Processes: Measurement, Analysis and Simulation*. Elsevier Science, New York.
- CARTWRIGHT, D.E & LONGUET-HIGGINS, M.S. 1956. *The Statistical Distribution of the Maxima of a Random Function*. *Proc. Royal Soc. London*, Ser. A, 237, pp 212 -232.

- CHAKRABARTI, S.K. 1987. *Hydrodynamics of Offshore Structures*. Computational Mechanics Publications, Springer - Verlag, Berlin.
- DANISH HYDRAULIC INSTITUTE. 1984. *DHI's Offshore Test Bassin - Final Report*. Danish Hydraulic Institute.
- DEAN, R.G. 1965. *Stream Function Representation of Nonlinear Ocean Waves*. *Journal of Geophysical Research*, 70 (18).
- FORRISTAL, G.Z. 1978. *On the Statistical Distribution of Wave Heights in a Storm*. *Journal of Geophysical Research*, 83 (C5), pp 2353 - 2358.
- FRYER, D.K., GILBERT, G. & WILKIE, M.J. 1973. *A Wave Spectrum Synthesizer*. *Journal of Hydraulic Research*, 11 (3), pp 193 - 204.
- FUNKE, E.R. 1974. *Random Wave Signal Generation by Minicomputer*. *Proceedings of the Coastal engineering Conference, Copenhagen*, pp 353 - 369.
- GILBERT, G., THOMPSON, D.M. & BREWER, A.J. 1971. *Design Curves for Regular and Random Wave Generators*. *Journal of Hydraulic Research*, 9, pp 163 - 196.
- GODA, Y. 1970. *Numerical Experiments on Wave Statistics with Spectral Simulation*. *Rept. Port and Harbour Res. Inst.*, 9 (3), pp 3 - 57.
- GODA, Y. 1974. *Estimation of Wave Statistics from Spectral Information*. *Proceedings of the Int. Symposium on Ocean Waves Measurement and Analysis*, ASCE, New Orleans, pp 320 - 337.
- GODA, Y. 1977. *Statistical Theory of Random Waves*. *Serial Seminar*.
- GODA, Y. 1985. *Random Seas and Design of Maritime Structures*. *University of Tokyo Press*.
- HANSEN, J.B., SCHIOLTEN, P. AND SVENDSEN, I.A. 1975. *Laboratory Generation of waves of Constant Form*. *Institute of Hydrodynamics and Hydraulic Engineering, Technical University of Denmark, Series paper 9*.

- HASSELMANN, K. 1973. *Measurements of Wind Wave Growth and Swell Decay during the Joint North Sea Wave Project (JONSWAP)*. *Deutsch Hydrographische Zeitschrift, Reihe A* 8 (12).
- HASSELMANN, K., ROSS, D.B., MULLER, P. & SELL, W. 1976. *A Parametric Wave Prediction Model*. *Journal of Physical Oceanography*, 5, pp 200 - 228.
- HAVELOCK, T.H. 1929. *Forced Surface Waves on Water*. *Philosophical Magazine, Ser. 7*, 8 (51), pp 569 - 576.
- HINWOOD, J.B., BLACKMAN, R.D. & LLEONART, G.T. 1982. *Some Properties of Swell in the Southern Ocean*. *Proceedings of the 18th International Conference on Coastal Engineering, Cape Town, Nov. 1982*, pp 261 - 269.
- HUANG, N.E. & LONG, S.R. 1980. *An Experimental Study of the Surface Elevation probability Distribution and Statistics of Wind-generated waves*. *Journal of Fluid Mechanics*, 101 (1), pp 179 - 200.
- HUANG, N.E., LONG, S.R., TUNG, C., YUEN, Y. & BLIVEN, L.F. 1981. *A Unified Two-parameter Wave Spectral Model for a General Sea State*. *Journal of Fluid Mechanics*, 112, pp 203 - 224.
- HUDSPETH, R.T. & BORGMAN, L.E. 1979. *Efficient FFT Simulation of Digital Time Sequences*. *Proc. ASCE*, 105 (EM2), pp 223 - 235.
- HUYN, J.M. 1976. *Simplified Analysis of a Plunger Type Wavemaker Performance*. *Journal of Hydronautics*, 10 (3), pp 89 - 94.
- IPPEN, A.T. (ed). 1966. *Estuary and Coastline Hydrodynamics*. McGraw-Hill. New York.
- KEATING, T. & WEBBER, N.B. 1977. *The Generation of Periodic waves in a Laboratory Channel : a Comparison between Theory and Experiment*. *Proc. Institution of Civil Engineers, Part 2*, 63, pp 819 -832.
- KINSMAN, B. 1965. *Wind Waves, their Generation and Propagation on the Ocean Surface*. Prentice-Hall, New Jersey.

- LE MEHAUTE, B. 1976. *An Introduction to Hydrodynamics and Water Waves*. Springer-Verlag. New York.
- LIU, P.C. 1971. *Normalized and Equilibrium Spectra of Wind Waves in Lake Michigan*. *Journal of Physical Oceanography*, 1 (4), pp 249 - 257.
- LONGUET-HIGGINS, M.S. 1952. *On the Statistical Distribution of the Heights of Sea Waves*. *Journal of Marine Research*, 11, pp 245 - 266.
- LONGUET-HIGGINS, M.S. 1957. *The Statistical Analysis of a Random, Moving Surface*. *Philosophical Transactions, Royal Society, A 249*, pp 321 - 387.
- LONGUET-HIGGINS, M.S. 1963. *The Effects of Non-linearities on Statistical Distributions in the Theory of Sea Waves*. *Journal of Fluid Mechanics*, 17, pp 459 - 480.
- LONGUET-HIGGINS, M.S. 1980. *On the Distribution of the Heights of Sea Waves: Some Effects of Nonlinearity and Finite Band Width*. *Journal of Geophysical Research*, 85 (C3), pp 1519 - 1523.
- MADSEN, O.S. 1971. *On the Generation of Long Waves*. *Journal of Geophysical Research*, 76 (36), pp 8672 - 8683.
- MCCORMICK, M.E. 1973. *Ocean Engineering Mechanics*. John Wiley & Sons. New York.
- MITCHELL, G.M., SOBEY, R.J., BARBAGALLO, A.M.J. & COLMAN, E.J. 1979. *A Programmable Water Wave generator*. *Research Bulletin No. CS18, Department of Civil & Systems Engineering, James Cook University of North Queensland*.
- MITSUYASU, H. 1972. *The One-dimensional Wave Spectra at Limited fetch*. *Proceedings of the Thirteen Coastal Engineering Conference, Vancouver, B.C., ASCE*, 1, pp 289 - 306.
- MULTER, R.H. & GALVIN, C.J.Jnr. 1967. *Secondary Waves: Periodic Waves of Nonpermanent form - (Abstract)*. *Transactions of the American Geophysical Union*, 48, pp 139 - 140.

- NEWLANDS, D.E. 1975. *An Introduction to Random Vibrations and Spectral Analysis*. Longman, London.
- OCHI, M.K. 1972. *On Prediction of Extreme Values*. *Journal of Ship Research*, pp 29 -37.
- OCHI, M.K. & HUBBLE, E.N. 1976. *Six-parameter Wave Spectra*. *Journal of Waterways and Harbours Division, ASCE*, pp 557 - 583.
- PHILLIPS, O.M. 1958. *The Equilibrium Range in the Spectrum of Wind Generated Waves*. *Journal of Fluid Mechanics*, 4, pp 426 - 434.
- PHILLIPS, O.M. 1961. *On the Dynamics of Unsteady Gravity Waves of Finite Amplitude. Part 2*. *Journal of Fluid Mechanics*, 11, pp 143 - 155.
- PIERSON, W.J. & MOSKOWITZ, L.A. 1964. *A Proposed Spectral Form for Fully developed Wind Seas Based on the Similarity Law of S.A. Kitaigorodskii*. *Journal of Geophysical Research*, 69 (24), pp 5181 - 5203.
- RANDALL, R.B. 1987. *Frequency Analysis (3rd Ed.)*. Bruel & Kjaer.
- RICE, S.O. 1944 - 45. *The Mathematical Analysis of Random Noise*. *Bell Syst. Tech. Journal*, 23, pp 282 - 232, 24, pp 46 - 156. Reprinted in *Selected Papers on Noise and Stochastic Process*, WAX, N. ed., Dover Publications, New York. 1954. pp 133 -294.
- SAND, S.E. 1979. *Three-dimensional Deterministic Structure of Ocean Waves*. *Institute of Hydrodynamics & Hydraulic Engineering, Technical university of Denmark*, Ser. paper 24.
- SAND, S.E., BJARNE, D, KARSTEN, H.H. & NIELS, M. 1982. *Optimization of Absorbers for DHI's Offshore Test Bassin by Means of a 3-gauge Reflection Procedure*. *Danish Hydraulic Institute*.
- SHORE PROTECTION MANUAL. 1984. *U.S. Army Coastal Engineering Research Centre, U.S. Government Printing Office, 4th Ed.*

- SILVESTER, R. 1974. *Coastal Engineering, I. Generation, Propagation and Influence of Waves*. Elsevier Scientific Publishing Co. New York.
- STOKES, G.G. 1847. *On the Theory of Oscillatory Waves*. *Trans. Cambridge Phil. Soc.*, 8, pp 441 - 455. (Also in *Mathematical and Physical Papers*, 1, pp 197 - 229. Cambridge University Press, London.)
- STOKES, G.G. 1880. *Supplement to the 1847 paper: On the Theory of Oscillatory Waves*. *Mathematical and Physical Papers*, 1, pp 314 - 326. Cambridge University Press, London.
- STOKER, J.J. 1957. *Water Waves*. Interscience Publishers Inc. New York.
- SVENDSEN, I.A & JONSSON, I.G. 1976. *Hydrodynamics of Coastal Regions*. Technical University of Denmark.
- SVERDRUP, H.U. & MUNK, W.H. 1947. *Wind, Sea and Swell: Theory of Relations for Forecasting*. U.S. Navy Hydrographic Office, Publication No. 601.
- TUCKER, M.J. 1963. *Analysis of Records of Sea Waves*. *Proceedings of the Institute of Civil Engineers*, 26, pp 305 - 316.
- URSELL, F., DEAN, R.G. & YU, Y.S. 1960. *Forced Small-amplitude Water Waves: a Comparison of Theory and Experiment*. *Journal of Fluid Mechanics*, 7, pp 33 - 52.
- WANG, S. 1974. *Plunger-Type Wavemakers: Theory and Experiment*. *Journal of Hydraulic Research*, 12 (3), pp 357 - 388.
- WEBBER, N.B. & CHRISTIAN, C.D. 1974. *A Programmable Irregular Wave Generator*. *Proceedings of the Coastal Engineering Conference, Copenhagen*, pp 340 - 351.
- WILSON, J.F. (Ed). 1984. *Dynamics of Offshore Structures*. Wiley - Interscience, John Wiley & Sons, New York.

Further Theoretical Definitions for the Wallops Spectrum. - After Huang et. al. (1981).

The definition of the  $n^{th}$  moment,  $M_n$ , of a spectral density function is defined as

$$M_n = \int_0^{\infty} \omega^n S(\omega) d\omega \quad (A1)$$

For the Wallops spectrum

$$M_n = M_0 (m/4)^{n/4} \omega_0^n \frac{\Gamma[0.25(m-n-1)]}{\Gamma[0.25(m-1)]} \quad (A2)$$

where

$$M_0 = \frac{\beta g^2 4^{0.25(m-5)}}{m^{0.25(m-1)} \omega_0^4} \cdot \Gamma[(m-1)/4] \quad (A3)$$

Hence the theoretical nominal energy content,  $M_0$ , may be obtained from equation (A3) and the theoretical spectral width parameter,  $\epsilon_s$ , from

$$\epsilon_s = \sqrt{\frac{M_0 M_4 - M_2^2}{M_0 M_4}} \quad (A4)$$

The spectral bandwidth,  $\nu$ , for the wallops spectrum, as defined by Longuet-Higgins (1957), may be theoretically determined from

$$\nu = \left[ 1 - \frac{\Gamma^2[0.25(m-2)]}{\Gamma[0.25(m-3)] \Gamma[0.25(m-1)]} \right]^{0.5} \quad (A5)$$

Since  $m$  is a function of the significant slope of the wave field,  $\xi$ , the spectral bandwidth,  $\nu$ , is also a function of  $\xi$  alone. The Wallops spectrum is therefore a spectral model of variable bandwidth which depends solely on the nonlinearity of the wave field.

Formulation of the Plunger Generating Surface.

The shape of the plunger was formulated so that the differences in horizontal displacement at each horizontal plane would be minimized as illustrated in figure 6.3. The shape of the generating surface was developed by considering the rotation of the wave maker by a nominal angle  $\theta$  about the pivot point 'o' as shown in figure 1B.

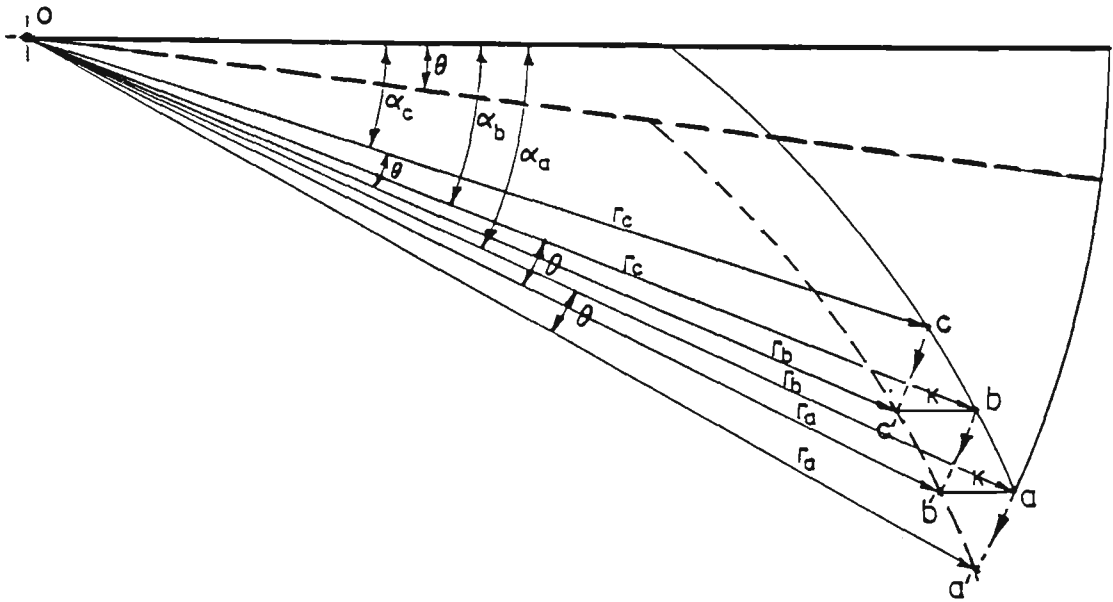


Figure 1B. Development of the plunger generating surface.

The polar coordinates of points  $a, b, c \dots$  are defined by  $\alpha_a, \alpha_b, \alpha_c \dots$  and  $r_a, r_b, r_c \dots$  respectively. It may be seen from figure 1B that for a specific angle of rotation  $\theta$ , a unique curve may be generated for which the horizontal displacement at every plane shall be the same (i.e. equal to a constant  $k$ ). This unique curve may be generated as follows:

$$r_a \cos(\alpha_a) - r_b \cos(\alpha_b + \theta) = k \tag{B1}$$

$$r_b \sin(\alpha_a) = r_b \sin(\alpha_b + \theta) \tag{B2}$$

Re-arranging equation (B2)

$$r_b = r_a \sin(\alpha_a) / \sin(\alpha_b + \theta) \quad (B3)$$

Substituting for  $r_b$  in equation (B1) and making  $\alpha_b$  the subject of the equation

$$\alpha_b = \tan^{-1} [r_a \sin(\alpha_a) / (r_a \cos(\alpha_a) - k)] - \theta \quad (B4)$$

Similarly

$$r_c = r_b \sin(\alpha_b) / \sin(\alpha_c + \theta) \quad (B5)$$

$$\alpha_c = \tan^{-1} [r_b \sin(\alpha_b) / (r_b \cos(\alpha_b) - k)] - \theta \quad (B6)$$

and likewise for  $\alpha_d, \alpha_e \dots$  etc.

Therefore, by initially defining the coordinates of point a (i.e.  $\alpha_a$  and  $r_a$ ) and a constant  $k$ , a unique curve may be generated for a specific angle of rotation  $\theta$ .

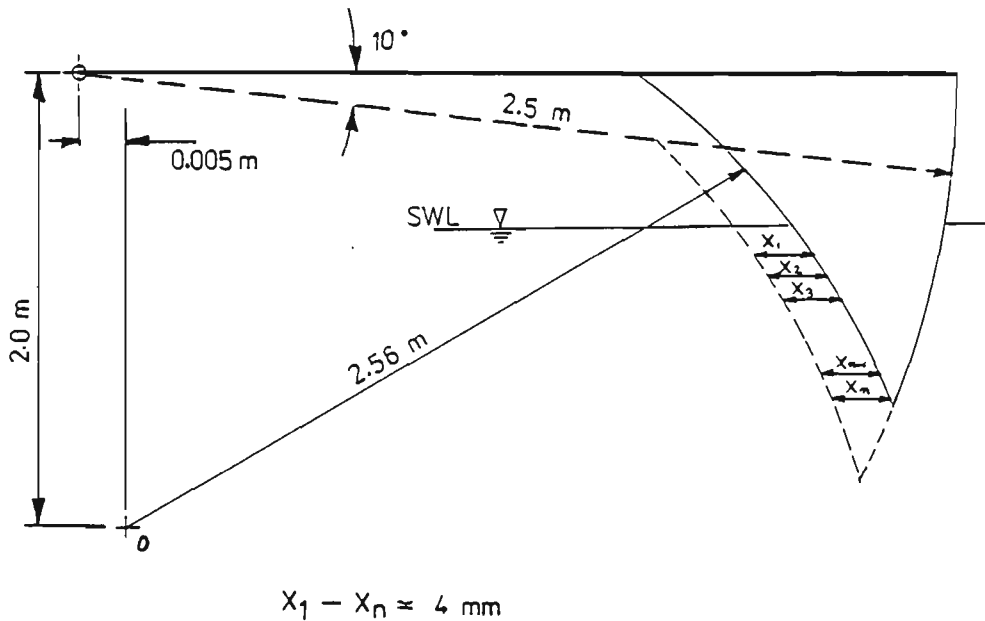


Figure 2B. Expected maximum horizontal displacement error.

A curve was generated using equations (B3), (B5).... and (B4), (B6)... by means of a BASIC computer program. By fitting a circular arc to the resulting data points values of the radius and centre point coordinates were obtained.

Further analysis of the curve showed that when the wave maker was rotated by  $10^{\circ}$  (expected maximum rotation), the maximum error in horizontal displacement, as defined in figure 2B, is approximately 4 mm.